2D CONTROLLED SOURCE SEISMIC MAPPING OF THE LOW VELOCITY LAYER OF BLOCK 14T IN MAGADI, KENYA

ELLY BOGI MULUMBU

MASTER OF SCIENCE
(Applied Geophysics)

JOMO KENYATTA UNIVERSITY OF
AGRICULTURE AND TECHNOLOGY

2017

2D Controlled Source Seismic Mapping of the Low Velocity Layer of Block 14T in Magadi, Kenya

Elly Bogi Mulumbu

A Thesis Submitted in Partial Fulfillment for the Degree of Master of Science in Applied Geophysics in the Jomo Kenyatta University of Agriculture and Technology

2017

DECLARATION

This thesis is my original work and has not been presented for a degree in any other University.

Signature……………………………………..Date………………………..

Elly Bogi Mulumbu

This thesis has been submitted for examination with our approval as University Supervisors

Signature…………………………..Date………………………
Dr. Maurice Odondi K'orowe, PhD,
JKUAT, Kenya

Signature……………………….Date………………………
Dr. John Gitonga Githiri, PhD,
JKUAT, Kenya.

DEDICATION

This thesis is dedicated to my dear parents; Wicklif Mulumbu and Evelyne Anna. My late grandfather Jackton Oduku and Jackton Ondiek who in their great wisdom and encouragement, saw it fit and sent me to school when I had lost hope of attending school. Many thanks to you for noticing, believing and sending me back to school once more. I also dedicate it to my dear brothers, sisters and cousins, to my uncle Daniel Oduku who took care of me throughout my study period and ensured that I have all provisions I required to study successfully. You were all a great source of encouragement and inspiration to me.

ACKNOWLEDGEMENT

I sincerely wish to thank my academic supervisors: Dr. Maurice k'Orowe and Dr. John Githiri of Jomo Kenyatta University of Agriculture and Technology for their belief in me and continuous guidance throughout my research period. They were always available for consultation for my thesis, a source of encouragement and supported me at all times in my study period.

I also extend my appreciation to Mr. Muriuki for assisting me in digitizing maps for the study location. Special gratitude to National Oil Corporation of Kenya for allowing me use their seismic data for my thesis, Polaris Seismic International Ltd for internship training and provision of seismic software for processing the seismic research data. I am also grateful to Society of Exploration of Geophysicists for mentoring me during the period of study through sponsoring our various field camps that gave me great experience in my studies.

Further gratitude to Mr. Malcom Jeffreys and his wife Cynthia Berlier for funding my entire Masters study through Society of Exploration Geophysicists. I gratefully acknowledge their generosity in being a beneficiary of their funds for my study and for their keen interest in my studies. I am greatly indebted to them. Many thanks also to Physics department and JKUAT administration for allowing me do my study in their premises.

Finally and most important, I thank my heavenly Father, God for providing me with all the resources to enable me undertake this project and fruitful people that helped me accomplish my study. Glory and Honour to Him, now and always.

TABLE OF CONTENTS

LIST OF TABLES

LIST OF FIGURES

LIST OF APPENDICES

LIST OF ABBREVIATIONS AND ACRONYMS

EARS	East African Rift System
KRISP	Kenya Rift International Seismic Project
LVL	Low Velocity Layer
1D	1 Dimension
2D	2 Dimension
3D	3 Dimension
4D	4 Dimension
GPS	Global Positioning System
T_i	Intercept time
V_0	Average Velocity of the weathered zone/first layer
V_1	Average Velocity of the semi weathered zone/second layer
V_2	Average Velocity of the bedrock/third layer
T_u	Travel time for shot updip.
T_d	Travel time for shot downdip
Z_0 (H_0)	Depth of the weathered zone/ first layer
Z_1 (H_1)	Depth of semi-weathered zone/Second layer

ABSTRACT

A 2D controlled source shallow seismic refraction survey was carried out in Magadi basin in the southern part of Kenya to determine the characteristics of the low velocity layer. This involved mapping the thickness and corresponding velocities in the weathered zone which has considerable influence in processing and interpretation of deep seismic reflection data. The thicknesses and velocities are suitable for determining static corrections for deep seismic reflection surveys. The data was collected in eight profiles using 1C-24 channel geophones of 10 Hz at an interval of 3 km between stations whose spread length was 108 m at each station. Sledge Hammer acted as a source of seismic waves. Stack of 10-15 shots were made at each station for reverse and forward shooting to minimize background noise effect. Data was created on Vscoope database and exported to SEG-Y file which were transcribed to 2D Vista Seismic Processing software for first break picking. Picked first break time were loaded into spreadsheet where layers were picked and velocities calculated using time intercept method. A two layer model of the low velocity zone was obtained; the weathered zone and the semi-weathered zone. The third layer is a consolidated/ bedrock zone only observed from the velocities. Line 3 was observed to have the least thickness of approximately 16.0 m and while line 5 was the thickest averaging 34.4 m. The weathered zone of layer 1 of line 6 had the highest average velocity of 381 m/s while layer 1 of line 1 had the lowest velocity of 262.6 m/s. Layer 2 of line 2 had the highest average velocity of 1328.8 m/s while that of line 8 had the least average velocity of 878.2 m/s which all lie within the weathered zone of less than 1500 m/s. A qualitative interpretation of isopachs and isovel results show higher values of velocity and thickness in the north, north eastern and eastern region of study. Low velocity values are observed in the southern region of study. These are areas around Shompole and Nasurrana swamp as well regions towards Lake Natron. The thicknesses of low velocity layer are generally lower in the southern part but increase towards the north, around Lake Magadi and towards the east. It is observed that applied refraction statics due to low velocity layer is necessary for clear resolution of deep reflection seismic sections as processed seismic sections free of statics do not show clear structural and stratigraphic

reflections seismic sections, while seismic reflected sections whose statics are applied show clear structural, stratigraphic and lithological sections. These results show that the weathering zone could result in adverse effect on deeper reflection seismic data since it exists in Magadi basin. Therefore, to map deep features for hydrocarbon location, it is recommended that static correction be applied when processing deep seismic reflection data in this region.

CHAPTER ONE

INTRODUCTION AND LITERATURE REVIEW

1.1 Introduction

Seismic survey involves propagation of elastic waves within the subsurface by seismic energy sources. These sources include explosives, vibrator, weight-drop and a sledgehammer. The seismic response is simultaneously recorded by a number of receivers (geophones, seismometers) positioned along straight profile lines (2-D seismics) or over an area in 3-D seismic surveying and connected to a seismograph. During their propagation, seismic waves may be reflected, refracted or diffracted when elastic contrasts occur at boundaries between layers and rock masses of different rock properties (seismic velocities and/or bulk densities) or at man-made obstacles (Knödel *et al.,* 2007). This study was carried out in Magadi basin which lies in the Kenyan Rift basin. The area lies within an exploration field in Southern Kenya referred as BLOCK 14T where extensive seismic exploration activity is being done to locate features necessary for hydrocarbon storage. From previous studies, Rift Basin has been known to contain excellent hydrocarbon potential the world over when they are filled by syn-rift fluvio-lacustrine systems (Lambiase, 1995; Morley 1999; & Talbot *el al.,* 2004). Assuming favourable climatic and structural conditions during the deposition of the sediments that fill such basins, the resulting infill in some cases will develop functional petroleum systems owing to the close juxtaposition of good source and reservoir rock, (Lambiase, 1995). Such rift basins exist in East African region specifically in the Cenozoic East African Rift System (EARS) that is described by Gregory (1921) as a comparative trench with fairly regular walls. EARS is an elongated system of normal faults that stretches more than 3500 km and is connected to the world wide system of oceanic rifts via the Afar Triangle to the Gulf of Eden and the Red Sea, (Baker & Wohlenberg, 1971). It is divided into two main arms, the late Miocene western arm, a volcanic dry and largely submerged under the great lakes of East Africa and the Eastern arm which comprises the Ethiopian and the Kenyan Rifts where the BLOCK 14T in Magadi basin lies. Morley *et al.* (1999) observed that the

Eastern arm of the EARS formed during the Paleocene time is volcanically-wet and punctuated by a number of small, shallow fresh water to hyper–saline (Lake Magadi), ephemeral to perennial lakes**.**

1.1.1 Study Area

Magadi basin is located in Kajiado County, approximately 100 km from Nairobi. The study area is bounded by latitudes 1^0 40’S and 2^0 10’ S and Longitudes 36^0 00’ E and 36^0 30’ E as in Figure 1.1. It is in the Southern part of the Gregory Rift of continental rift type. It extends from the Magadi to Natron, a quaternary basin in the south to Baringo and Suguta grabens in the north; a complex grabens bisecting the Kenya domal uplift. The lake Magadi is located in a broad flat depression with the lowest point in the Southern part of the Kenya Rift Valley.

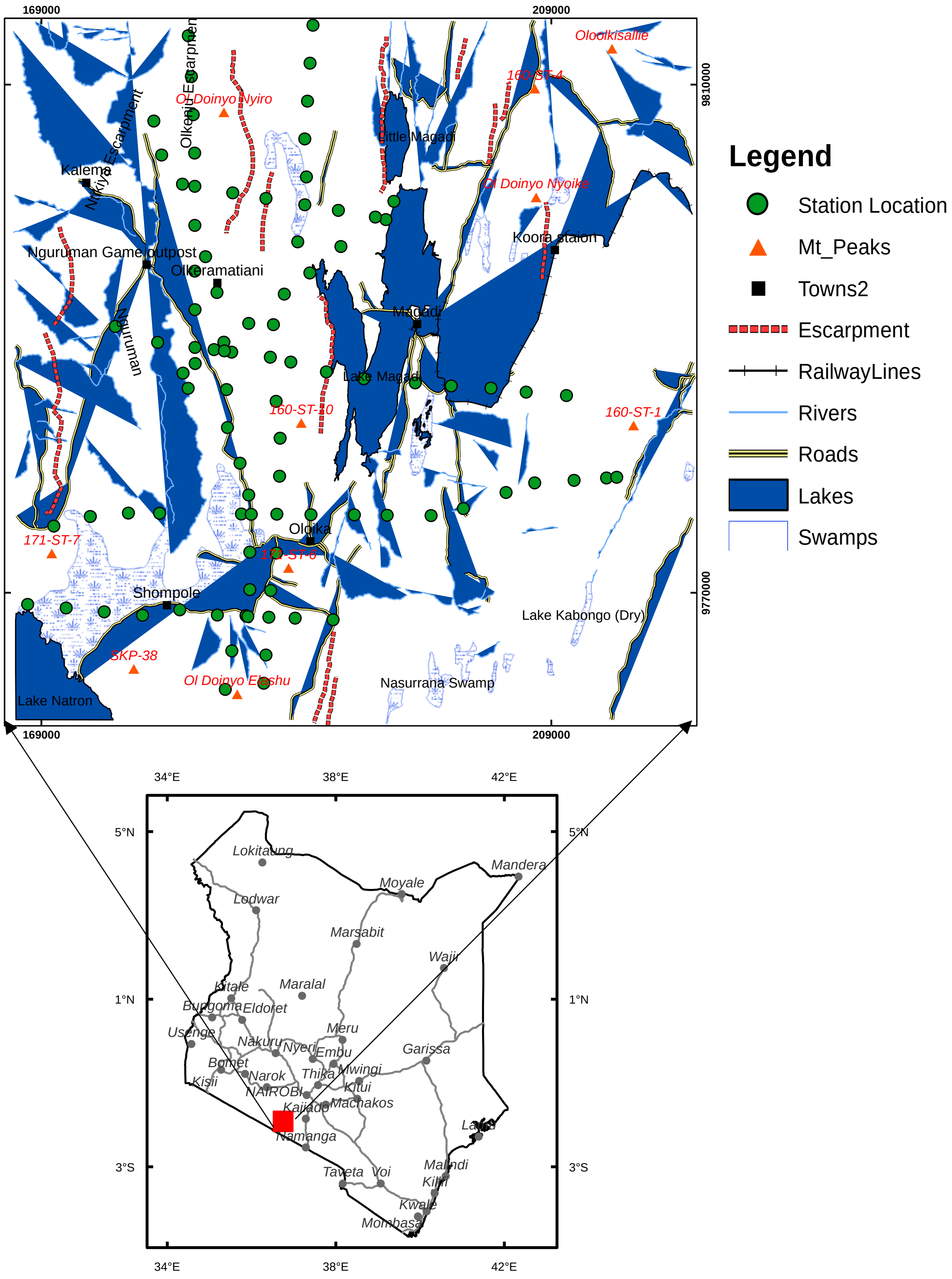

Figure 1. 1: The study area of Magadi and shallow seismic refraction locations.

1.1.2 Geology of Study Area

The Magadi basin is classified into three formations by Baker (1958, 1963) namely; Precambrian metamorphic rocks, Plio-Pleistocene volcanics, the Holocene to Recent Lake and fluvial sediments as illustrated in the geological map (Figure 2.1). The basement rocks outcrop in the region west of the Nguruman escarpment. These rocks consists mainly of regular banded schists, gneisses and muscovite-rich quartzites. Baker (1958) found that the olivine basalt layers of the Kirikiti platform are interbedded with conglomerates; gravels and sands deposited between different eruption episodes. Three central volcanoes exist; olorgesailie, Oldoinyo Nyokie and Shompole (Figure 1.1). Olorgesailie is the highest. Its lava composition consists of olivine basalts, alkali trachyte and nephelinite. Further south, the Lenderut volcano dated 2.5 Ma has basalt and andesite lavas, while Shompole dated 2.0 Ma consists of carbonates and nephelinite rocks (Baker, 1963). The most extensive volcanic activity in the area occurred between 1.4 and 0.7 Ma, (Crossley, 1979). During this period the Magadi Trachyte series were formed and consisted of alkali lava sheets extending many kilometers that overlie most of the volcanics in the area. The Magadi area is largely covered by quaternary sediments that overlie extensive Pleistocene lavas. The trachyte lava overlies Pliocene olivine basalts and nephelinites that rests on the archean basement. A dense network of grid faults, mainly the north south trending fault scarps, affects the area and control the occurrence of geothermal manifestations (Riaroh & Okoth, 1994). Magadi trachytes were followed by development of ash and lava vents and small obsidian lava volcano Oldoinyo Nyokie marking the end of volcanism in the southern Kenya Rift. Lacustrine and fluviatile sediments were the last geological formations. Lake bed lie in the bottom of fault troughs and depressions mostly covered by alluvial silts, clays and boulder beds. These are exposed around Lake Magadi mainly in the Eastern trough of the lake. The fluviatile sediments are mainly located in the Ewaso Ngiro Basin. Other superficial deposits are the alluvium and soil filled Kordjya basin and Kora Basin, (Baker, 1958).

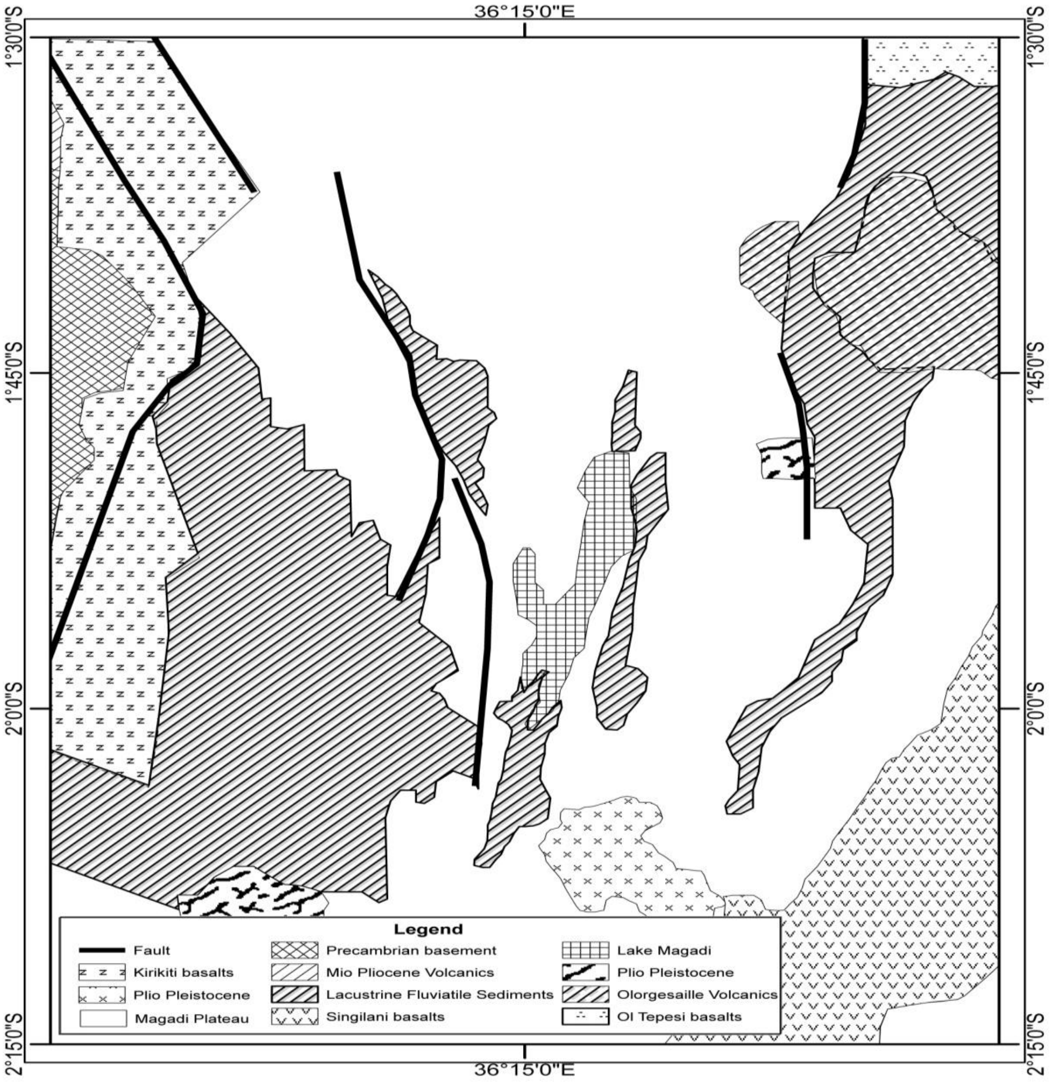

Figure 1. 2: Geological Map of Magadi (Simplified from Baker, 1958; 1963).

1.1.3 Structural Setting of Magadi area

Magadi basin is located within the Kenya portion of the East African Rift, commonly called Kenya Rift. It covers the entire area referred as the South Kenya Rift, a southern portion of approximately 900 km long Kenya Rift that extends from Lake Turkana in the North to Lake Natron on Kenya - Tanzanian border in the south. The rift formation and development began about 30 million years ago in Lake Turkana area and then migrated southward being more intense about 14 million years ago, during Miocene period. The extensional tectonics accompanied by faulting, uplift, lava flows, and volcanism formed the Kenya Rift. The main rift is bounded by N-S running major rift scarps that depict different tectonic style on the two sides, (Leat, 1984). In the southern section of the Kenya Rift referred as the Magadi-Natron Basin, the trend of the Kenyan Rift reverts back to N-S orientation (Figure 1.3) with the predominant major faults to small faults in the trough, (Kenya Tertiary Rift Study, 1987). These major N-S faults include the Naitami, Endosapia and Longitoto faults. The Magadi basin is presumably asymmetrical and bordered to the west by the Ngurumani Escarpment and to the east by a large faulted flexural zone consisting of a broad area marked by numerous faults that spread most of the trough, (Riaroh & Okoth, 1994). Ngecu (1999) observed that the Magadi-Natron basin is about 69 km wide graben and is flanked by plateaus having an elevation of about 1500-2000 m above sea level. The post-volcanic infill in the Magadi basin comprises of Plio-Pleistocene sedimentary formations with Munya-wa-Gacheru formation which extends across the Kedong Valley and Suswa plains to the west and Olorgesailie formation that extends southwards to Mount Olorgesailie, (Owen *et al.*, 2011). The Olorgesailie formation famous for lower paeleolithic archeological sites that contain abundant acheulian artefacts and fossil vertebrates is fluvio-lacustrine formation comprising predominantly of laterally extensive diatomaceous and tuffaceous silts and pedogenetically modified clays and silts that sit on trachytes and basalts, north of Mount Olorgesailie, (Owen *et al.*, 2011). South of Mount Olorgesailie are well defined Green, High Magadi and Oloronga beds formally known as the Chert Series that form the infill that extend to lake Natron on the Kenya-Tanzania Border. The Oloronga beds form the oldest sediments in Magadi basin. The west wide thickening is approximately 35 m, (Baker, 1958).

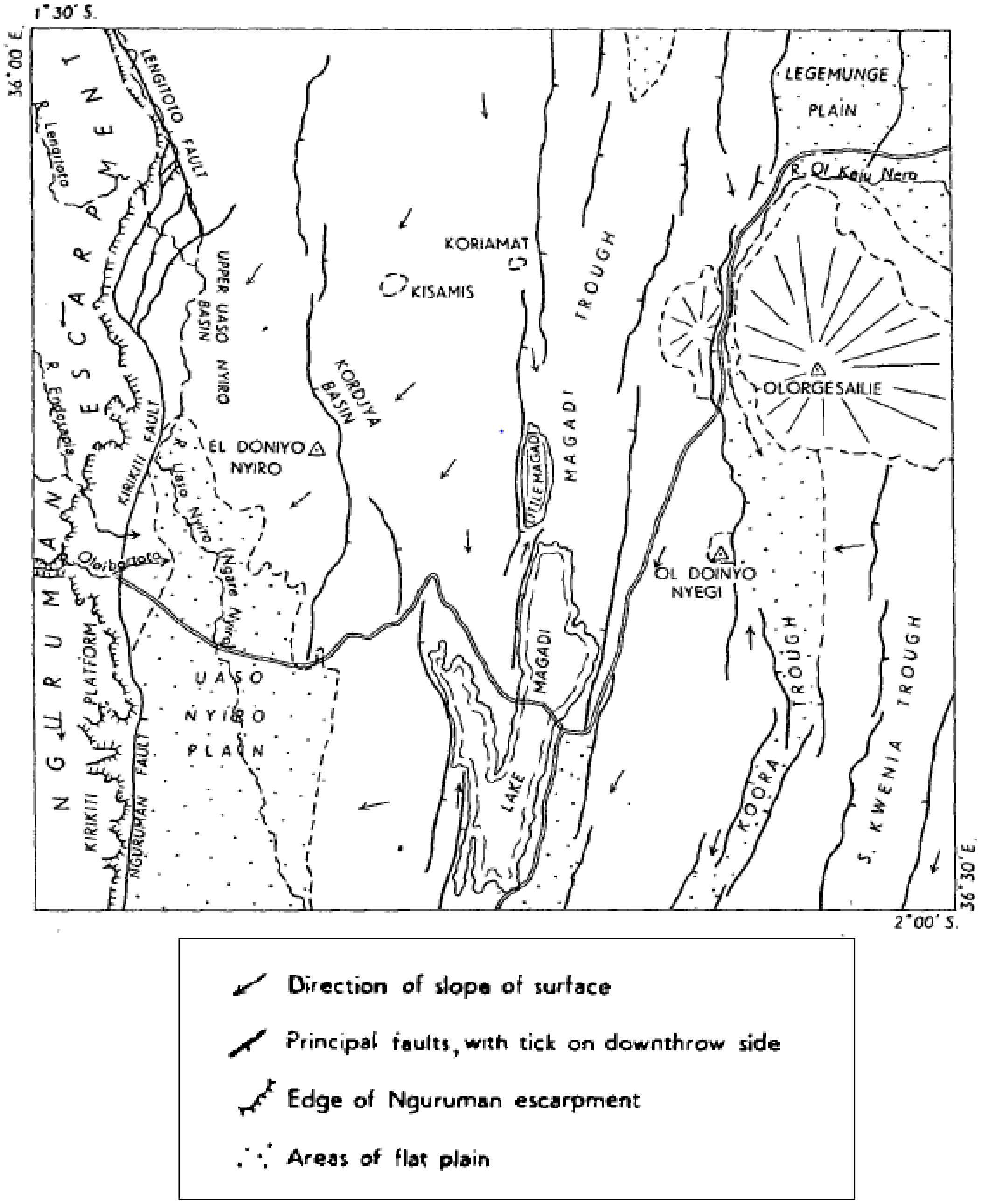

Figure 1. 3: Major Structures of Magadi Area, (Baker, 1958).

It is in this area that the weathered zone has been mapped by shallow refraction method to determine the trend, its thickness, the depth to the bedrock and its velocity. An effect of the low velocity layer on deep reflection seismic data was investigated to show that the application of statics is significant for clear mapping of geological features necessary for hydrocarbon storage during the processing and interpretation of deep reflection seismic data.

1.2 Statement of the Problem

The aim of reflection seismic data processing is to obtain an accurate image of the subsurface that is critical for interpretation during exploration for hydrocarbons and other geological targets. The target of seismic interpretation is identifying features which could reveal the oil and gas prospects of the region of interest. Some of the common ways of finding potential reservoirs is to look for clearly mapped structural and stratigraphic traps through a series of processing steps of which statics correction is key. The statics are the highly variable travel times of reflected waves accumulated during their propagation within the low velocity zone/near surface layer. The low velocity zone is loosely consolidated and significantly more non-uniform compared to the deeper layers. It is heterogeneous in composition and brings wide range of velocities causing variable delay in travel time of the reflected seismic waves. If this time shifts are not mitigated against, static shifts are capable of completely disrupting the coherence of reflection patterns and loss of depth resolution leading to unclear mapped images and hence erroneous interpretations, (Stein *et al.,* 2009). Due to exploration activities occuring in Magadi basin, proper computed statics of the weathered zone will be useful for clear mapping of the deep underlying structures responsible for oil and gas reservoir.

1.3 Justification

The thickness of weathered zone decreases over hilltops and increases at stream valleys, and changes radically over short distances. Magadi basin is not an exception. These lateral changes bring significant problems in areas where paleotopographic relief are frequently encountered on the surface. Because of small thickness of overburden and its continued disintegration, the weathered layer has low velocities and large energy distribution as a result of frictional losses in unconsolidated material. A good knowledge of the thickness to the bedrock and the trend of the weathered zone is of immense advantage to computing static correction that will help in temporal and spatial resolution of the seismic reflection data analysis in any exploration field such as Magadi basin. This helps in clear mapping of subsurface geological structures necessary for oil and gas reservoir.

1.4 Hypothesis

There is no variation of the velocity of the weathered zone of the Magadi area.
The weathered zone of Magadi area has uniform thickness.

1.5 Objectives

1.5.1 General objectives

The main objective of the study is to carry out shallow seismic refraction surveys in the Magadi basin.

1.5.2 Specific Objectives

1. To determine the seismic velocity and the trend of the weathered zone of the Magadi basin
2. To determine the average depth to the bedrock of the BLOCK 14T in Magadi basin.
3. To demonstrate the effect of static correction on deep reflection seismic data due to low velocity layer.

1.6 Literature Review

Large scale seismic refraction profiles experiments were recorded across the region by the Kenya Rift International Seismic Project (KRISP) in 1985 and 1990. The data provided a good picture of the overall crustal structure of the region. It was observed that the variation of the crustal structure across the rift are surprisingly large, generally correlating with the elevation of the Rift Valley floor, (Mechie *et al.,* 1994). In the southern part, the seismic P-wave velocity information shows that the crustal boundary outside the rift occurs at 42 km depth. Low P-waves velocities (7.5-7.7 km/s) have been detected below the rift, while outside the rift, P-wave velocities appear normal, that is, 8.0-8.1 km/s, (Bonjer *et al.,* 1970; Backhouse & Long, 1976). Most of the seismic studies carried out were for mapping the crustal structure and the mantle. This project will focused mainly on studying characteristics of the weathered zone that has great impact on deep reflection seismic data normally acquired for locating geological features necessary for hydrocarbon location. The near surface zone has various properties. It is usually aerated, loose, unconsolidated with abnormally low velocities, and variable thicknesses, densities and lithologies. The number of refractors (layers) present in the weathering zone can be determined explicitly by examining the differences between first-arrival travel times on records from overlapping spreads. Alaminiokuma and Amonieah (2012) geostatistically developed near surface structural model from a sample density of 36 Uphole/LVL survey points to determine the properties of the weathered layer. The results served as baseline data for future 4D seismic data acquisition for accurate mapping of the deep underlying structures for oil and gas exploration in the North-Central part of the Niger Delta. Rather than finding velocities and thicknesses of layers, shallow seismic refraction data is commonly used in oil and gas exploration with the aim of computing static correction for seismic reflection surveys. However, in order to obtain static correction the knowledge of the velocity and thickness of the weathered layers is significant. The static corrections obtained are used to adjust travel times for passage through the thick, low-velocity "weathered zone" overlying solid rock. Lawton observed that absolute values of the static corrections of less than 10ms, had greater effect on reflection travel times than does the surface topography and increased in response to the increasing thickness of glacial overburden in Southern Alberta, Calgary, (Lawton, 1989).

Knowing the extent of weathered zone in terms of thickness is also key in engineering applications. Geological survey of India and the central Water and Power research Station, Poona used seismic refraction to determine the depth to a hard rock for dam and bridge sites using three seismic lines around 110 m to 160 m using 24 channel geophones with a spacing of 5m.They obtained the depth to the bedrock for the foundation to be 20 m, 26 m and 18 m at three pier locations and also showed a regional feature (depression) of a low velocity channel in the center of the river which had been filled by flowing pebbles and boulders, (Rao *et al.,* 2004).

Kolawole *et al.* (2012) carried out downhole refraction in Niger Delta Basin in which they analyzed data sets from 15 refraction points positioned at 4km grid intervals. A 3-layer model for two consecutive points and 2-layer model for the other 13 refraction points was observed. Correlation and analysis of observed lithological successions, velocities and depths of boundaries suggested an irregularity caused by faulting along the true base of weathering as a possible origin of the event. Anomohanran, (2014) and Saha *et al*., (2012) investigated the velocity and depth of the weathered layer using a downhole seismic refraction technique in Escravos and Assam Basin in Nigeria respectively. Weathered layer thickness in Escravos averaged depth of 3.68 m while analysis of velocity-thickness map of all the layers in Assam Basin area showed significant variations, both in local as well as regional scale giving some information on low velocity layer characteristics near Naga thrust area, (Saha *et al.,* 2012).

Having determined the trend, thicknesses and velocity of the weathered zone, the effect of static corrections on reflection seismic data was investigated. Static corrections are corrections applied to seismic data to compensate for the effects of variations in elevation, weathering thickness, weathering velocity, with reference to a datum. Magadi basin has sharp variation of the near-surface structure which was caused by faulting, uplift, lava flows, and volcanic deposits and therefore requires static correction. If static corrections are not properly applied and handled during the processing of reflection seismic data, then a whole catalog of problems will affect the interpretations of the seismic sections, including lines with variable elevations and false structural anomalies. Therefore, proper statics solutions are desirable for obtaining high-resolution sections which can be used for both stratigraphic and lithologic interpretations for clear mapping of hydrocarbons. As for the deep reflection seismic data, proper statics solutions are important in order to obtain the final clear and accurate images of the crust and upper mantle, (Zhu *et al.,* 2014).

1.7 Theoretical Review

1.7.1 Introduction

The basic principle of all seismic methods is the controlled generation of elastic waves by a seismic source in order to obtain an image of the subsurface. Seismic waves are pulses of strain energy that propagate in solids and fluids. In seismic surveying, seismic waves are created by a controlled source and propagate through the subsurface where some waves will return to the surface after refraction or reflection at geological boundaries within the subsurface while others may be transmitted or absorbed in the subsurface. Instruments distributed along the surface are used to detect the ground motion caused by these returning waves and hence measure the arrival times of these waves at different ranges from the source. These travel times may be converted into depth values enabling systematic mapping of the distribution of subsurface geological interfaces. This geological interfaces are derived from paths that fall into two main categories; refracted or headwaves and the reflected waves.

1.7.2 Propagation of Elastic Waves

Propagation of elastic waves within the subsurface causes the particle motion of the medium as well as volume and shape changes. A mathematical expression of particle displacement and wave velocity *v* as functions of space (x, y, z) and time *t* is the wave equation. The wave equation is based on the theory of elastic continua which relates deformation (strain) and stress. Equation (1) describes the wave propagation in a homogeneous isotropic elastic medium, where φ can be a vector or a scalar, for example, a component *u* of the particle displacement.

$$\nabla^2\varphi = \frac{\partial^2\varphi}{\partial x^2} + \frac{\partial^2\varphi}{\partial y^2} + \frac{\partial^2\varphi}{\partial z^2} = \left(1/v^2\right)\frac{\partial^2\varphi}{\partial t^2} \qquad \ldots\ldots\ldots\ldots\ldots\ldots\ldots\ldots\ldots\ldots\ldots\ldots .. \; 1$$

The solution of the wave Equation is that of a planar wave with harmonic ground motion.

$$\varphi(t) = A\cos(\theta + \omega t) \qquad \ldots\ldots\ldots\ldots\ldots\ldots\ldots\ldots\ldots\ldots\ldots\ldots\ldots\ldots\ldots\ldots\ldots.. \ 2$$

A is amplitude, *θ* is the phase difference and *ω* the angular frequency of the wave. An additional phase term *kz* shows a generalized form in the *z* direction of wave propagation (1D case):

$$\varphi(t) = A\cos(\omega t + kz + \theta) \qquad \ldots\ldots\ldots\ldots\ldots\ldots\ldots\ldots\ldots\ldots\ldots\ldots\ldots..\ldots \ 3$$

where k is the wave number (k=2π/λ) with λ being the wavelength and z the direction of wave propagation, (Knödel *et al.*, 2007). To describe the seismic wave propagation it is important to know the behavior of seismic waves at an interface. Huygens' principle suggests that when an advancing planar wavefront arrives at a boundary between two layers of different elastic properties, every point at this boundary acts as a source of a secondary spherical wave. These secondary waves overlap and new wavefronts defined by the envelope to all the secondary waves are formed - a reflected wavefront in the upper halfspace and a transmitted (refracted) wavefront in the lower halfspace. The ratio between reflected and transmitted energy and, hence, the ratio of the wave amplitudes depends on the elastic properties of both layers, and is expressed as their acoustic impedance.

The acoustic impedance of a layer is the product of its seismic velocity and the bulk density *(z=ρv)*. Based on the contrast in acoustic impedances at a seismic boundary, reflection and transmission coefficients can be calculated. These values define that part of energy which is reflected or transmitted. A reflection coefficient of value "1" (theoretically) means that all incident seismic energy is reflected. Keeping the boundary conditions for displacement and stress one can state: The reflection coefficient R (reflectivity) and transmission coefficient T (Transmissivity) of the seismic waves in terms of the amplitude are given by equations (4) and (5)

$$R = \frac{A_{reflect}}{A_{Incident}} \qquad \ldots\ldots\ldots\ldots\ldots\ldots\ldots\ldots\ldots\ldots\ldots\ldots\ldots\ldots\ldots\ldots\ldots\ldots \; 4$$

$$T = \frac{A_{Transmitted}}{A_{Incident}} \qquad \ldots\ldots\ldots\ldots\ldots\ldots\ldots\ldots\ldots\ldots\ldots\ldots\ldots\ldots \; 5$$

The coefficients R and T can be expressed in terms of acoustic impedance defined as the product of density and velocity, $Z = \rho v$ .The reflection coefficient R in the general case is;

$$R = \frac{\left(Z_2/Z_1\right) - \sqrt{1-(n-1)\tan^2 \alpha_i}}{\left(Z_2/Z_1\right) + \sqrt{1-(n-1)\tan^2 \alpha_i}} \qquad \ldots\ldots\ldots\ldots\ldots\ldots\ldots\ldots\ldots\ldots\ldots\ldots \; 6$$

Where $n = (V_2/V_1)^2$ and α_i is the angle of incident of the wave ray. For a normal incident, $\alpha_i = 0$ and the reflection becomes;

$$R = \frac{Z_2 - Z_1}{Z_2 + Z_1} \qquad \ldots\ldots\ldots\ldots\ldots\ldots\ldots\ldots\ldots\ldots\ldots\ldots\ldots\ldots\ldots \; 7$$

While the transmission coefficient is;

$$T = \frac{2\sqrt{Z_1 Z_2}}{Z_2 + Z_1} \qquad \ldots\ldots\ldots\ldots\ldots\ldots\ldots\ldots\ldots\ldots\ldots\ldots\ldots\ldots\ldots \; 8$$

1.7.3 Seismic Refraction Surveying

So far we have analyzed propagation of elastic waves within the subsurface. In a seismic survey elastic waves are generated by different energy sources such as vibrator, weight-drop and sledgehammer. The seismic response is simultaneously recorded by a number of receivers positioned along straight profile lines (2-D seismics) or over an area in 3-D seismic surveying and connected to a seismograph. The signals of individual geophones or groups of geophones are recorded by a seismograph, processed and displayed in seismic sections to image the subsurface structure. Seismic refraction method uses the process of critical refraction to determine the depth and dip of layer boundaries including the different velocity of layers. According to Snell's law, an incident P-wave is split in both refracted and reflected P- and S-waves at each layer boundary as shown in Figure 1.4. In refraction seismics, "head waves" which arise at the interface between two layers when refraction at the critical angle occurs are used. The interaction of the critical refracted wave with the layer interface produces secondary waves that are transmitted as wavefronts back to the surface. These head waves can be registered with geophones at the earth's surface. The main aim of refraction surveys is to use head waves to determine the depths to layers, the refractor topography (dip of layers) and layer velocities, (Knödel *et al.*, 2007).

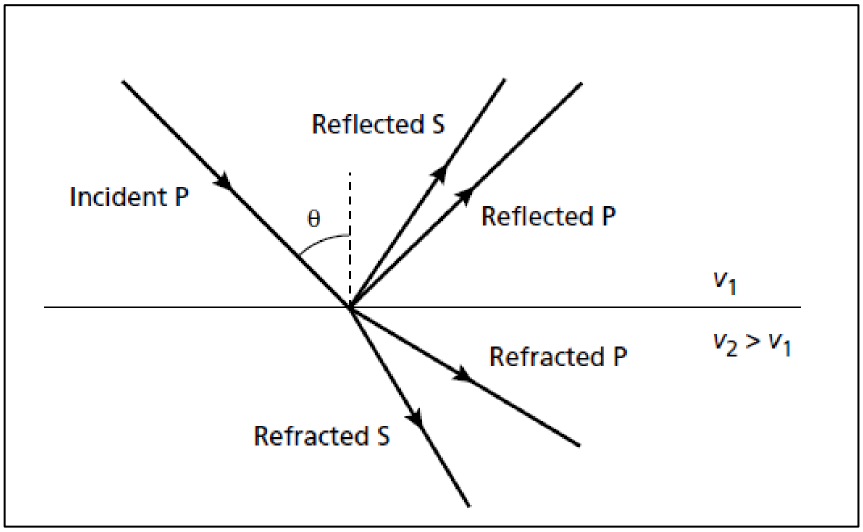

Figure 1. 4: Reflected and refracted P- and S-wave rays generated by a P-wave ray obliquely incident on an interface of acoustic impedance contrast, (Keary et al., 2005).

In refraction seismogram sections, the arrivals of head waves appear beyond a certain (critical) distance $x_{critical}$ only, but are overlain by the events of subcritical and overcritical reflections at the layer boundary. Their arrivals are clearly recognizable as first breaks on the seismogram at geophone offsets greater than the crossover distance, $X_{crossover}$. At the crossover distance the direct wave and the refracted wave arrive at the same time. $X_{crossover}$ will always be greater than twice the refractor depth (Knödel *et al.*, 2007). The time difference between the time break is a linear function of the offset as well as velocity and dip of the layer boundary. The intercept time Ti is the interpolated intersecting point of this linear function to an offset equal to zero and directly related to the depth of the refractor below the shot point. The velocity in the (lower) refracting layer is derived from the reciprocal slope of the traveltime curve. In the case of dipping layers the velocity value derived from the traveltime curve is an apparent velocity. To determine true velocities, depth, and dip of layers; an average of velocity, depth and dip of at least two overlapping traveltime curves and equations derived from forward and reverse direction shots are necessary.

$$T_d = \frac{\sin(i_c + \alpha)}{V_1} x + \frac{2Z_d \cos(i_c)}{V_1} \qquad \ldots\ldots\ldots\ldots\ldots\ldots\ldots\ldots\ldots\ldots\ldots\ldots \; 9$$

$$T_u = \frac{\sin(i_c - \alpha)}{V_1} x + \frac{2Z_u \cos(i_c)}{V_1} \qquad \ldots\ldots\ldots\ldots\ldots\ldots\ldots\ldots\ldots\ldots\ldots\ldots\ldots \; 10$$

Equations (9) and (10) shows traveltime equations of a critical refracted wave for a two layer case with dipping planar interfaces. T_d and T_u are traveltimes of the shot downdip and updip, Z_d and Z_u are the depths below the shotpoint perpendicular to the refracting interface for updip and downdip respectively, i_c the critical angle, α the layer dip and V_1 the velocity of the direct wave in the first layer, (Knödel *et al.*, 2007).

1.7.4 Geometry of Seismic Refraction Ray Paths

Consider a simple geological section (Figure 1.5) involving three homogeneous layers of seismic velocities V_0, V_1 and V_2 and their corresponding ray path travel time curves (Figure 1.6). The layers are separated by a horizontal interface at a depth Z_0 and Z_1, the compressional average wave velocity being higher in the underlying layer (i.e. $V_2 > V_{1>} V_0$). The general assumption of the subsurface geological geometry being; its composed of a series of layers, separated by planar and possibly dipping interfaces, i.e., the dip angle is very small (Figure 1.5), within each layer seismic velocities are constant, the velocities increase with layer depth and the ray paths are restricted to a vertical plane containing reversed sets of the profile line, i.e. there is no component of cross-dip, (Keary *et al.*, 2005).

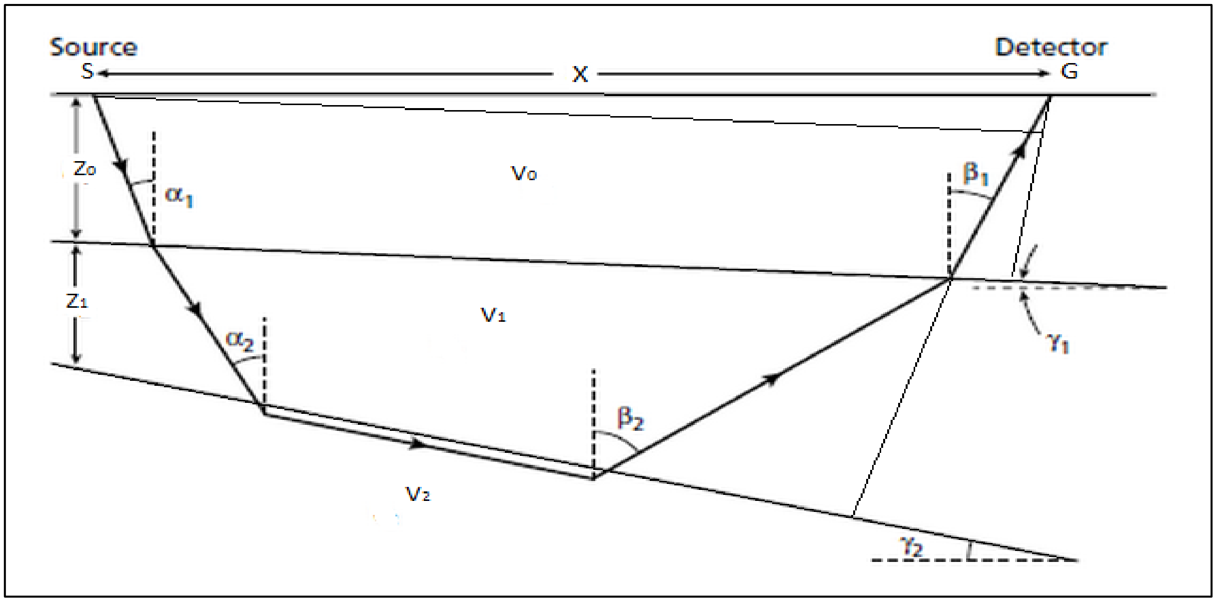

Figure 1. 5: Geometry of the refracted ray path through a three layer of the weathering zone, dipping model, (after Johnson, 1976).

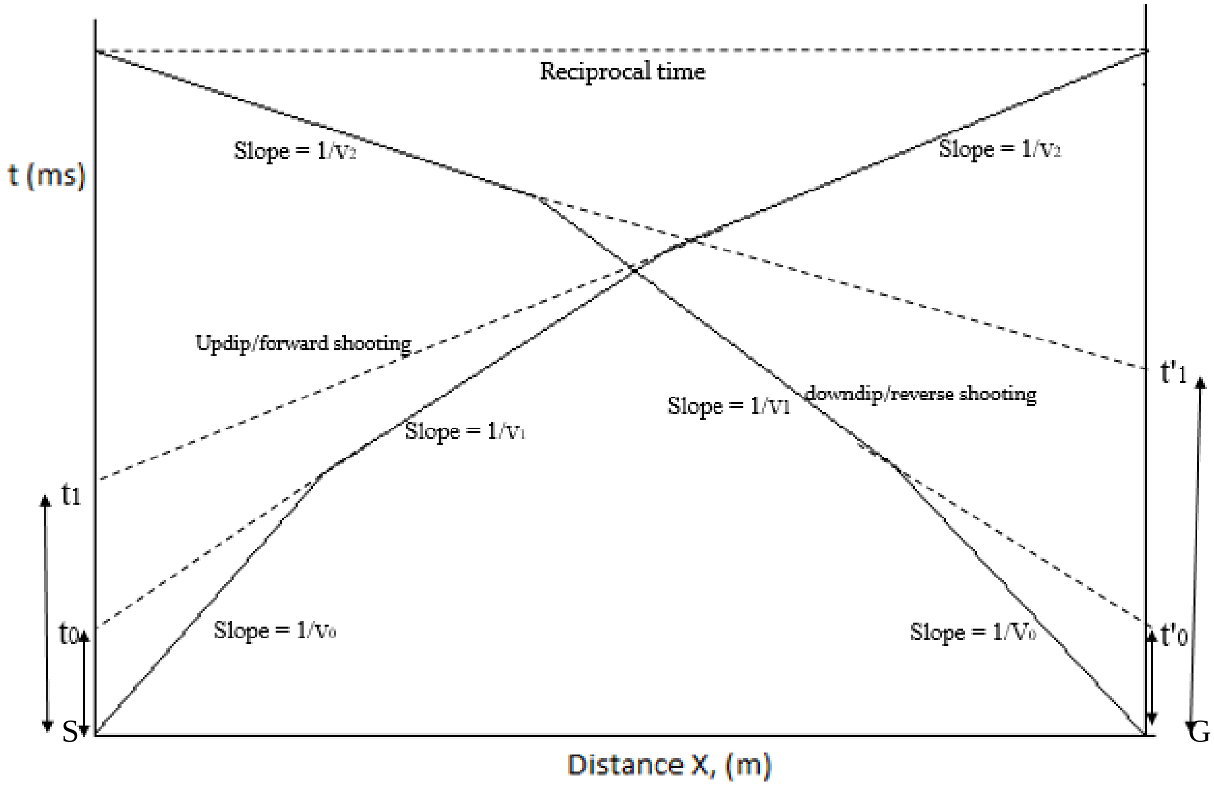

Figure 1. 6: Ray path travel-time curves for head wave arrivals from a dipping refractor in the forward and reverse directions along a refraction profile line, (Telford et al., 1990).

From near surface seismic source S, there are three types of ray path by which energy reaches the surface at a distance from the source where it is recorded at a horizontal distance x (SG) by a detector G, from the source. The direct ray travels along a straight line through the top layer from source to the detector at velocity V_0. The refracted ray travels its entire path at the top layer at velocity V_1 and V_2 in the third layer. The refracted ray travels obliquely down to the interface at velocity V_0, along a segment of the interface between top layer and second at a higher velocity V_1, and back up through the upper layer at V_0. Some of the refracted wave travels from layer 1 at V_0 and second layer at V_1 and is critically refracted when it reaches the third layer where it travels at much higher velocity V_2. The travel time of direct ray is given by;

$$t_{direct} = \frac{x}{V_1} \qquad \text{………………..……………….……………….…} \qquad 11$$

which defines a straight line slope passing through the origin of the time-distance (T-X) graph, (Keary *et al.*, 2005). The general form of the equation for the travel-time t_n of a ray critically refracted in the *n*th dipping refractor is given by Johnson's, (1976) relation;

$$t_n = \frac{x\sin\beta_1}{V_1} + \sum_{i=1}^{n-1} \frac{Z_i(\cos\alpha_i + \cos\beta_i)}{V_i} \qquad \text{………….……………………………} \qquad 12$$

where Z_I is the vertical thickness of the *i*th layer beneath the shot, V_I is the velocity of the ray in the *i*th layer, α_i is the angle with respect to the vertical made by the downgoing ray in the *i*th layer, β_i is the angle with respect to the vertical made by the upgoing ray in the *i*th layer, and *x* is the offset distance between source and detector. Equation (12) is comparable with equation (13) for horizontal layers, the only differences being the replacement of θ by angles α and β that include a dip term.

$$t_n = \frac{x}{V_n} + \sum_{i=1}^{i=n} \frac{2Z_i\cos\theta_{in}}{V_i}, \qquad \theta = \mathrm{Sin}^{-1}(V_i/V_n) \text{ ……………………..….. } 13$$

Where θ is the critical angle of refraction in the nth layer. In the case of shooting downdip, for example (in Figure 1.5), $\alpha_i = \theta_{in} - \gamma_i$ and $\beta_i = \theta_{in} + \gamma_i$, where γ_i is the dip angle of the *i*th layer and $\theta_{in} = \sin^{-1}(V_1/V_n)$ as before. Z_i is the vertical thickness rather than the perpendicular or true thickness of a layer (hi), (Keary *et al.*, 2005). However, if γ is small enough, $Z_i = h_i$.

Shooting downdip and updip along the forward and reverse profile for two layer dipping model, equation (12) reduces to equations (14) and (15) respectively for downdip and updip travel times.

$$t_d = \frac{x\sin(\theta+\gamma)}{V_0} + \frac{2Z\cos\theta}{V_0} \qquad \text{...…………………………………………………} \qquad 14$$

$$t_u = \frac{x\sin(\theta-\gamma)}{V_0} + \frac{2Z^1\cos\theta}{V_0} \qquad \text{……………………………………………....…} \qquad 15$$

The updip, V_u and downdip, V_d velocities in the second layer are given by;

$$V_u = \frac{V_1}{\mathrm{Sin}(\theta-\gamma)}, \qquad V_d = \frac{V_1}{\mathrm{Sin}(\theta+\gamma)} \quad \ldots\ldots\ldots\ldots\ldots\ldots\ldots\ldots\ldots\ldots\ldots\ldots\ldots\ 16$$

The inverse of the slope of the T-X graph (Figure 1.6) gives the apparent velocity of the first layer in the updip and downdip directions respectively. Subsequently, the inverse of the second layer and third layer are the apparent velocities of the second and the third layer respectively. The second term in equations (14) and (15) represent the intercept times for forward (updip) and reverse (downdip) and are used to calculate the thickness of the LVL in the updip and downdip respectively as in equation (22).

For reversed set of profiles, the angles α and β are given by Johnson's (1976) relation:

$$\mathrm{Sin}\ \alpha_i = (V_0/V_u), \qquad \mathrm{Sin}\ \beta_i = (V_0/V_d) \ \ldots\ldots\ldots\ldots\ldots\ldots\ldots\ldots\ldots\ldots.\ 17$$

Where V_u and V_d are apparent velocities in the updip and downdip directions. The layer dip γ is given:

$$\gamma = (\alpha - \beta)/2 \quad \ldots\ldots\ldots\ldots\ldots\ldots\ldots\ldots\ldots\ldots\ldots\ldots\ldots\ldots\ldots\ldots\ldots\ldots..\ 18$$

If the refractor dip is small, cos $\gamma \approx 1$ (for example, if $\gamma < 15$, cos > 0.96), Lowrie, (2007), Yilmaz, (2000), and Telford, (1990) suggests an approximate formula for the true velocity of the second layer as;

$$\frac{1}{V_2} = \frac{1}{2}\left(\frac{1}{V_u} + \frac{1}{V_d}\right) \ \ldots\ldots\ldots\ldots\ldots\ldots\ldots\ldots\ldots\ldots\ldots\ldots\ldots\ldots\ldots\ldots\ (19)$$

Telford, (1990) further suggests a simpler approximation for V_2 can be obtained by applying binomial theorem to equation (16) and assuming that higher powers of γ are small hence negligible;

$$V_d = \frac{V_1}{\mathrm{Sin}(\theta)}\left(\cos\gamma + \cot\theta \sin\gamma\right)^{-1} \ldots\ldots\ldots\ldots\ldots\ldots\ldots\ldots\ldots\ldots\ldots\ldots\ldots\ldots\ldots\ 20$$

Equation (20) reduces to equation (21) after further manipulation as suggested by Telford, (1990) and Reynolds, (1998) and therefore the velocity of the second layer can be given as;

$$V_2 = \tfrac{1}{2}\left(V_d + V_u\right) \qquad \ldots\ldots\ldots\ldots\ldots\ldots\ldots\ldots\ldots\ldots\ldots\ldots\ldots 21$$

The second term in equations (14) and (15) are used to obtain the average thickness Z_0 and Z_1 of each layer for the reversed set of profiles from the point of intersection of the two layers by using the time intercept method for a horizontal layer or for a dip angle small enough and approximately equal to one, ($\cos\gamma \approx 1$).

$$Z_0 = \frac{t_0}{2}\left(\frac{V_1 V_0}{\sqrt{\left(V_1^2 - V_0^2\right)}}\right) \qquad \ldots\ldots\ldots\ldots\ldots\ldots\ldots\ldots\ldots\ldots\ldots\ldots\ldots\ldots 22$$

$$Z_1 = \frac{1}{2}\left[t_1 - \frac{2Z_0\sqrt{\left(V_2^2 - V_0^2\right)}}{V_2 V_0}\right]\frac{V_2 V_1}{\sqrt{\left(V_2^2 - V_1^2\right)}} \qquad \ldots\ldots\ldots\ldots\ldots\ldots\ldots\ldots\ldots\ldots 23$$

where: t_0 and t_1 are the intercept times on the Distance-Time graph. V_0, V_1 and V_2 are the velocity of the weathering layer, semi-weathering layer and the bedrock respectively. Equations 22 and 23 are used in obtaining thicknesses in a horizontal layer for three layer model.

The total thickness of the weathering layer is therefore;

$$Z_W = Z_0 + Z_1 \text{ (m)} \qquad \ldots\ldots\ldots\ldots\ldots\ldots\ldots\ldots\ldots\ldots\ldots\ldots\ldots\ldots\ldots\ldots 24$$

For multiple horizontal layers, the thickness of each layer for $n > 1$ can be calculated from

$$Z_n = \left[\frac{T_n}{2} - \sum_{k=1}^{n-1}\frac{Z_k}{V_k}\cos\theta_{k(n+1)}\right]\frac{V_n}{\cos\theta_{n(n+1)}} \qquad \ldots\ldots\ldots\ldots\ldots\ldots\ldots\ldots\ldots\ldots 25$$

The near surface trend of the weathered zone and the velocity of the two layers can be seen more clearly when plotted in surfer by a geostatistical process of Kriging. The kriging technique is an interpolation estimator used to find the best linear unbiased estimate. The general equation of the Kriging estimator is:

$$Z^*(x_p) = \sum_{i=1}^{n} \lambda_i Z(x_i) \qquad \ldots\ldots\ldots\ldots\ldots\ldots\ldots\ldots\ldots\ldots\ldots\ldots\ldots\ldots\ldots\ldots\ldots\ldots\ldots\ldots\ldots \; 26$$

Where $Z^*(x_p)$ is the krigged value at location x_p, $Z(x_i)$ is the known value at location x_i, λ_i is the weight associated with the data, (Gooverts, 1997).

1.7.5 Seismic Instrumentation

The conversion of ground motion to an electric signal requires a transducer which is sensitive to some components of the ground motion, and can record the required range of frequencies and amplitudes without distortion. As the ground oscillates, it is possible to measure the displacement, velocity or acceleration of the ground particles as the wave passes using a device known as seismometer or geophone shown in Figure 1.7, (Keary *et al.,* 2005).

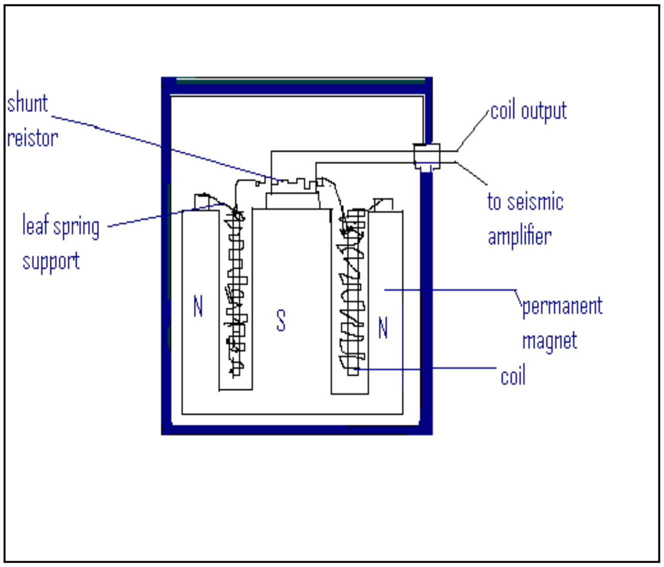

Figure 1. 7: A moving coil geophone, (Keary and Brooks, 2005)

The main parts of the geophone are: the moving mass, made up by the coil and the "former" on which it is wound; the coil suspension, two springs, one at the top and one at the bottom, to avoid lateral displacement of the coil; the case, with the magnet and polar pieces inside a cylindrical container which protects the other elements against dust and humidity. The magnet has a cylindrical pole piece inside the coil and an annular pole piece surrounding the coil. The suspended coil represents an oscillatory system with a resonant frequency determined by the mass of the coil and stiffness of the spring suspension. The moving coil geophone operates according to the principle of a microphone or a loudspeaker: the coil consisting of copper wire wound on a thin non-conducting cylinder ("former") moves in the ring-shaped gap of a magnet (Figure 1.7). The annular magnet and polar pieces N and S in soft iron create a radial field in the gap. As the coil moves, its windings cut magnetic lines of force and an electromotive force is generated. The coil can only move in one direction, usually vertical, and only senses the component of ground motion along the coil axis as in Figure 1.8. The movement of the coil in the magnetic field generates a voltage across the terminals of the coil. The shunt resistance controls the amount of damping by controlling the amount of current flowing in the coil.

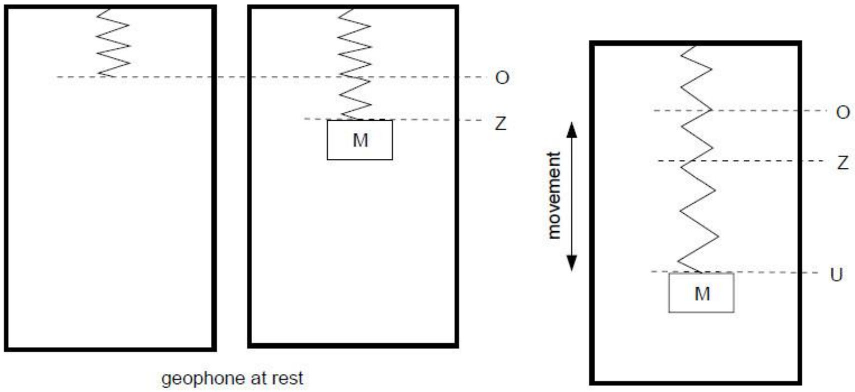

Figure 1. 8: Displacement parameters of a geophone, (left) rest position without weight, (centre) rest position with weight, and (right) in motion with weight, (Drijkoningen, 2003).

The geophone can be represented with a coil of mass M instead of a massive weight, (Figure 1.8). Vertical movements are measured along axis OZ, with the positive values in the downward direction and with an origin O at the level of the coil when the geophone is at rest. The geophone case is assumed to be connected tightly to the ground and follows exactly the ground motion. The movement of the coil lags behind that of the case and the voltage generated is a function of the relative motion, (Drijkoningen, 2003). When the case is at level z; the coil is at level u and its relative displacement y is:

$$y = u - z \qquad \text{……………………..…………………………………} \; 27$$

The forces acting in the coil are; its weight, Mg,

a) The force F_1 exerted by the spring which is proportional to the increase of the length of the spring with stiffness k.

$$F_1 = -ku = -k(y+z) = -(k_y + Mg) \qquad \text{…………………………………} \; 28$$

Where kz is the stretch under the weight of the coil i.e., Sz=Mg

b) The friction and other mechanical damping forces opposing the displacement of the coil relative to the case. The resultant is a force F_2 proportional to the velocity:

$$F_2 = -D\frac{dy}{dt} \qquad \text{……………………………………………………..…… } \; 29$$

Where D is the mechanical damping factor.

c) The electrical damping force F_3, is the back electromotive force that opposes the motion. It is proportional to the length L of the wire in the coil, to the magnetic induction B assumed to be constant, and to the current i flowing in the coil. Taking as positive the direction of the current generated when the relative displacement of the coil is negative, F_3 is expressed by:

$$F_3 = BLi \qquad \text{……………………………………………………..…….............} \; 30$$

The voltage generated in the coil is proportional to the rate at which the coil cuts the magnetic flux. As the field is assumed to be radial and perpendicular to the wire everywhere.

$$E = -BL\frac{dy}{dt} \qquad \text{………..………..............……………………………………} \; 31$$

The geophone can be thought of as a generator (a voltage source with electro-motive force *E*) feeding the amplifier through a connecting line. For our simplified evaluation, the inductance of the coil is assumed to be negligible and all impedances are assumed to be pure resistances. The total circuit resistance is R_T and the resistance of the amplifier input is R_A. The voltage flowing in the circuit is given by

$$E - R_T i = -BL \frac{dy}{dt} \qquad \ldots\ldots\ldots\ldots\ldots\ldots\ldots\ldots\ldots\ldots\ldots\ldots\ldots\ldots\ 32$$

And the voltage at the amplifier input, the seismic signal is;

$$V - R_A i = -\frac{R_A}{R_T} BL \frac{dy}{dt} \qquad \ldots\ldots\ldots\ldots\ldots\ldots\ldots\ldots\ldots\ldots\ldots\ldots\ldots\ 33$$

Equating the sum of the forces applied to the coil to the product of its mass and its acceleration, the equation of the movement of the coil is obtained.

$$Mg + F_1 + F_2 + F_3 = M \frac{d^2u}{dt^2} = M \frac{d^2(y+z)}{dt^2} \qquad \ldots\ldots\ldots\ldots\ldots\ldots\ldots\ldots\ 34$$

Replacing F_1, F_2 and F_3 by the values, the equation becomes.

$$-ky - D\frac{dy}{dt} + BLi = M \frac{d^2y}{dt^2} + M \frac{d^2z}{dt^2} \qquad \ldots\ldots\ldots\ldots\ldots\ldots\ldots\ldots\ldots\ 35$$

Differentiating this equation once and using the electrical relations, we get;

$$-k\frac{dy}{dt} - D\frac{d^2y}{dt^2} + BL\frac{di}{dt} = M \frac{d^3y}{dt^3} + M \frac{d^3z}{dt^3} \qquad \ldots\ldots\ldots\ldots\ldots\ldots\ldots\ldots\ldots\ 36$$

Rewriting equation (33)

$$\frac{dy}{dt} = -\frac{R_T}{R_A}\frac{1}{BL}V \qquad \ldots\ldots\ldots\ldots\ldots\ldots\ldots\ldots\ldots\ldots\ldots\ldots\ldots\ldots\ldots\ldots\ldots\ 37$$

Combining equations (36) and (37) we get,

$$M\,\frac{d^{2}V}{dt^{2}}+\left(D+\frac{B^{2}L^{2}}{R_{T}}\right)\frac{dV}{dt}+kV=M\,\frac{R_{A}}{R_{T}}\,BL\,\frac{d^{3}z}{dt^{3}} \qquad \ldots\ldots\ldots\ldots 38$$

which is a differential equation with constant coefficients of the conversion of the ground motion of the moving coil geophone to voltage, (Drijkoningen). The frequency of the moving coil geophone is given by;

$$f_{o}=\frac{1}{2\pi}\sqrt{\frac{k}{M}} \qquad \ldots\ldots\ldots\ldots 39$$

the natural frequency of the spring. This is the frequency at which a mass M suspended on a spring of stiffness k oscillates in the absence of any other constraint. The natural frequency can be decreased by increasing the mass or by reducing the stiffness of the spring.

From equation (38), the term in the brackets can be written as;

$$\frac{D}{M}+\frac{B^{2}L^{2}}{R_{T}M}=2\lambda\omega_{o} \qquad \ldots\ldots\ldots\ldots 40$$

where the first term is the damping term due to mechanical effects and the second term is the damping term due to electromagnetic effects. λ is the total damping of the geophone and ω_0 is the angular natural frequency of the wave. Introducing the constant a as;

$$a=\frac{R_{A}}{R_{T}}\,BL \qquad \ldots\ldots\ldots\ldots 41$$

The differential equation becomes

$$\frac{d^{2}V}{dt^{3}}+2\lambda\omega_{o}\,\frac{dV}{dt}+\omega_{o}^{2}V=a\,\frac{d^{3}z}{dt^{3}} \qquad \ldots\ldots\ldots\ldots 42$$

which is the conversion of ground motion to electric signal. From equation (42), a is the transduction constant, i.e., the conversion factor from particle velocity into voltage. λ is damping factor and ω_o is the angular frequency. This equation relates the voltage at the input of the recording system to the vertical displacement z of the geophone case (assumed to be perfectly coupled to the ground) in the time domain, (Li *et al.*, 2009).

The geophone response depends on three possible cases; when $\lambda>\omega_o$, $\lambda=\omega_o$ and when $\lambda<\omega_o$. If the right side of equation (42) is zero (i.e., the external force disappears), then the geophone instantaneous response can be obtained. The general solution of the inherent geophone vibration in terms of voltage when $\lambda > \omega_o$ is given by;

$$V = \exp(-\lambda t)\left\{ C_1 \exp\left[\lambda^2 - \omega_0^2\right]^{1/2} t + C_2 \exp\left[-\left(\lambda^2 - \omega_0^2\right)^{1/2} t\right]\right\} \quad \ldots\ldots 43$$

where C_1 and C_2 are constants.

The time duration of the geophone natural vibration depends on the damping coefficient λ. In this state, the geophone is said to be in an over-damped state and the motion is overdamped. When λ equals ω_o, the free motion of the geophone is between periodic and non-periodic vibrations. The inertial body stops vibration as soon as it returns to the balance position. This is a critically damped motion and the voltage is represented by the equation.

$$V = \exp(-\lambda t)(B_1 + B_2 t) \quad \ldots\ldots 44$$

where B_1 and B_2 are constants. When $\lambda<\omega_o$, the natural vibration is an attenuating sine vibration, which is an under-damped state and the motion is underdamped. The voltage output is;

$$V = \exp(-\lambda t)\left\{ D_1 \sin\left(\left[\lambda^2 - \omega_o^2\right]^{1/2} t\right) + D_2 \cos\left(\left[\lambda^2 - \omega_o^2\right]^{1/2} t\right)\right\} \quad \ldots\ldots 45$$

Equation (45) can be summarized as:

$$V = D\exp(-\lambda t)\cos(\omega t - \varphi) \quad \ldots\ldots 46$$

where $D=\sqrt{D_1^2+D_2^2}$ is the amplitude of the wave.

When the vibrations arrive from the source, the active element in the geophone oscillates and a force is in turn introduced. The force produced is proportional to the vertical displacement *z* and is given by $z = A\cos pt$ with p as the frequency of the incoming seismic wave and *A*, its amplitude.

Equation (42) can then be written as;

$$\frac{d^2V}{dt^2}+2\lambda\omega_o\frac{dV}{dt}+\omega_o^2V=Aap^3\sin(pt) \quad \ldots\ldots\ldots\ldots\ldots\ldots\ldots\ldots\ldots\ldots\ldots\ldots\ldots\ldots\ldots\ 47$$

The solution to the equation (47) is:

$$V=\frac{aAp^3}{\left\{\left(\omega_o^2+p^3\right)^2+4\lambda^2\omega_o^2p^3\right\}^{1/2}}\sin(pt-\theta) \quad \ldots\ldots\ldots\ldots\ldots\ldots\ldots\ldots\ldots\ldots\ldots\ldots\ldots\ 48$$

where *θ* is the phase difference between seismic wave and natural frequency of the geophone.

$$\tan\theta=\frac{2\omega_o\lambda p}{\omega_o^2-p^3} \quad \ldots\ldots\ldots\ldots\ldots\ldots\ldots\ldots\ldots\ldots\ldots\ldots\ldots\ldots\ldots\ldots\ldots\ldots\ldots\ldots\ldots\ 49$$

At resonance, $\omega_o = p$, very large displacement occurs in the geophone and probably distort the geophone. The damping term λ is introduced to prevent this distortion, and as a result, the geophone works between the two extreme points, that is when $\omega_o < p$ where the geophone reads the displacement and when $\omega_o > p$, where the geophone measures acceleration.

1.8 Refraction Statics

Refraction methods allow us to derive estimates of the thicknesses and velocities of the near-surface layers by analyzing the first-breaks of the seismic records as seen in Chapter 1. According to the Huygens' principle, that is, every point on an advancing wavefront can be regarded as the source of a secondary wave and that a later wavefront is the envelope tangent to all the secondary waves. The important concept in seismic refraction is that when a seismic ray crosses a boundary between two formations of different velocities, then the ray is bent according to Snell's law which defines that the sine of refracted angle is equal to the ratio of the velocities of the two formations.

Therefore, the static correction based on refraction survey acquires the information of the first-arrival time of wavefield from refractor and the refractor velocity. Hence, there are two basic conditions for refraction survey, that is, a relative stable refraction interface between the two formations and an acknowledged near-surface velocity distribution. Applying the static corrections based on refraction survey can ensure structural integrity in the processed section. Refraction statics are effective for correcting long spatial wavelength anomalies and compensating for the weathering layers. Actually, refraction statics are also effective against short spatial wave- length anomalies, (Zhu *et al.*, 2014).

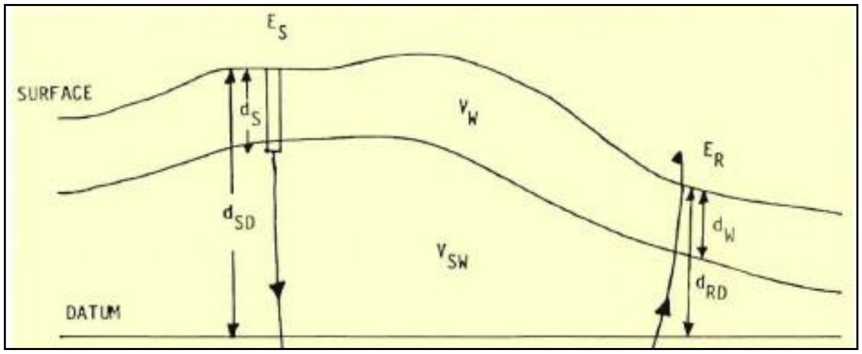

Figure 1. 9: Near surface representation of the computation of the static correction, (Yilmaz, 2000)

Consider a simple case of a two layer near-surface (Figure 1.9) consisting of a weathered layer of low velocity unconsolidated material and a sub-weathered layer of more competent lithology. Assuming that the datum plane down to which we wish to correct the data is in the sub-weathered layer and if we know the thickness of the weathered layer, the elevations of the shot and geophone, and the depth of shot, the static corrections of station can be computed. There are two components to the total static: a shot component for shot station and a receiver component for the receiver station. For shot component, the shot static correction for a particular station is given by;

$$t_S = \frac{d_{SD} - d_S}{V_{SW}} \quad \text{...} \; 50$$

while for receiver component, the receiver static correction for each station is, (Yilmaz, 2000);

$$t_R = \frac{d_W}{V_W} + \frac{d_{RD} - d_W}{V_{SW}} \quad \text{...} \; 51$$

Where t_S =shot static correction, t_R = Receiver static correction, D_W = depth of weathering, D = Datum level, E_S = shot elevation, E_R = Receiver Station, d_{SD} = Thickness of shot to datum, d_{RD} = thickness from the receiver to datum, V_W = Velocity of weathered zone and $V_{SW} =$ Velocity of sub-weathered zone. The refraction statics for this station is the sum of values obtained in equations 50 and 51.

$$T = t_S + t_R \quad \text{...} \; 52$$

CHAPTER TWO

MATERIALS AND METHODS

2.1 Field Work and Data Acquisition

Seismic surveys are mainly carried out to accurately record ground motion caused by an energy source at a known location. The record of ground motion constitutes seismogram and is the basic information used for interpretation through modeling and imaging of the subsurface. The seismogram is recorded as a function of time and receiver distance from the source. The velocities can then be estimated from the graph by determining the travel times of the waves to the receivers. This helps in determining the velocity and thicknesses of the subsurface strata. Low velocity layer (LVL) spread length was 108 m with 24 channel receivers to record the seismic waves. A pre-calibrated rope of 108 m was used to mark geophone location at each station along the line and geophones planted within the calibrated points besides the rope. A wiring cable was connected to all the geophones and to DAQLink III to receive seismic signals from geophones. The received analogue seismic signals were converted to digital seismic signals using DAQLink III and then transferred to the Laptop for identification of good/bad seismic signal. Geophones coupled firmly to the ground showed green colour in the display window of the computer while loose geophones to the ground showed yellow colour (Figure 2.1). These were first rectified before data was collected. The offset distance from the first geophone was 20 cm.

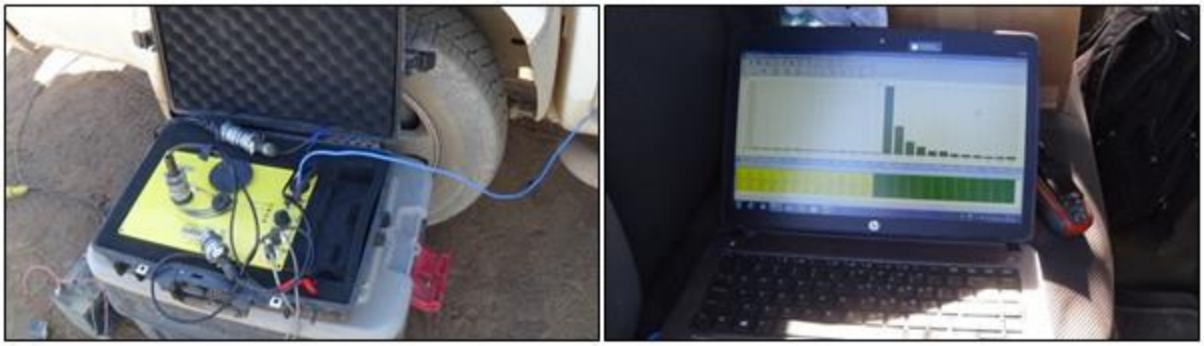

Figure 2. 1: DAQLink III and Laptop for data collection

The layout configuration of the spread 108 m was 1m-2m-2m-3m-3m-5m-5m-6m-6m-8m-8m-10m-8m-8m-6m-6m-5m-5m-3m-3m-2m-2m-1m which resembled calibration on the rope and positions at which geophones were planted to the ground. The source of the seismic signal was a sledge hammer and steel alloy plate as seen from Figure 2.2. The steel alloy plate was fitted with a trigger to set up the geophones so as to receive the seismic signal from the source. The set up was then tested for data collection before data acquisition began. Once the set up was complete, data collection began and was recorded in SEG Y format, a trace sequential (or de-multiplexed) internationally recognized format designed to store seismic data. A stack of 10-15 shots was made for forward and reverse shooting at each station to minimize background noise effects (Figure 2.4). Quality control was done by examining the nature of seismic data produced when recording to eliminate noise and to ensure good records of data are collected and noisy signals rejected. The sampling rate of the data was 125 µs with recording length of 500 ms. Other measuring considerations are shown Table 2.1.

Figure 2. 2: Steel alloy plate fitted with a trigger and a sledge hammer (left), geophones placed firmly in the ground a long a line, also seen is a rope calibrated with a red tape; the position at which the geophone is placed, (right).

Table 2. 1: LVL recording parameters used in this study

Recording System	DAQLink III
Recording format	SEG-Y
Recording Length	300 ms
Sample rate	125 us
Delay Time	0 ms
Gain	Fixed
Low cut filter	Out
High cut filter	Out
Notch	Out
Offset	0.2 m
Source	Sledge Hammer + Plate
Receiver	24 Channels Geophone
Total Spread Length	108 m
Spread Configuration	1m-2m-2m-3m-3m-5m-5m-6m-6m-8m-8m-10m-8m-8m-6m-6m-5m-5m-3m-3m-2m-2m-1m

Station locations were determined using a hand-held Global Positioning system (GPS). The collected data was then stored in the SEGY format in the computer for further processing to determine the velocity and thickness of the weathered zone. The data was acquired after every 3 km along each line using one component 10 Hz geophones. Data was acquired in 8 profile lines as shown in Figure 2.3 with a total of 94 stations.

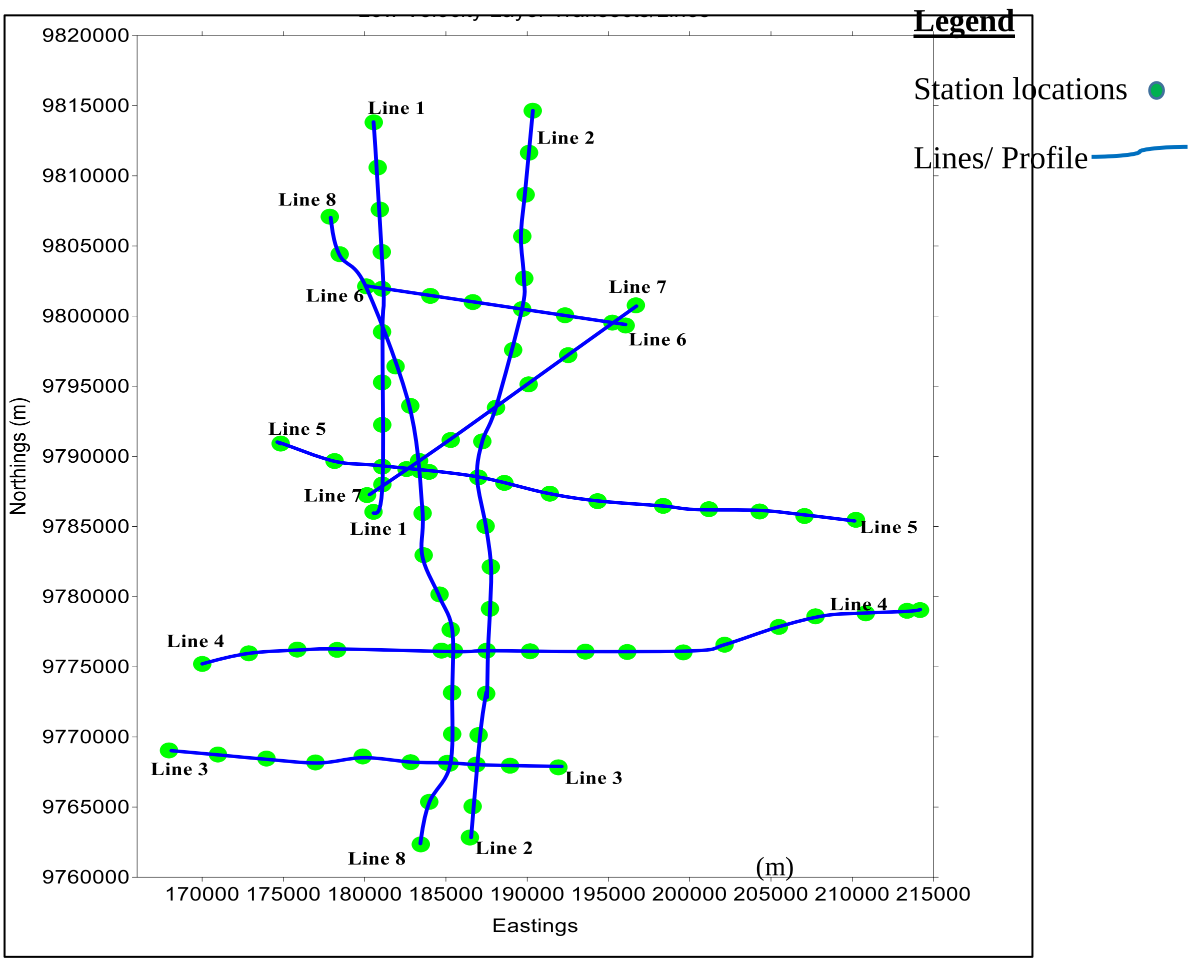

Figure 2. 3: Low Velocity Layer location map and the profiles covered

CHAPTER THREE

DATA ANALYSIS, RESULTS AND DISCUSSION

3.1 Data Analysis.

Refraction method is widely used in determining the thicknesses and velocities for near-surface layers. It requires an accurate picking of the first arrival times of the seismic waves. The acquired data was first uploaded directly in to the computer and imported into the Vista 2D/3D Software for processing. The imported data at each station in each line was sorted, scaled and stacked in to a single short as in Figure 3.1. Stacking of 10-15 shots into a single shot was done to improve their resolution and to increase signal to noise ratio so that the signals are seen more clearly.

Offset (m)	FBT (ms) Left	FBT (ms) Right
0	1.189	1.189
1	4.741	3.697
3	10.347	9.182
5	15.953	14.666
8	21.559	20.150
11	27.165	25.634
16	32.508	32.536
21	40.127	40.374
27	47.746	48.212
33	55.365	56.938
41	62.984	65.164
49	71.449	73.391
59	76.935	81.709
67	82.420	87.872
75	87.906	94.034
81	93.392	100.196
87	98.877	102.457
92	102.854	104.637
97	105.952	107.015
100	108.333	108.323
103	110.119	109.631
105	111.310	110.939
107	113.159	112.247
108	114.286	113.555

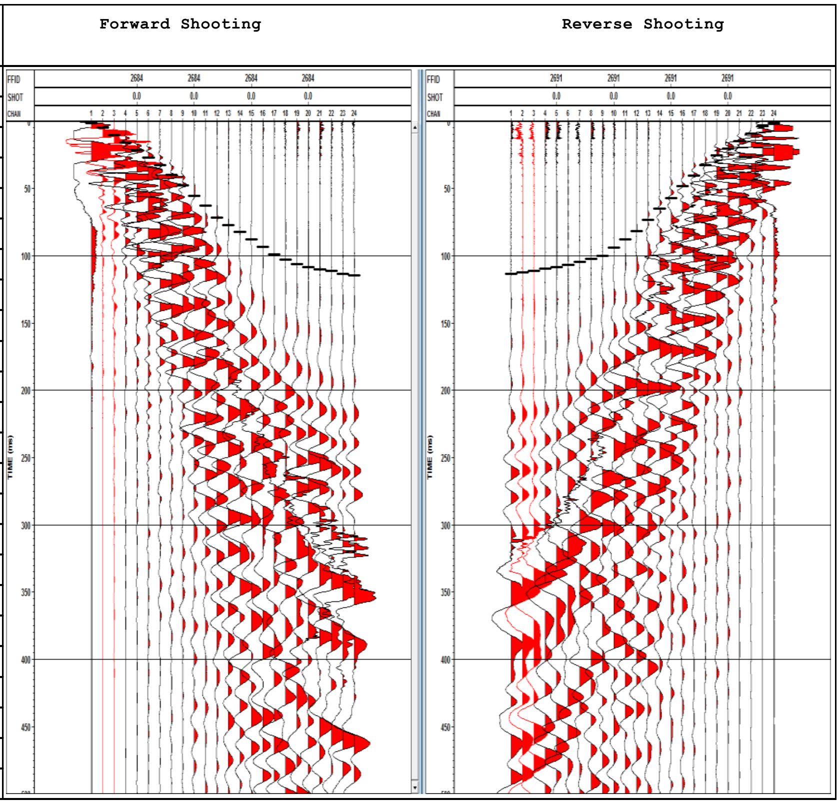

Figure 3. 1: Datum Line 8 station 17 showing first break picks for forward and reverse shooting respectively.

3.1.1 Determination of Velocities and Depths of Layers

Line 8 station 17 is used to show how data analysis, velocity and depth computation done at each LVL location in Magadi basin was calculated. The first break picking for forward and reverse shooting was done (Figure 3.1) for the digitized seismic waveforms from all channels for each station along all the surveyed eight profiles (Figure 2.3). Picked first break times for forward and reverse shots (Figure 3.1) were exported to spreadsheet for plotting travel time graph of the seismic wave at each station (Figure 3.2) and used to calculate velocity and thickness of different layers at each station as explained below.

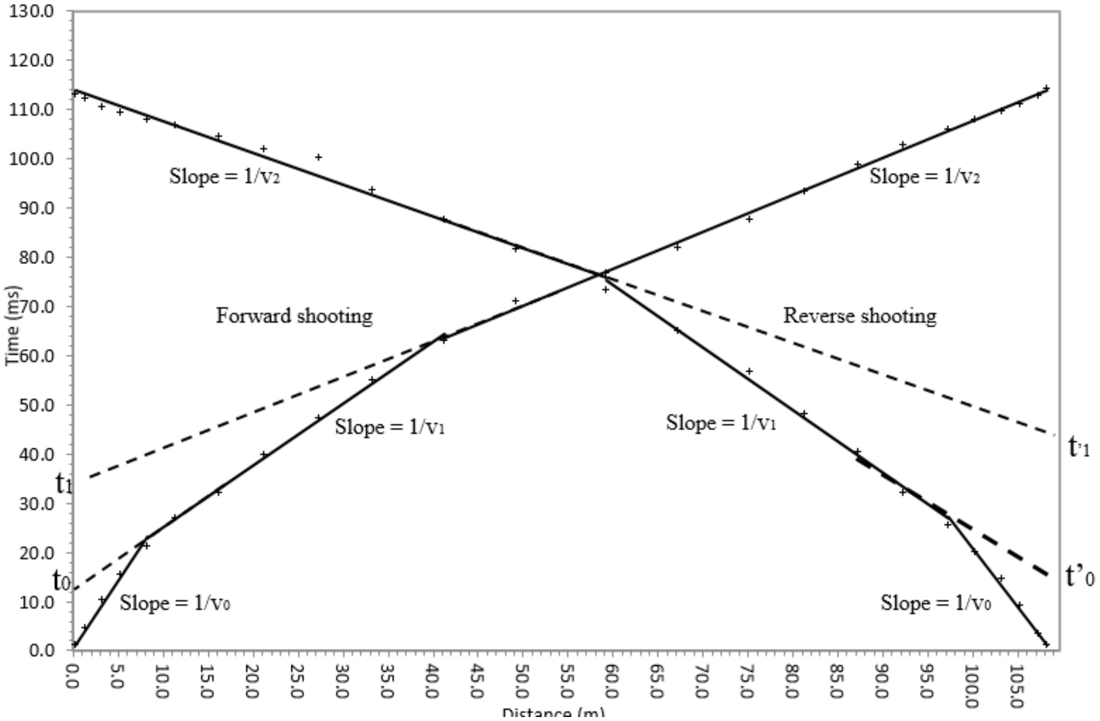

Figure 3. 2: LVL data line 8 station 17 showing time-graph for forward and reverse shooting.

Using the assumptions made in section 1.7.4 and applying equation 11, the velocity of the first layer was obtained by getting the reciprocal of the slope of the first layer in Figure 3.2. In this case, the velocity for the first layer is 354.8 m/s. Similarly, the reciprocal of the second and the third layers gives the forward velocities of the second and third layer as 792.1 m/s and 1328.3 m/s respectively. Intercept time equations 22 and 23 were used to determine the thickness of layer 1 and 2 respectively. The thickness of the weathered/first layer was found to be 2.5 m and the thickness of semi-weathered/second layer was found to be 16.1 m, giving a total depth to the bedrock 18.6 m for forward shooting. This process was repeated for the reverse profile shooting and velocities of 411.3 m/s, 787.9 m/s and 1549.5 m/s were obtained for weathered, semi-weathered and bedrock/third layer respectively with thicknesses of 3.1 m and 20.2 m. A total depth 23.3 m was obtained for reverse profile shooting. Assuming the layers are horizontal and there is no dipping, a quick approximation of the true velocity of the first layer is the average velocity of the forward and reverse shots in the first layer (equation 21). This velocity is (354.8+411.3)/2 = 383.1 m/s. This was also done for subsequent 2 layers and the results tabulated in Table 3.1

Table 3. 1: LVL analysis and interpretation of Station 17 line 8.

	Velocity, V (m/s)		
	V_0	**V_1**	**V_2**
Forward Shooting	354.8	792.1	1328.3
Reverse Shooting	411.3	787.9	1549.5
Average Velocity	383.1	790.0	1438.9
	Thickness, Z (m)		
Thickness	**Z_0**	**Z_1**	**$Z = (Z_1+Z_0)$**
Forward shooting	2.5	16.1	22.9
Reverse Shooting	3.1	20.2	23.3
Average Thickness	2.8	18.2	21.0

Considering the assumptions made in section 1.7.4 and that the layers in Magadi basin are dipping, using equation (17) for reversed set of profiles, where α and β consists the dipping term γ, we can obtain the angles α and β as follows;

The angle $\alpha = \text{Sin}^{-1} (V_0/V_{1f}) = (383.3/792.1) = 28.94^0$ and $\beta = \text{Sin}^{-1} (V_0/V_{1r}) = (383.3/787.9) = 29.11^0$ where f and r in the equations denote forward and reverse profile shooting respectively. The dip angle from equation (18) for this station becomes $\gamma = (\alpha - \beta)/2 = 0.08^0 \approx 0.1^0$.

Applying equation (19) for a small dip angle, $\gamma < 15$, the true velocity V_1 of the second layer is $V_1 = \{½ ((1/792.1) + (1/787.9))\}^{-1} = 790.0$ m/s and $V_2 = \{½ ((1/1328.3) + (1/1549.5))\}^{-1} = 1430{\cdot}4$ m/s for the third layer. The result of V_1 compare well and agrees with average results obtained and shown in Table 2 based on equation (21). V_2 is slightly less than the average results by 0.5%. This was done for each station at 3 km interval in all the profiles in Figure 2.3.

Equation 19 and 21 were used to calculate true thickness/ velocity and the average thickness/ velocity respectively for each station in line 1 and the results compared in Table 3.2 and Table 3.3

Table 3. 2: α, β and the dip angle γ in degrees calculated for line 1 to show that angle of dip is <15 degrees and layers could be treated as horizontal. All angles are in degrees

Station No.	**α**	**B**	**γ dip angle, (α-β)/2**	**V_0 (m/s)**	**True V_1 (m/s)**	**V1 (m/s) (average)**	**% difference V_2**	**True V_2 (m/s)**	**V_2 (m/s) (Average)**	**% difference V_2**
1	13.86	7.73	3.1	271.5	1452.0	1576.3	8.6	3184.2	3184.3	0.003
2	6.72	6.61	0.1	248.0	2135.9	2136.1	0.0	3604.0	3604.1	0.001
3	23.96	13.54	5.2	288.8	902.2	972.5	7.8	2837.4	2837.4	0.001
4	7.37	5.92	0.7	280.4	2421.7	2450.6	1.2	4507.6	4516.4	0.194
5	14.99	15.20	0.1	283.9	1090.2	1090.3	0.0	4348.7	4355.9	0.166
6	29.85	26.41	1.7	391.1	829.8	832.4	0.3	1394.2	1408.8	1.047
7	21.13	23.68	1.3	255.6	670.9	672.9	0.3	1276.8	1278.3	0.120
8	20.24	26.25	3.0	216.8	550.0	558.4	1.5	1291.2	1291.2	0.001
9	34.74	26.36	4.2	238.5	470.4	477.8	1.6	1644.0	1650.7	0.406
10	27.15	25.25	1.0	209.8	475.4	475.9	0.1	1519.8	1520.4	0.039
11	21.25	23.95	1.3	187.5	488.0	489.6	0.3	1659.8	1682.4	1.362

Table 3. 3: Average thickness and true thickness for line 1 compared

Thickness			
Station No.	**Average Thickness (H_0) (m)**	**True Thickness (H_0) (m) Using dip angle γ**	**% difference in Thickness**
1	1.143	1.156	1.083
2	1.316	1.333	1.263
3	1.497	1.539	2.773
4	1.402	1.404	0.089
5	1.062	1.069	0.656
6	2.711	2.679	1.199
7	1.627	1.629	0.101
8	3.102	3.089	0.412
9	3.860	3.911	1.296
10	3.208	3.209	0.042
11	2.790	2.804	0.494

Having determined that the angle of dip are very small (less than 15) from Table 3.2 and other 8 profiles, and that the percentage difference between the average velocity/true velocity and average thickness/true thickness are small and that the values are very close (see Table 3.2 and Table 3.3), the layers at each station in Magadi basin were treated as horizontal and equations (22 and 23) governing ray path in a horizontal layers were used. The time intercepts T_i for most stations were not equal (Figure 3.2) and hence the thickness for forward and reverse profile was calculated separately and equation (21) used to determine the average velocity of each layer at each station. Finally, Pap (1976) found that at small dips (Equation 19) approaches arithmetic mean (Equation 21) and, in approximately 90% of the cases, the averaging of updip and downdip velocities yields satisfactory results (Table 3.2 and Table 3.3). Therefore, the average of forward and reverse shooting velocities were used to calculate the true velocities and thickness of each layer at each station in all the eight profile in Figure 2.3. The results obtained in reverse and forward shooting were used to create a 2D model to show the variation of first and the second layer in the weathered zone as shown Figure 3.3 for station 6 line 1.

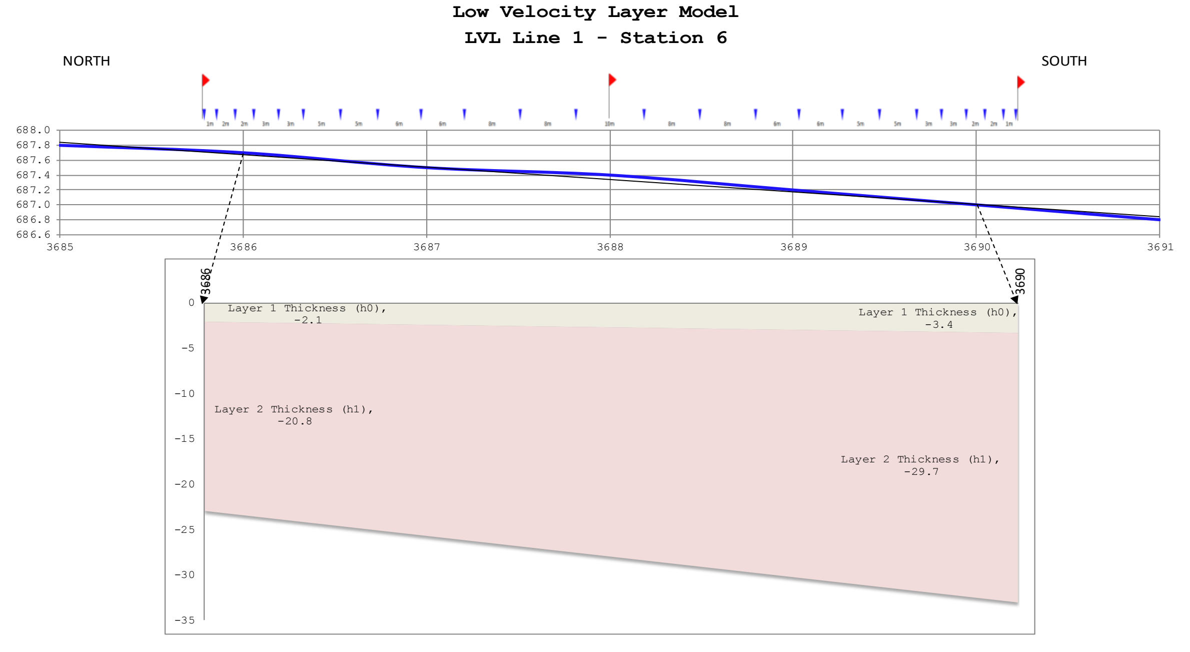

Figure 3. 3: Low velocity layer model for line 1 station 6

The top graph shows the variation of topography for various stations with current station recorded at the middle. For this specific station, the elevation decreases towards the South, since line 1 is oriented in a North South direction (Figure 2.3). The depth of both the weathered and the semi-weathered layer increases towards the south as observed in Figure 2.6. Therefore, for this given station, the low velocity zone increases towards the south. This was done for all the stations along line 1 and extended to the remaining seven profiles in order to observe the general trend of LVL and velocity along each profile.

Variation of velocities along the profile 1-8 and their corresponding 2D surface variation of the thickness in the low velocity zone is first discussed. Lines 1, 2 and 8 are trending in the N-S direction (Figure 2.3). Line 7 was recorded in the NE-SW direction. The rest of the lines are in West-East directions. H_0 and H_1 refers to thickness of layer 1 and layer 2 respectively.

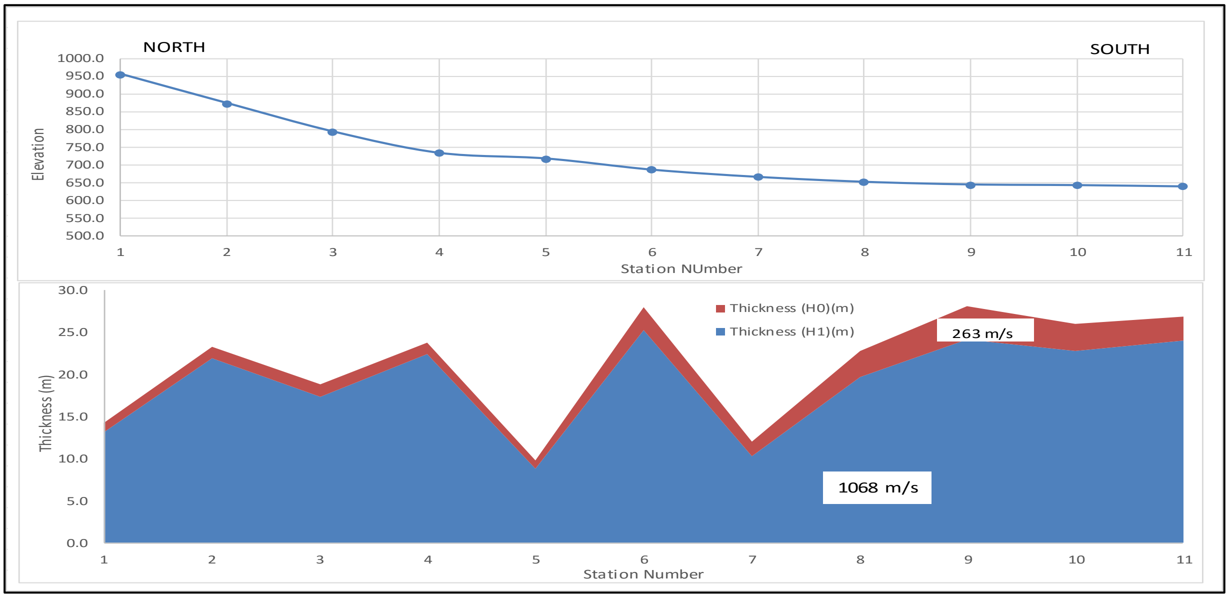

Figure 3. 4: Low velocity Layer variation along line 1

Line 1 (Figure 3.4) shows the general variation and trend of LVL in Magadi basin. The elevation decreases gently along the profile towards the south. Highest elevation are seen in the north and least one in the South. The LVL trends in the N-S direction with maximum thickness in the Southern part. This LVL is quite intermittent. The first layer is quite thin (H_0), however, it is most abundant towards south. A similar trend is observed in layer 2 (H_1). The LVL of line 1 (Figure 3.4) has an average velocity of 263 m/s and 1068 m/s with average thicknesses of 2.2 m and 21.3 m for layer 1 and layer 2 respectively. H_0 is thick between stations 1 and 4, decreases at station 5 and increases sharply to station 6 before decreasing to station 7 and finally increases gently towards the end. Station 6 and 9 have the minimum depths. Layer 2 is thicker than layer 1 with maximum thickness observed at station 11. The velocity in the first layer (V_0) of this line is generally constant (Figure 3.5) with most velocity values being less than 500 m/s. The velocity changes slightly in the second layer (V_1) towards the northern parts and decreases uniformly to constant in the southern part. The maximum velocity variation is observed at station 4.

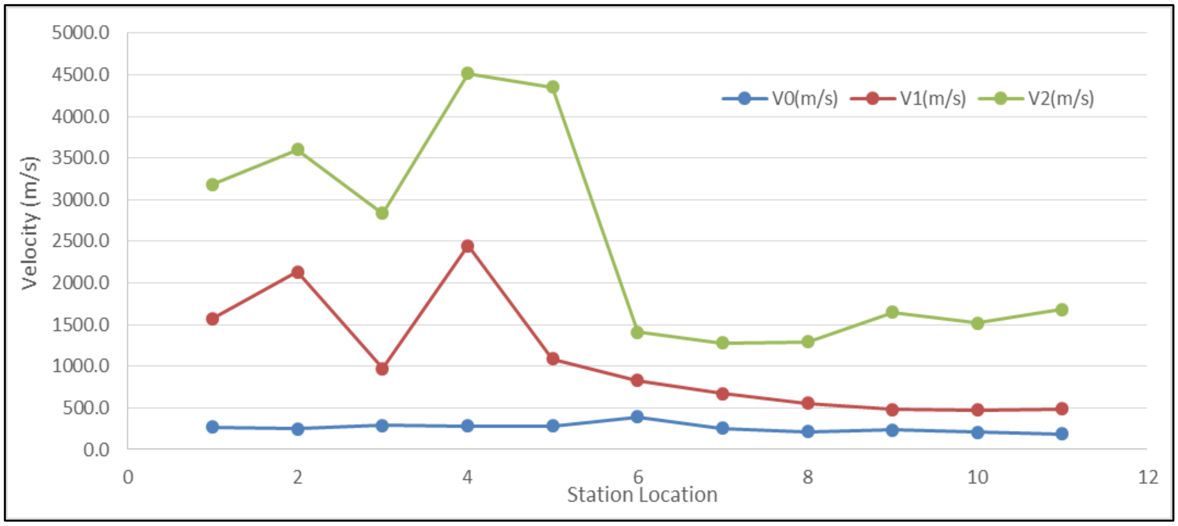

Figure 3. 5: Velocity variation along line 1 (N-S)

The third layer has the largest average velocities (V_2) along the profile with much variation being in the Northern part of the profile. The velocity decreases across the profile tending to a constant in the southern part of the profile. These high velocities could be in the consolidated zone or bedrock in the Magadi basin. V_1 and V_2 have similar trends with both decreasing towards the south.

In Line 2 (Figure 3.6), a very thin layer 1 is observed across the profile while layer 2 is slightly thicker. The thickness increases along the line with much LVL observed at centre of the line. High elevated areas have low thickness while gentle areas are thicker (centre of line 2). The average thicknesses of layer 1 and layer 2 are 3 m and 26.4 m, respectively with maximum average depth being 29.4 m. Maximum depths are observed from stations 9-13 with lowest depths seen at stations 8 and 15. The large thicknesses (stations 9-13 of Figure 3.6) observed are within the basin where erosion of trachytes by wind and water are deposited in the lowland regions resulting in increased depth of LVL. Velocities of layer 1 line 2 (V_0) (Figure 3.7) are similar to line 1 layer 1 since both are below or equal to 500 m/s. Layer's 1 and 2 have average velocities of 335.7 m/s and 1323.8 m/s (Figure 3.6). Layer 1 has fairly constant velocity (V_0) across the line which is less than 400 m/s. The average velocity of Layer 2 (V_1) decreases towards station 4 and is generally constant before picking up at station 8. The highest velocity is observed at station 10 and then decreases slowly towards the end of the line. Velocity of layer 3 (V_2) (Figure 3.7) decreases sharply along the line up to station 4, increases to station 8 and finally decreases along the line. The velocity is high in this layer. The layer is probably in the bedrock zone.

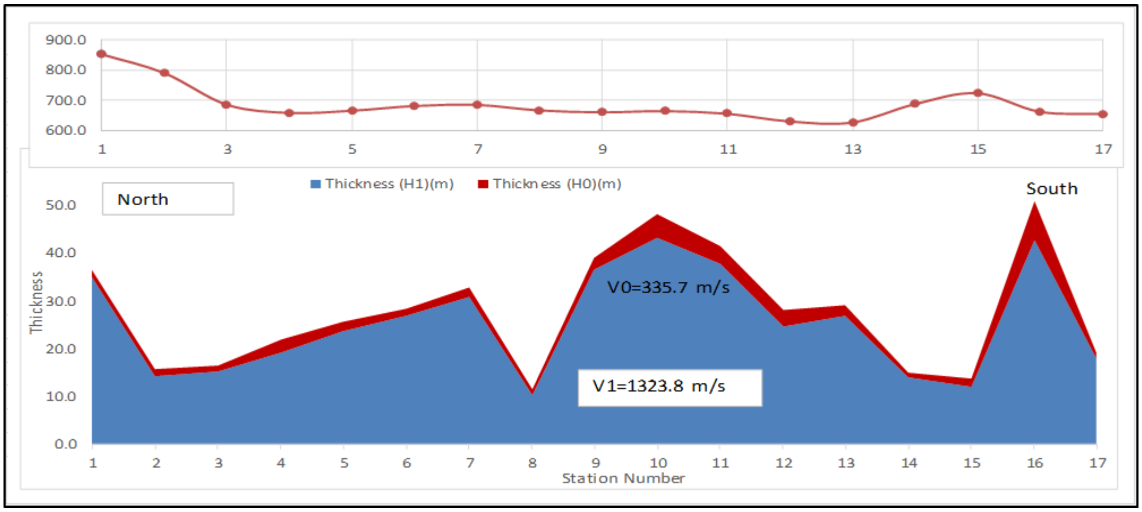

Figure 3. 6: 2D Low velocity layer variation along line 2 (N-S)

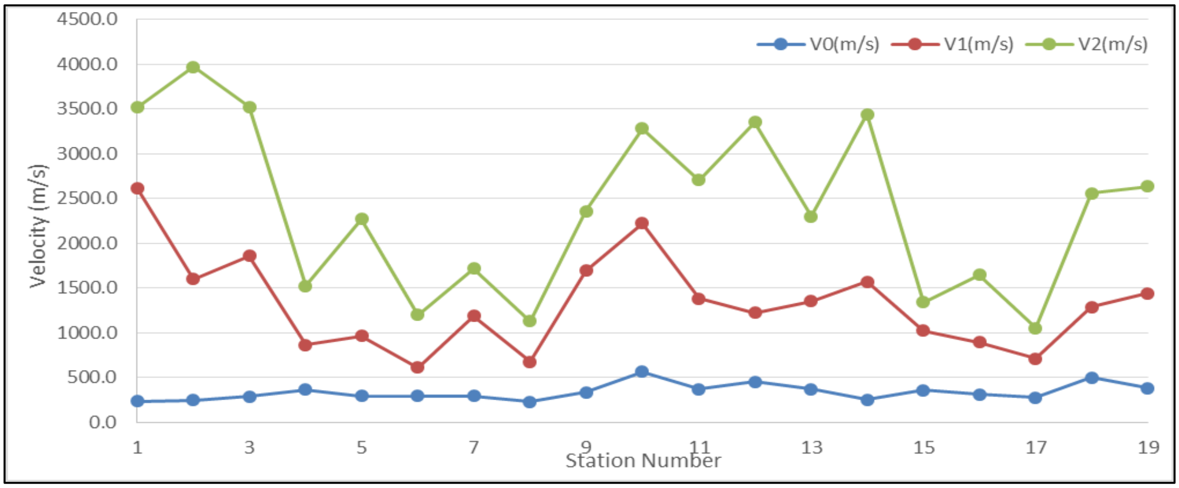

Figure 3. 7: Velocity variation along line 2 (N-S)

Line 8 is the last line trending in N-S direction. It has very thin first layer as observed in Figure 2.11. Second layer is thicker with depth increasing towards the centre of the profile. The end points of the profile has low thickness so is the elevation. The average thickness of layer 1 is 2.4 m and 22.1 m for layer 2. Layer 1 thickness is generally constant along line 8. Maximum thickness of LVL is observed between stations 6-13 while station 5 has the lowest depth. It has average velocities of 217.7 m/s and 878 m/s for layer 1 and layer 2 respectively which are well within a weathering zone, (Figure 3.8). Velocity of the first layer (V_0) and second layer (V_1) of line 8 (Figure 3.9) is relatively constant and below 2000 m/s. Both velocities decrease along the profile. Velocity of layer 3 is quite high in the north, however, it decreases in the southern side. Velocity spikes are seen at stations 6, 14 and 16 along the profile. However, when two velocity values sandwiching between this spiked velocities are averaged, the trend in layer 3 resembles layer 1 and 2.

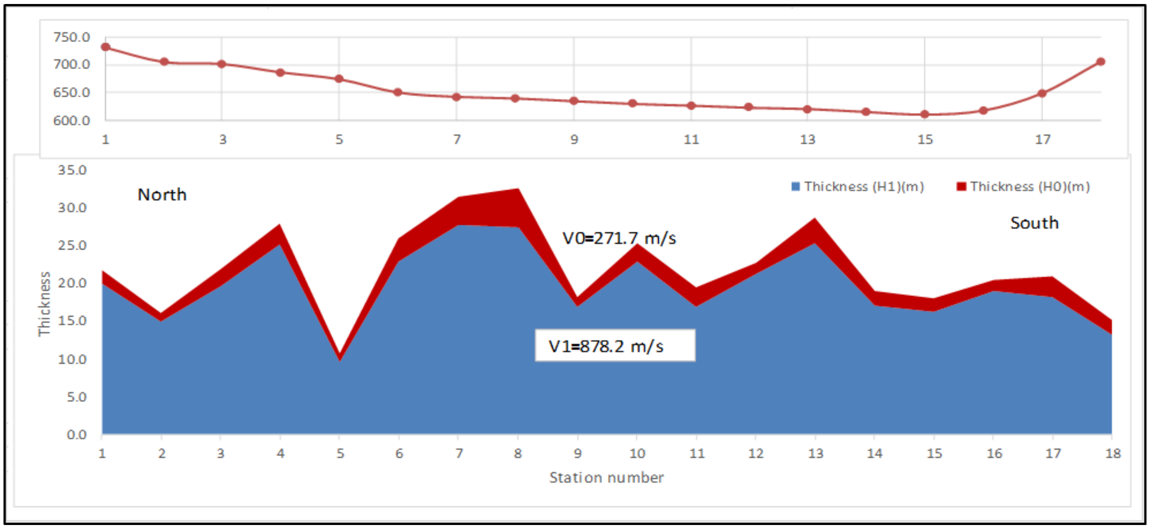

Figure 3. 8: Low velocity layer variation along line 8 (N-S)

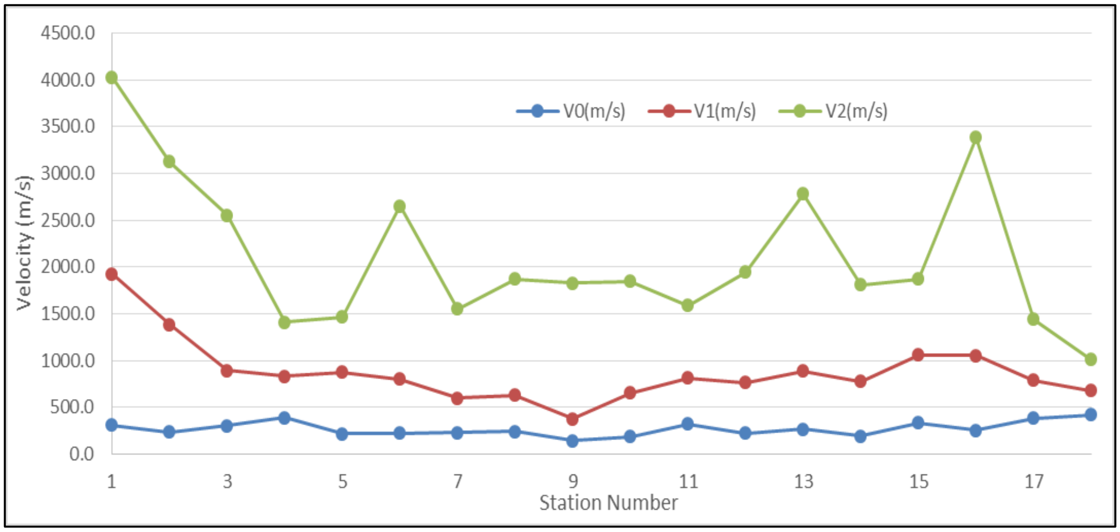

Figure 3. 9: Velocity variation along line 8 (N-S)

Line 7 traverses from NE-SW direction at the North of Lake Magadi (Figure 2.3). This profile has relatively flat elevation except at station 4 (Figure 3.10). The first layer is very thin and is observed to increase towards south west. Layer 2 is generally thicker and spreads on both sides of station 4. The LVL layer is fairly constant except at station 4 where it has the least thickness. The least thickness at station 4 could be attributed to erosion of the weathering zone due to surface run off and wind erosion towards Lake Magadi and low altitude areas. Layer 2 is generally constant. Layer 1 and layer 2 have average velocities of 274.8 m/s and 933.6 m/s with thicknesses of 2.5 m and 23.7 m, respectively.

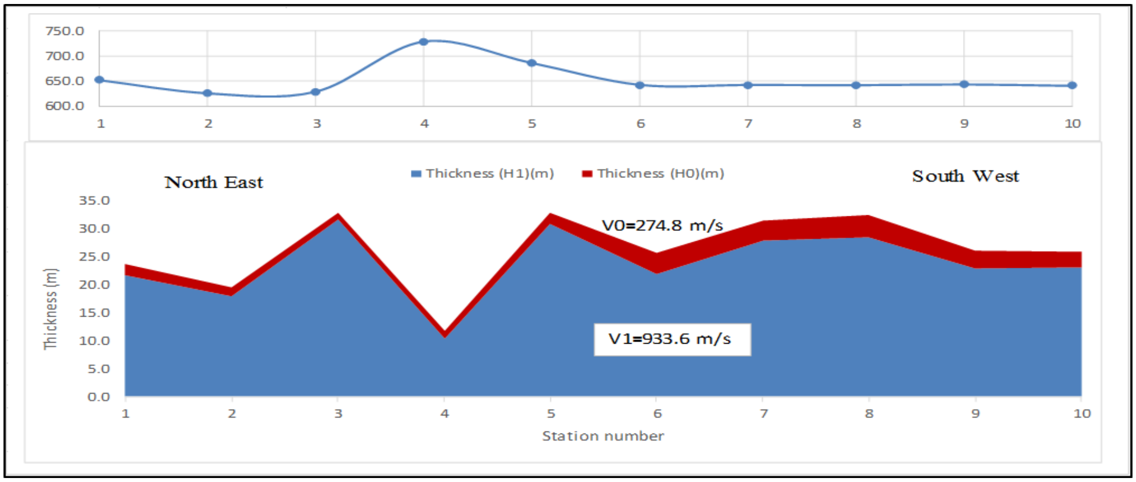

Figure 3. 10: Low velocity layer variation along line 7 (NE-SW)

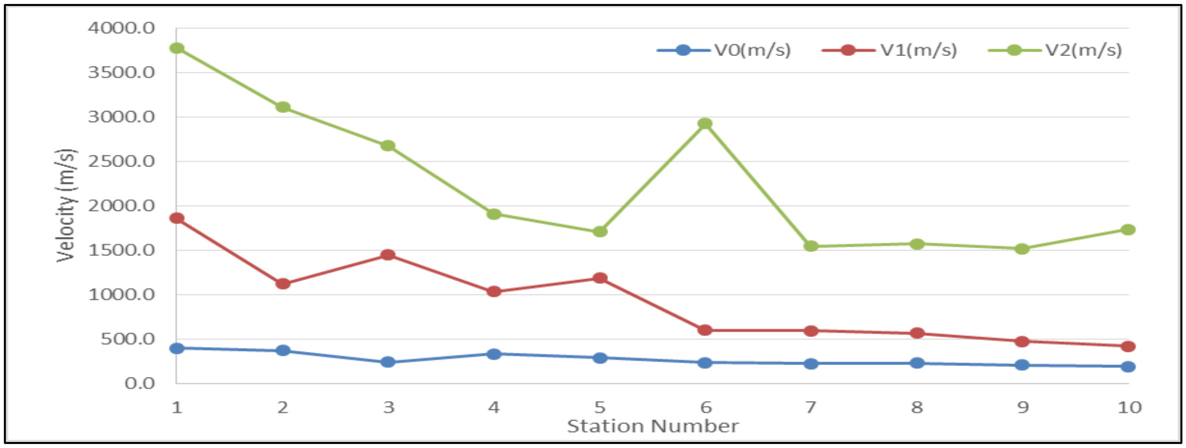

Figure 3. 11: Velocity variation along line 7 (NE-SW)

Velocities V_0, V_1 and V_2 of layers 1, 2 and 3 of line 7 (Figure 3.11) decreases generally along the profile with large variations experienced in the NE direction. Layer 1 and layer 2 have very low velocities of less than 2000 m/s.

Lines 3, 4 and 5 are oriented in East –West direction and their elevations decreases towards the west as shown in Figures 3.12, 3.14 and 3.16. Line 3 is at the extreme south (Figure 2.3) and cuts through swampy regions of Shompole (Figure 1.1). Lines 5 goes through Lake Magadi.

The LVL of line 3 decreases towards East (Figure 3.12). This line has the least LVL with layer 1 and layer 2 having average thickness of 1.6 m and 16 m with velocities of 328.7 m/s and 956.8 m/s. The LVZ decreases gently westwards which is similar to elevation. Station 1 has the maximum thickness along the profile while stations 7 and 9 have the least depth. The LVL is thicker in the East and thinner in the West.

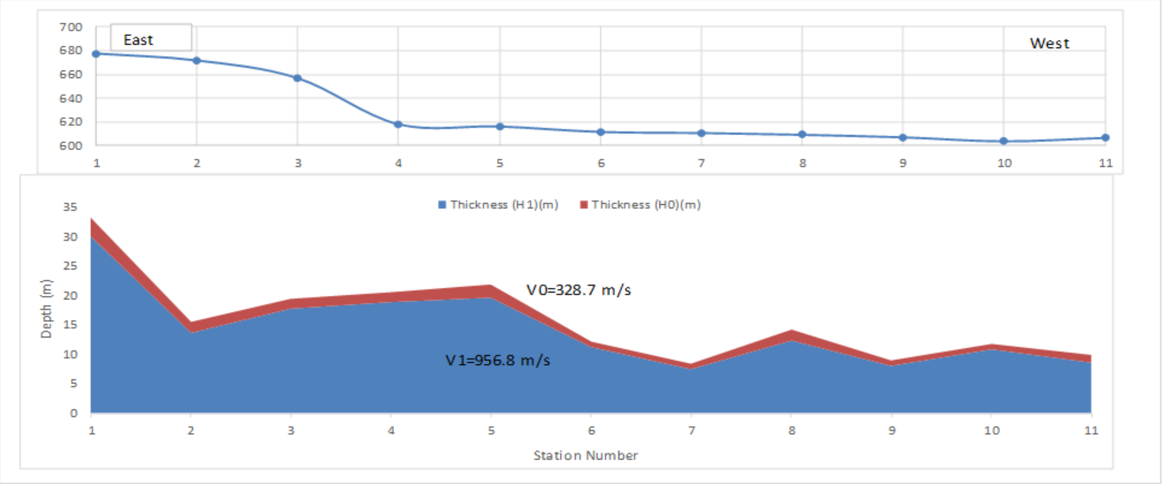

Figure 3. 12: Low velocity layer variation along line 3 (E-W)

Velocities V_0 and V_1 for layer 1 and layer 2 of profile 3 are generally constant in the western side of line 3, (Figure 3.13). Layer 1 and 2 velocities' spikes at stations 3 and 8 respectively which is also observed in the velocity of layer 3. V_3 is generally high and intermittent along the line while V_0 is fairly constant throughout the line.

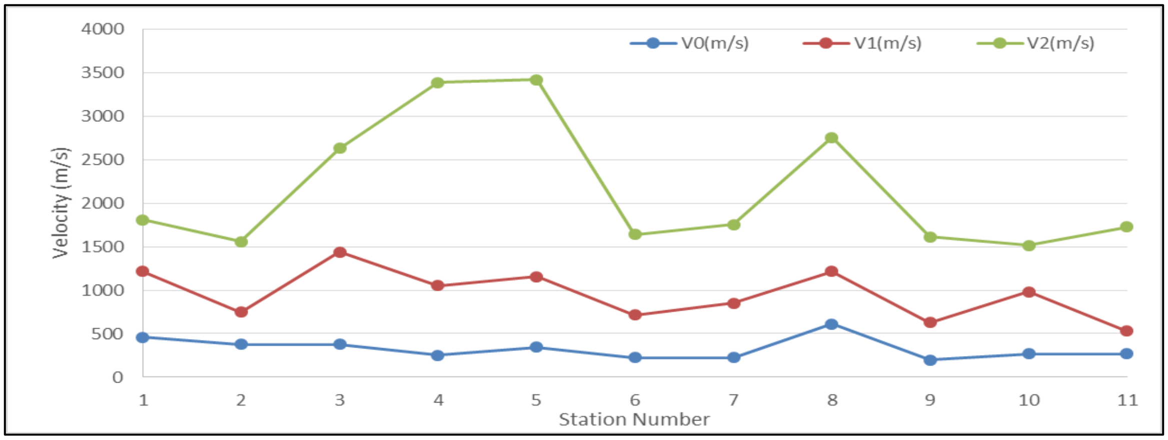

Figure 3. 13: Velocity Variation along line 3 (E-W)

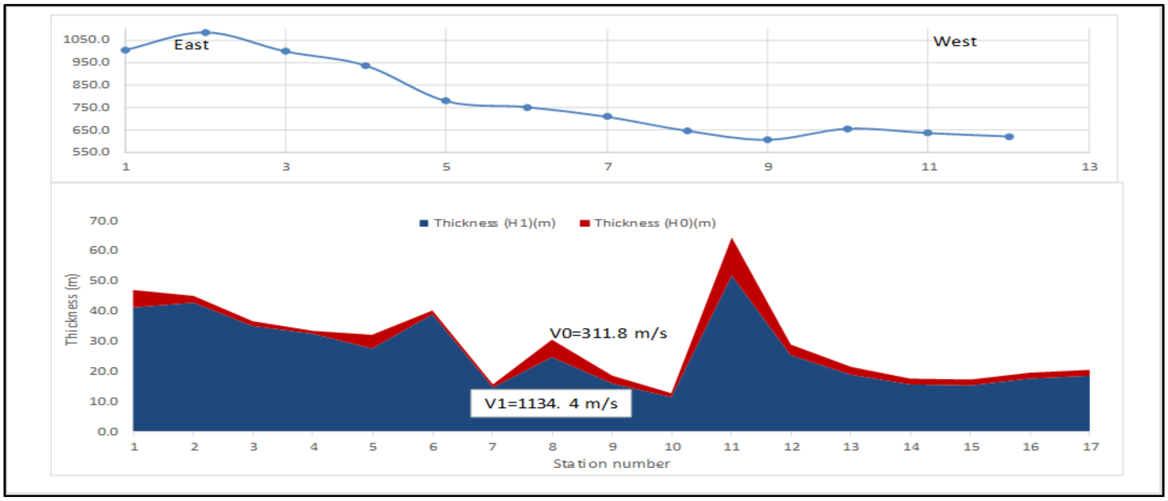

Figure 3. 14: Low velocity layer variation along line 4 (E-W)

The elevation of line 4 generally decreases towards the West (Figure 3.14). Low velocity layer is very thin in this profile. Layer 2 is thicker than in most lines and layer 1 is barely invisible. The consolidated zone is very close to the surface. The thickness of LVL of line 4 (Figure 3.14) decreases towards the west with higher thickness observed between stations 1-6 and 11, while stations 7, 10 and 14 have the least thickness. Layers 1 and 2 have an average velocity of 311.8 m/s and 1134.4 m/s, respectively. Figure 3.14 shows average velocity of 35-40 m along stations 5 and 6. On comparison with stations such as lines 2 and 8, the average thickness around the common point is 25 m and 30 m. This is due to different locations of this lines (Figure 2.3). Line 4 is at the center of the basin and has more deposits of sediments such trachytes, silts and trona increasing the thickness in line 4 than those in lines 2 and 8.

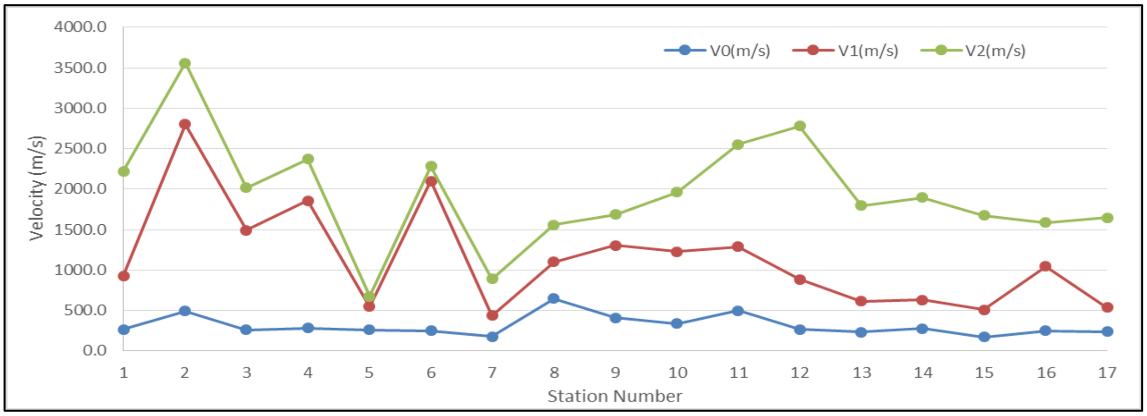

Figure 3. 15: Velocity variation along line 4 (E-W)

The average velocities V_0, V_1, and V_2 of layer 1, 2 and 3 of line 4 decreases in the E-W direction (Figure 3.15). V_0 of layer 1 is generally constant along the profile. V_1 and V_2 of layer 2 and layer 3 have similar properties; both are high in the East and low in the west. Large velocity variations are observed at stations 2, 6 and 12 along the profile as observed in Figure 3.15.

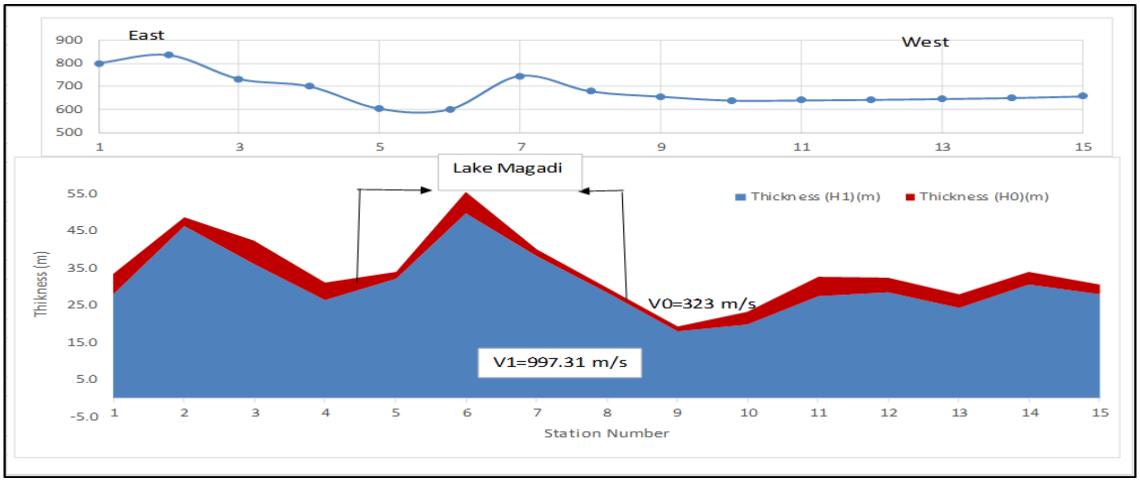

Figure 3. 16: Low Velocity layer variation along line 5 (E-W)

Line 5 passes through Lake Magadi and the thickness of LVL increases westwards as well as the elevation as seen in Figure 3.16. LVL is thicker between stations 1 and 8 approximately 33 m where station 5-8 lies within the Lake Magadi. Beyond station 8, the thickness reduces to about 25 m while the elevation tends to a constant of about 750 m. The average thickness of layer 1 is 3.6 m while layer 2 is 30.8 m. The average velocity for layer 1 is 323 m/s and 997 m/s for layer 2 as in Figure 3.16.

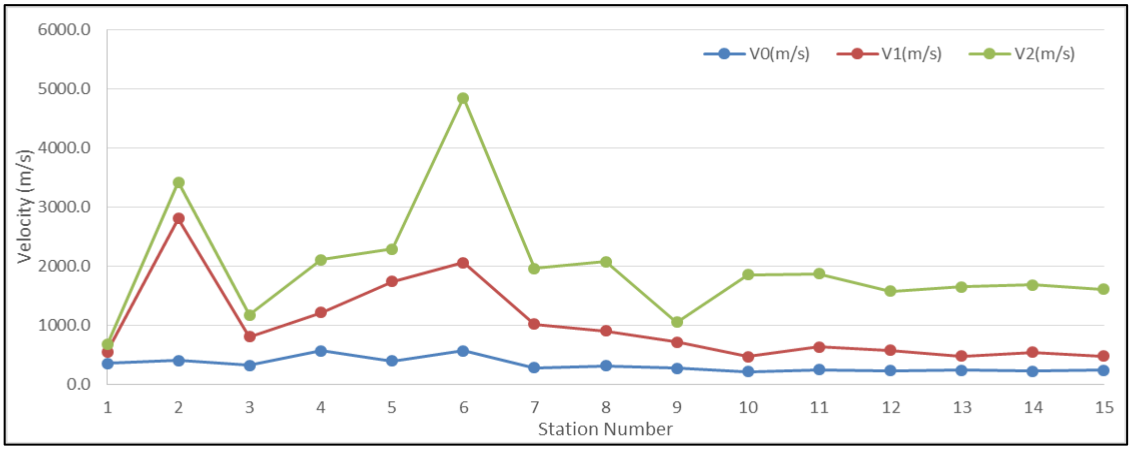

Figure 3. 17: Velocity variation along line 5

Velocity of the first layer of profile 5 (Figure 3.17) is almost constant, a characteristic of all other lines. V_1 and V_2 are high in the east and decreases towards the west. Both layer 1 and layer 2 exhibit similar trends, i.e., have large velocities at station 2 and 6 respectively. The larger thickness and low velocities observed in layer 1 and layer 2 of this line could be attributed to volcanic sediments mainly cherts and trona which are dominant in the area that are carried by run off, hill wash and to a lesser extent wind erosion and are later deposited within and around the lake thus increasing the thickness of low velocity layer.

Line 6 is oriented in the E-W direction. It is the north most line that cuts across transects 1, 2, 7 and 8. Its elevation increases towards the west (Figure 3.18). The first layer is less thick with greater thickness observed at station 4 which is similar to layer 2. Layer 1 has high thickness between stations 3-5, which is also observed in layer 2. The velocity of the first layer is 381 m/s and 1059 m/s. The depth averages to 3.2 m for the first layer and 20.4 m for the second layer resulting in total thickness of 23.6 m of the weathered layer.

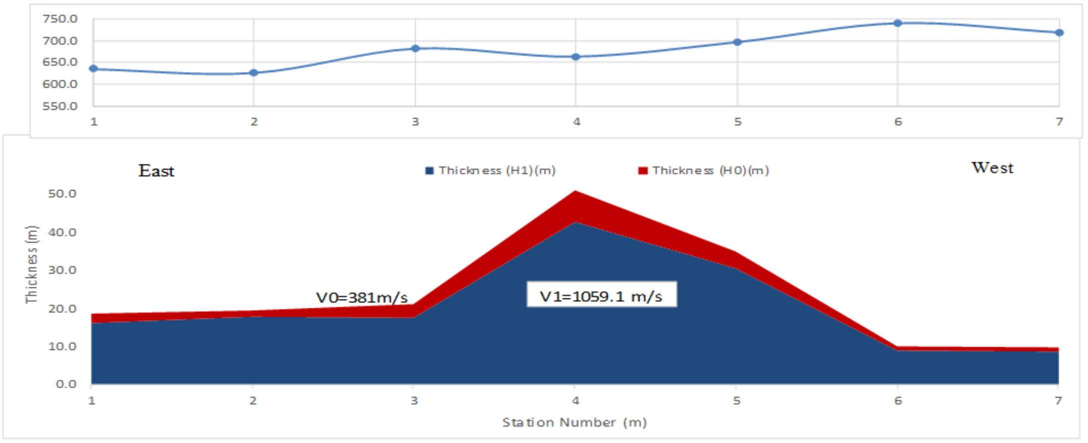

Figure 3. 18: Low velocity layer Variation along line 6 (E-W)

The velocities of layer 1 and layer 2 of this profile are generally constant along the line (Figure 3.19). The velocity increases with increase in altitude implying that the consolidate zone of this layer has been reached in this zone. V_3 of layer 3 increases towards the western side

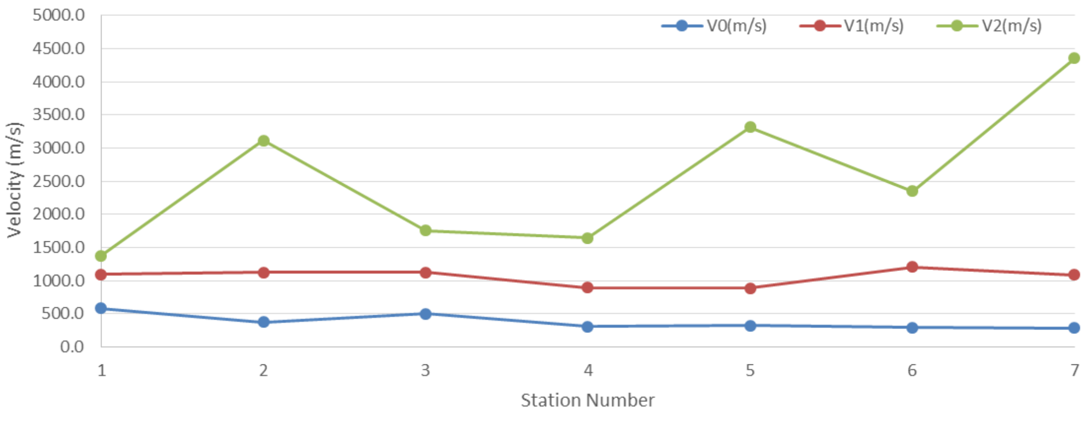

Figure 3. 19: Velocity variation along line 6 (E-W)

3.2 Comparison of Borehole Logs with Refraction Seismic Data

The LVL of Magadi basin is basically made of two layers. This layers composed of volcanics, trona, clay, silts, mud and cherts, (Baker, 1958). Trona is the main rock found within Lake Magadi and in the first layer resulting in low velocities experienced in line 5. Though, silts and mud forms highest percentage of layer 1 in the lake, cherts and clay forms the highest percentage part of layer 2 in the Lake (Figure 3.20).

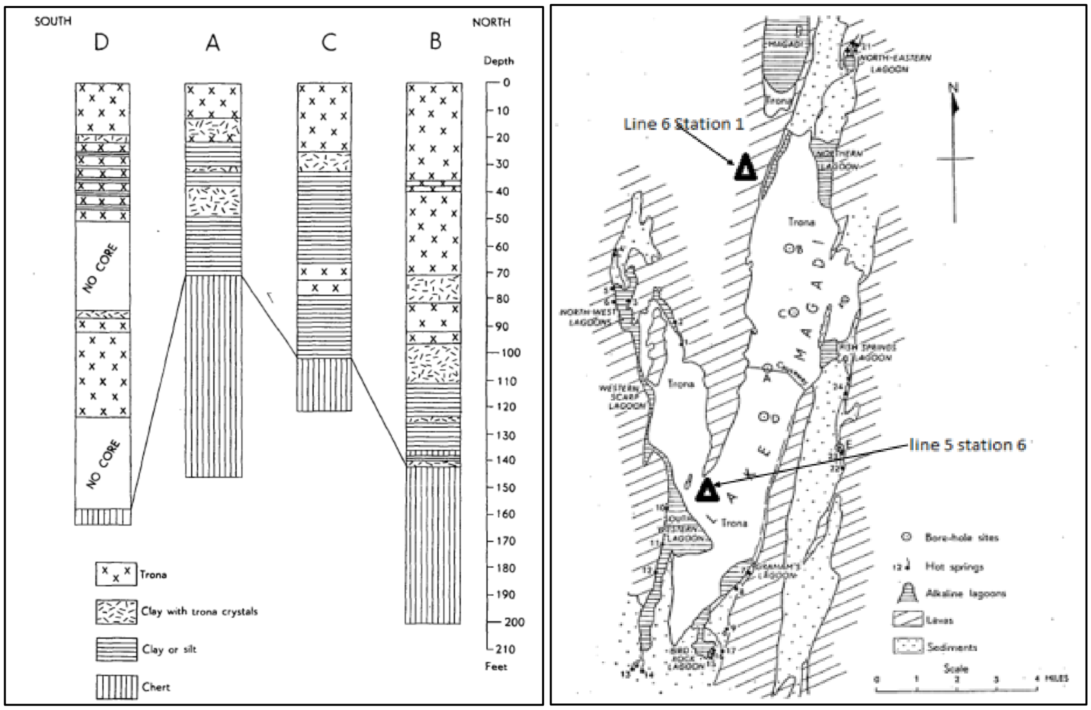

Figure 3. 20: Boreholes logs drilled in the evaporite series (left) and their location in Lake Magadi (Baker, 1958). The red triangle show the closest LVL stations to the boreholes.

Further, the outflowing of volcanic rock from the surrounding hot spring could aid in transportation of this sediments resulting in increased size of the LVZ. Regions beyond Lake Magadi are made of volcanic trachytes and cherts forming the most of the LVL. Finally, LVL are generally distributed in three categories; areas that are approximately uniform, areas where the LVL and other anomalous layers are thicker on hills and thinner in valleys, such as those tied to water table and areas where LVL is thicker in valleys and thinner on the hills; implying more alluvial fill for example and areas where the LVL is distributed almost randomly, (Mike Cox, 1999). Magadi basin falls in second category where LVL and other anomalous layers are thinner on the hills and thicker in valleys implying more alluvial deposits due hillwash (profiles 1, 8 and 6) and where LVL is thinner in valleys and thicker on the hills (profiles 3, 4 and 7) while profile 2 shows random LVL distribution.

The results of the shallow seismic refraction survey of the low velocity layer obtained in Magadi basin from two seismic stations (line 5 station 6 and Line 6 station 1) close to the borehole logs observed by baker, (1958), in Figure 3.20 and more recently by Cohen *et al.,* (2016) were compared to show the composition and the thickness of the low velocity at the given seismic stations. Baker, (1958), observed that over an extensive area in the lake, the trona occurs as a series of evaporites interbedded with clays (Figure 3.20). It is observed from the borehole logs that the trona in all the borehole logs rests on an irregular chert surface. From Figure 3.20, Borehole (BH) logs B and D at the extreme North and South are the closest to LVL Seismic Stations 6 and 1 of line 5 and 6 respectively. The thickness of each layer in stations 6 and 1 were compared with BH logs B and D as shown in Figure 3.21.

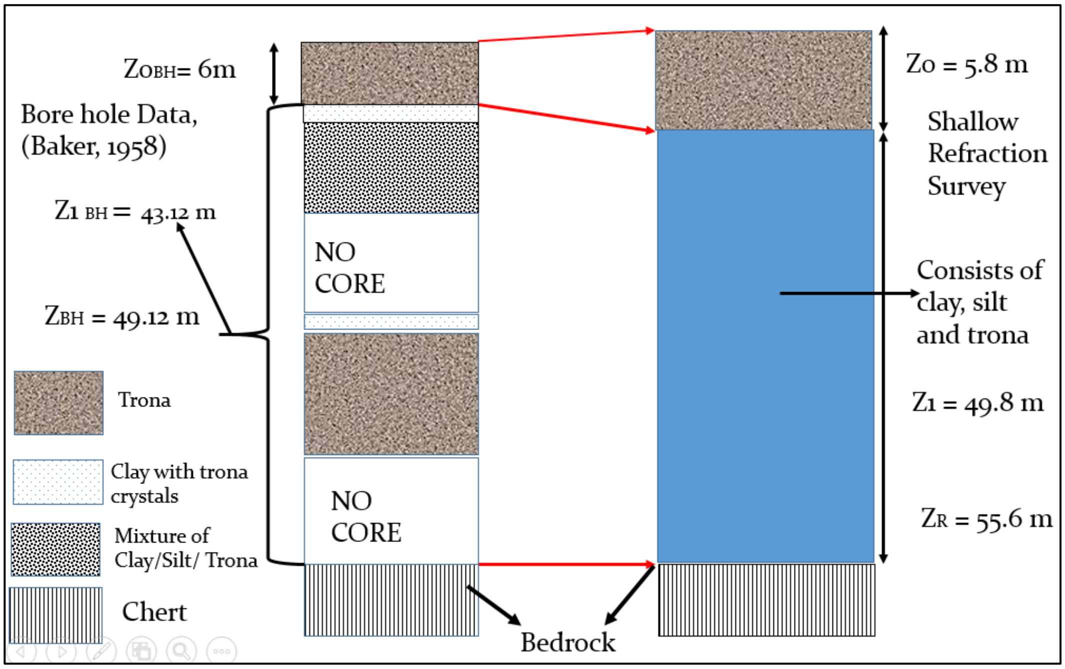

Figure 3. 21: Comparison of Borehole log D data (left) with LVL survey (right) data for line 5 station 6.

From Figure 3.21, it is observed that the first layer is approximately 6.0 m and consists of trona. An observation also made by Cohen *et al.*, (2016) in the Hominin Sites and Paleolakes Drilling Project (HSPDP) to study paleoclimatic records. However, the second layer is a mixture of clay, trona, clay and silts. We observed from Cohen *et al.*, (2016) that the core near station 5 was observed to be non-existent in some depths due to the instability of the core during the drilling, in fact core recovery was poor or non-existent in some depths as seen in Figure 3.21 which could extent to our station. This was because of the interbedded hard and soft lithologies (cherts and unconsolidated muds) which resulted in extremely challenging coring conditions. Cohen *et al.*, (2016) and Baker, (1958) further observed that the Lake Magadi sediments consist of large proportions of trona and other sodium carbonates, cherts and massive lacustrine muds. Muds, mudstones, and cherts in varying proportions dominate the lower stratigraphic intervals throughout the lake which are the composition of the low velocity layer. The thickness of the semi weathered layer from borehole log D and refraction survey (Figure 3.21) is almost similar approximately

50 m. Layer 2 is a mixture of clays, trona, mud and silts and the bedrock is mainly cherts. This is also observed in line 6 station 1 (Figure 3.22).

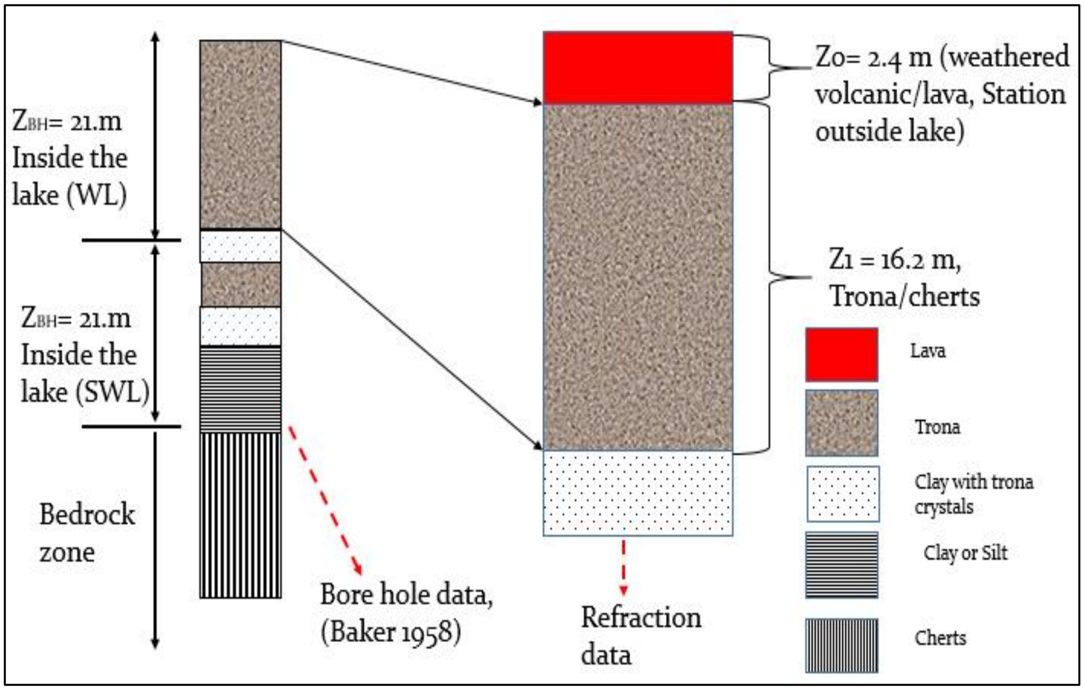

Figure 3. 22: Comparison of Borehole log with refraction seismic data for line 6 station 1

However, this station is adjacent to the lake and the first layer consists of mainly weathered volcanic lava. The first layer is very thin, approximately 2.4 m. The second layer is thicker, about 16.2 m. The layer could be made of trona and mixture of clay and silts as it adjacent to the lake. The bed rock is made of cherts just as seen in Figure 3.21 enabling us conclude that the Magadi basin LVL consists of weathered volcanics, lava, trachytes, cherts, trona mixed with mud, silts and clays.

3.3 Velocity and Thickness Distribution in Magadi Basin

3.3.1 Weathered Layer/ first layer

The average results of velocities and thicknesses obtained at each station were used to plot contour maps of velocities and thicknesses in the survey area by geostatistical process of Kriging (see Appendix 2). Isovels and isopachs were plotted using surfer 10.0 software. A distribution of seismic velocities and respective thicknesses for different layers across the study area is presented and discussed below.

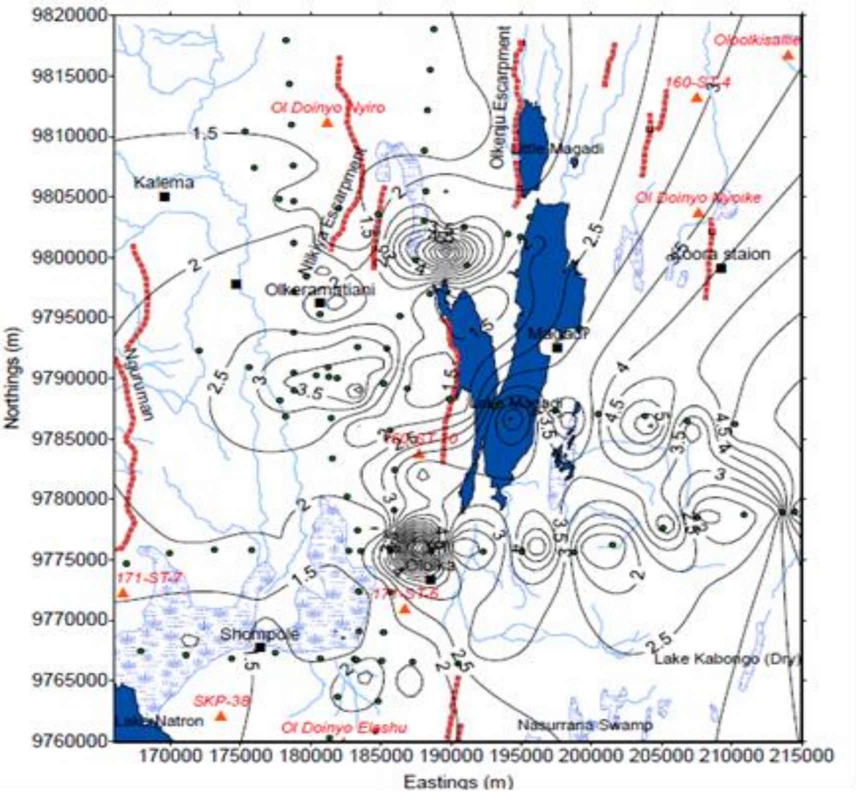

Figure 3. 23: Isopach contour map of layer 1 in Magadi Area with contour interval 1m.

Low thicknesses less than 2.5 m are observed in the Western part of the Magadi basin, Figure 3.23. The thicknesses of less than 1.5 m are observed in south western and north western region of study. This low thickness can be attributed to weathering and erosion of the top surface as the layer lies towards the Nguruman escarpment. The regions close to Nguruman escarpment are slightly steeper and experience more erosion which could result in a thinner first layer. In the southwestern side of study area, the regions encompassing Shompole and areas towards Lake Natron and swampy regions of Mbakasi, the thickness of the first layer is thin and less than 1.5 m. This could be due to erosion of sediments towards the Lake Natron resulting in very low thickness. Majority of western side of the study area have thickness of less than 2.5 m with patches close to Olkiramatian varying between 2.5 -3.5 m. The eastern side has thickness varying from 2.5-12 m. It is the thickest thickness in the first layer. This can be attributed to deposition of volcanic sediments mainly the trachytes, clays and cherts. It may also be due to deposited volcanic sediments and erosion from neighbouring volcanic features like Ol Doinyo Nyokie. This areas cover Lake Magadi and the eastern parts of the study area.

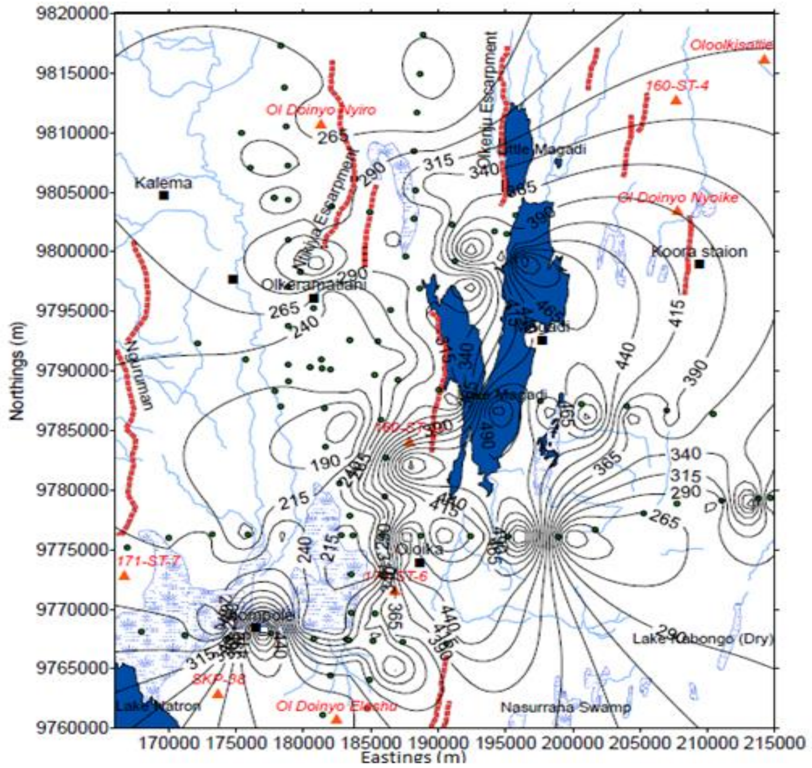

Figure 3. 24: Velocity Contour Map of layer 1 in Magadi basin with contour interval of 25 m/s

Figure 3.24 shows the distribution of velocities in the first layer. It is observed that the weathering velocity decreases generally towards the western side but increases towards the eastern and north eastern areas towards Ol Doinyo Nyokie region. The low velocities in the first layer vary from 140- 290 m/s and is mainly observed in the western and south eastern area of Magadi basin. These velocities are very low and are normally encountered in weathering zone. Higher velocities approaching 600 m/s are observed at the center of the study area, towards NE and the southern parts of the area of study. In general, the velocity in the first layer increases towards the eastern side and decreases towards the western side of the study area.

3.3.2 Semi-Weathered Zone/Second Layer

The semi-weathered zone has great depths towards the eastern part of the study area and within Lake Magadi (Figure 3.25). Low thicknesses are observed in the SW part of the study area and East of Shompole and also in the in the swampy regions. The depths in this area vary from 12-14 m. The thickness observed increases towards Nguruman escarpment and further towards the East. It is observed that as thickness decreases towards the south, so does the velocity (Figure 3.26). Average thickness varying from 16-32 m and are seen clearly in the western part of Magadi basin. Large depths greater than 32 m are observed in the eastern area of study. The velocity in the semi–weathered zone decreases southwards and westwards of the study area (Figure 3.26). However, as the depth and elevation increase towards the east and North, so does the velocity of the semi weathered zone. Most of the region in the south still lies in the low velocity zone as evidenced by the low seismic velocity distribution of less than 1500 m/s except the northern region. These high seismic velocities in the northern region could be due to bedrock of the volcanic rocks being exposed partly by hill wash and wind erosion of the neighbouring volcanic features like the Ol Doinyo Nyokie and Olorgesailie mountains. The large depths in Magadi area are composed of trona, clay, silts, mud and cherts forming the major part of semi-consolidated zone. Further, the outflowing of volcanic rock from the surrounding hot spring could aid in transportation of this sediments resulting in increased size of the LVZ.

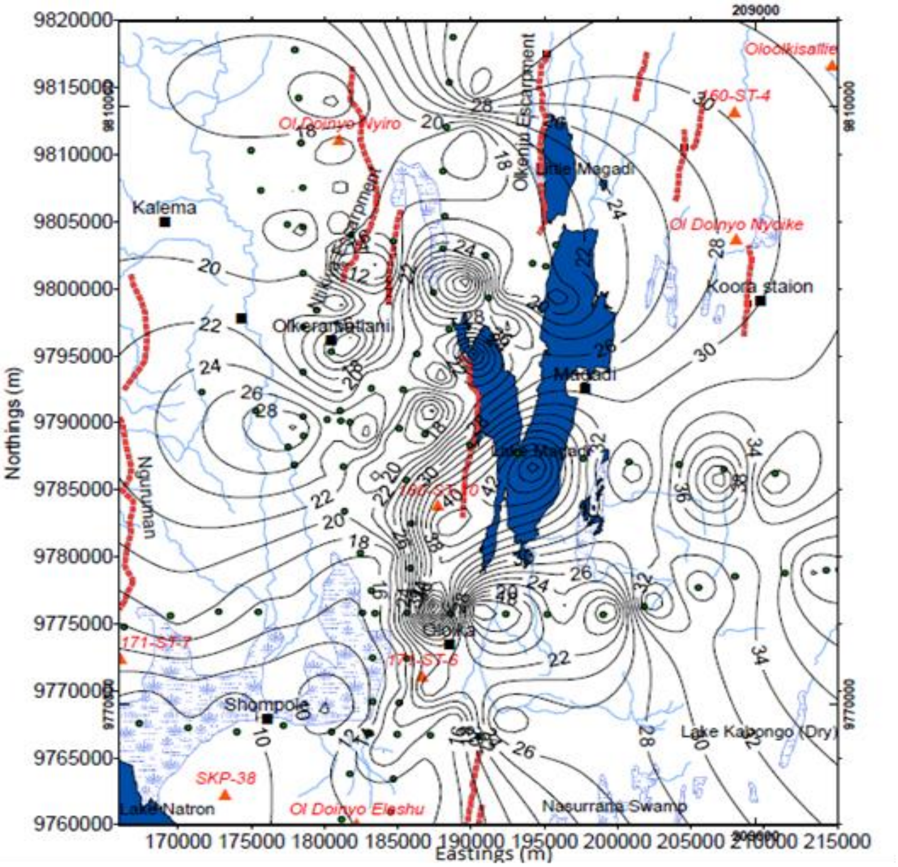

Figure 3. 25**:** Isopach contour map of the second layer.

As earlier noted towards the end of section 3.1.1, low velocity layer are generally distributed in three categories; areas that are approximately uniform, areas where the LVL and other anomalous layers are thicker on hills and thinner in valleys, such as those tied to water table and areas where LVL is thicker in valleys and thinner on the hills; implying more alluvial fill and, finally, areas where the LVL is distributed almost randomly, (Mike Cox, 1999). It is observed from the distribution of Isopachs (Figure 3.25) that Magadi basin falls in all these three areas; areas where the LVL and other anomalous layers are thicker on hills which are Ol Doinyo Nyokie and Olorgesailie, thinner in valleys and those tied to water table and include Shompole and Nasurrana regions; and areas where LVL is thicker in valleys such those around lake Magadi and towards Lake Kabongo caused by alluvial deposits of trachytes, silts, clay and other volcanic rocks from the region; and finally thinner on the hills such areas towards Nguruman and Okenju escarpment caused by erosion of top soil resulting in thin low velocity layer, Figure 3.26.

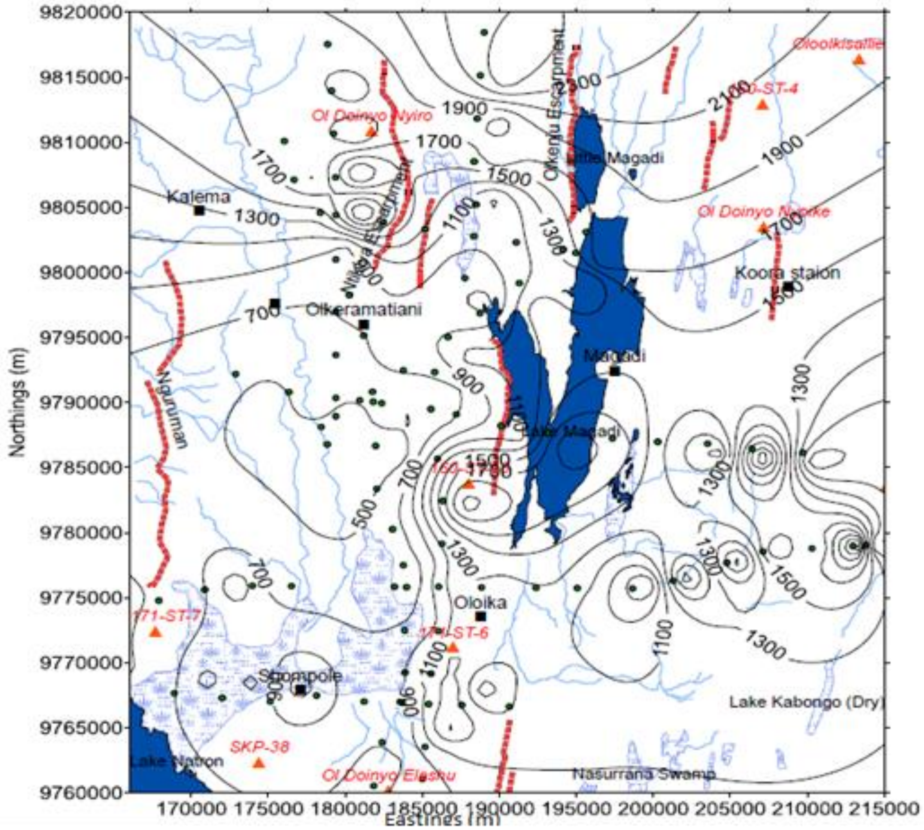

Figure 3. 26: Velocity contour of semi weathered zone

3.3.3 Consolidated Zone/ The third Layer

The region exhibits high seismic velocity distribution in the northern part of study area (Figure 3.27). There is sharp velocity variation in local scale of 3600 m/s to 600 m/s in some parts. This could be regions of non-homogenous layers. Uniform velocity distribution traverses the central part of the study area passing through Lake Magadi towards the south as one approaches the swampy regions. Low velocity distribution is exhibited in the south western and south eastern parts of the study area. Velocities in this region vary from 600 m/s to 1800 m/s with some local region regions having velocities of 2500 m/s. The high velocities are observed in the northern parts with velocities of up to 3600 m/s

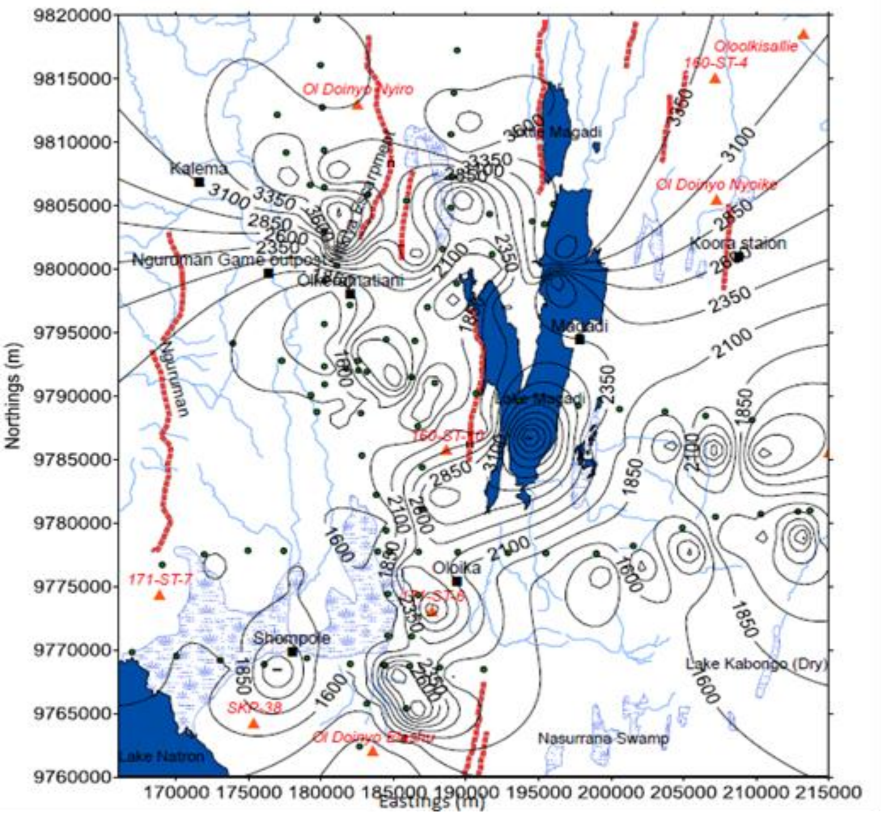

Figure 3. 27: Velocity contour of the consolidated zone

3.3.4 Effect of Geology on the Distribution of the Low Velocity Layer

The Magadi basin is classified into three formations by Baker (1958, 1963) namely; Precambrian metamorphic rocks, Plio-Pleistocene volcanics, the Holocene to Recent Lake and fluvial sediments as illustrated in the geological map (Figure 1.2) and discussed in Chapter one. This distribution of geology has a bearing on the distribution of the LVL in the Magadi Basin. It has been observed in section 3.3.1 and 3.3.2 that thickness of LVL increases toward the East and North and decreases westwards and southwards.

Three central volcanoes exist in Magadi basin; olorgesailie, Ol Doinyo Nyokie and Shompole and are susceptible to weathering and erosion. Due to erosions and hillwash; trachytes, clays, silts and cherts are carried and deposited in eastern and around the lake resulting in high thickness of the LVL around the lake and eastern regions. These volcanics are also weathered and strongly carried by inflow of water characterized by sodium resulting in increase of the trona in the Lake which is the main composition of the weathered and semi weathered zone in the lake and surrounding regions. There are also defined cherts at Oloronga beds that form the oldest sediments in Magadi basin which make up the bedrock in Lake Magadi (Figure 3.20) and further results in increase in LVL around Lake Magadi.

The basement rocks in Magadi basin outcrop in the region west of the Nguruman escarpment and consists of mainly metamorphic rocks such as basalts, banded schists, gneisses and muscovite-rich quartzites. At Kirikiti platform these rocks are interbedded with conglomerates; gravels and sands deposited between different eruption episodes, Baker (1958). The rate of weathering on these rocks is very slow, resulting in very low thickness of the LVL towards the west and the south which consists of conglomerates, gravels and sands. This low velocity layer is also due to hillwash, erosions by rain, animals which are carried down towards the Lake Magadi decreasing the thickness of LVL in this areas. Profiles 3 and 4 (in Figure 1.2 and 2.3), are found in swampy regions of Shompole which has the least thickness of the LVL (Figure 3.25). The basement of the rocks here are mainly basalts which have very low rate of weathering. There are fluviatile deposited sediments of mud, clay from the surrounding lakes which makes up the composition of the LVL in the south. Finally, the LVL is also composed of Magadi Trachyte series consisting of alkali lava sheets extending many kilometers that overlie most of the volcanics in the area which are covered by volcanic ash lava which is observed in most parts of the Magadi basin

3.4 Static Corrections

3.4.1 Introduction

Reflection times often are affected by irregularities in the near-surface. This irregularities cause distortions caused by a structural complexity deeper in the subsurface, more often they result from near-surface irregularities. For land data, reflection travel times are reduced to a common datum level, which may be flat or vary (floating datum) along a line. Reduction of travel times to a datum usually requires correction for the near-surface weathering layer in addition to differences in elevation to source and receiver stations. Recently, geophysical exploration has moved into more difficult areas with complex terrain and tough geological conditions, this has led to more serious statics problems. Estimation and correction for the near-surface effects usually are performed using refracted arrivals associated with the base of the weathering layer. These corrections remove a significant part of the travel time distortions from the data specifically, long-wavelength anomalies. Nevertheless, these corrections usually do not account for rapid changes in elevation, the base of weathering, and weathering velocity. The complex low velocity zone is characterized by the sharply undulated terrain and the big near-surface variations. Static corrections are defined as corrections applied to seismic data to compensate for the effects of variations in elevation, weathering thickness and weathering velocity with reference to a datum. It makes use of shotpoints and receiver points corrected from the surface to the datum which is regarded as a new surface.

There are many factors which make the static corrections and residual static corrections difficult to handle. These factors are rugged surface acquisition topography, non-planar refractors, near-surface low-velocity layers, lateral variant velocities of weathering layers and variations of underground water tables. Errors in static corrections lead to the losses of seismic resolutions, both temporal and spatial, and bring the difficulties and confusions during the interpretations of seismic sections, (Zhu *et al.,* 2014). The common ways to find potential reservoirs is to look for structural and stratigraphic traps with the help of sophisticated imaging and interpretation software. The images are obtained by using sequences of processing steps, and therefore the interpretation can only be reliable when all these steps are correct and sufficiently accurate (Jhajhria, 2009). Figure 2.31 shows the basic steps used in processing reflection seismic data.

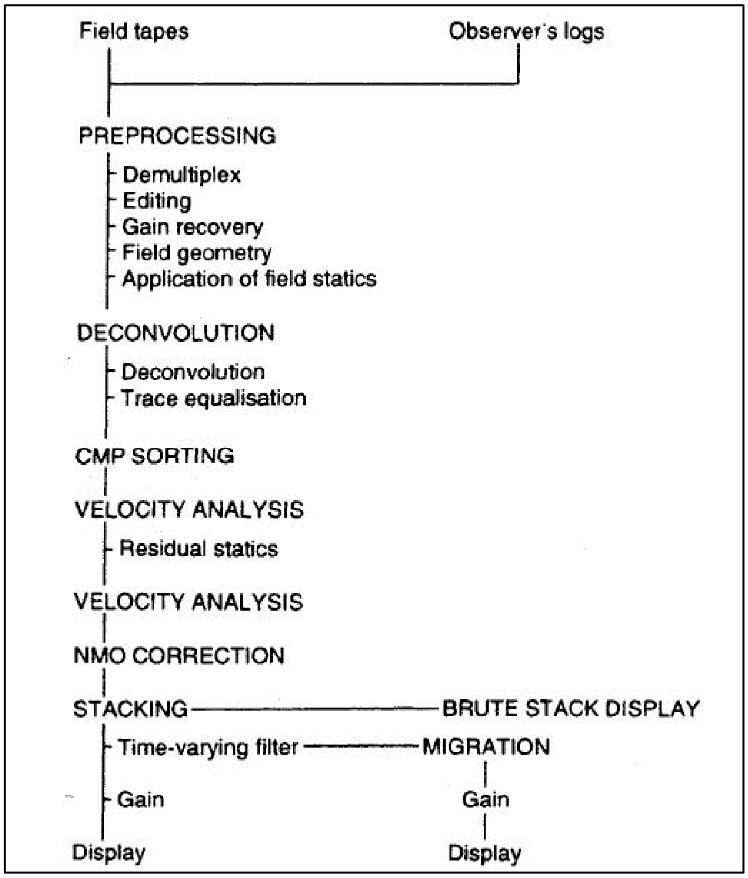

Figure 3. 28: A typical seismic data processing flowchart, (Yilmaz, 2000)

One of the key steps of seismic data processing is the statics correction which are travel time corrections that account for the irregular topography and near-surface weathering layer. They are commonly known as field statics or refraction statics corrections, (Yilmaz, 2000). Not all the processing steps follow those in Figure 3.28, but it gives the general idea of how the processing of reflection seismic data is done. There are four static correction methods used in analyzing reflection data. These methods are field statics, refraction statics, tomographic statics and residual static corrections. However in this study, focus is made on refraction static method discussed in section 1.8.

Magadi Basin has a complex terrain (see Figure 1.1). The region consists of Lake Magadi which is a water mass, to the West is Nguruman Escarpment that has varying elevation. In the south and the regions surrounding is Shompole swamp. To the north is Ol Donyo Nyokie and Olorgesailie volcanoes that have exists in the area of study. This complex terrain has contributed to a low weathered zone that has great effect on the travel times of reflected seismic waves and needs correction for better resolution and imaging lithologic geological structures within the subsurface as observed in the previous section. This section examines a single profile (line six) in the area of study whose data was made available (the rest of the data in other profiles is proprietary and is therefore not used in this section) to demonstrate the effect of the reflected seismic section with and without applied static corrections. First, the static correction for line 6 in Magadi basin is computed using the obtained thicknesses and velocity (Section 3.1.1) of the layers for each station for shallow refraction data. Static corrections for each source and receiver station was computed using equations (50) and (51) to a datum of 600 m by using the velocity and thickness obtained using intercept time at each station for shallow refraction survey. A standardized replacement velocity value of 2000 m/s was used. The replacement velocity is the velocity normally used for static corrections, also called the datum velocity. By application of equations (50) and (51) in Section 1.8, source and receiver static corrections for line six were computed for shallow refraction survey (Figure 3.29) and deep reflection seismic data (Figure 3.30). The statics from shallow refraction survey were used as a control for deep reflection seismic data for line six. In Figure 3.29, the top graph is the elevation which increases along the profile with maximum height observed between stations 1301 and 1351. This is also the area which has large static shifts required because the size of the low velocity layer in this region is also large, hence more travel time. The bottom of the graph is the static corrections made along the profile. The statics are also computed from deep reflection seismic data for line six in Figure 3.30 to the same datum of 600 m and replacement velocity of 2000 m/s. Both results are observed to be the same (Figure 3.29 and Figure 3.30). The statics in both cases lie between -10 ms and -100 ms. These, in both cases, increase along the profile with large static corrections required between station 1251 and 1451 along the profile. This is due to the large weathering zone between these stations. In both cases, a datum of 600 m was used since it lies slightly below consolidated zone which is not affected by the effects of the LVL. Further towards the west, statics are fairly constant with decrease in elevation and thickness of the low velocity. Finally the statics increase towards the end (station 1701) due to increase in the low velocity layer.

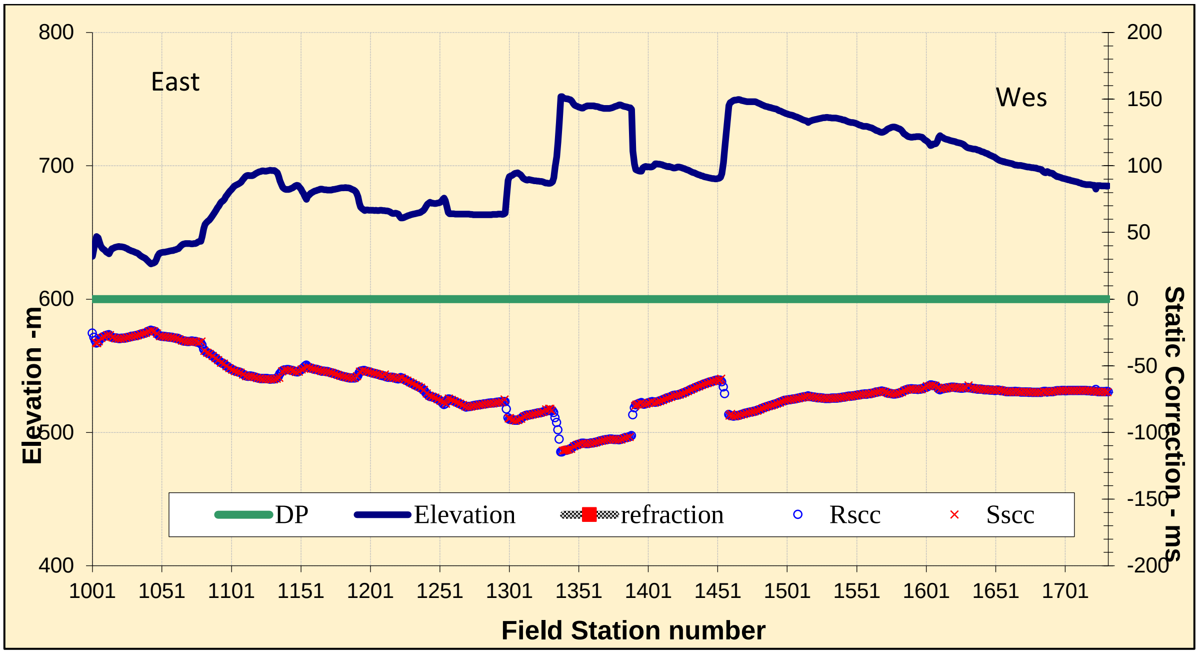

Figure 3. 29: Low Velocity Layer Model and Static Correction for Line 6

From Figure 3.29, DP- Datum plane (600 m), Rscc- Receiver static correction, Sscc- Source static correction. A sum of both receiver and source static correction is the refraction static as in equation 52. For this profile 6 in Figures 3.29 and 3.30, refraction static correction is the sum of receiver and source static correction at the given source and receiver station. The difference between the two figures is; Figure 3.30 does not have elevation which is observed in Figure 3.29

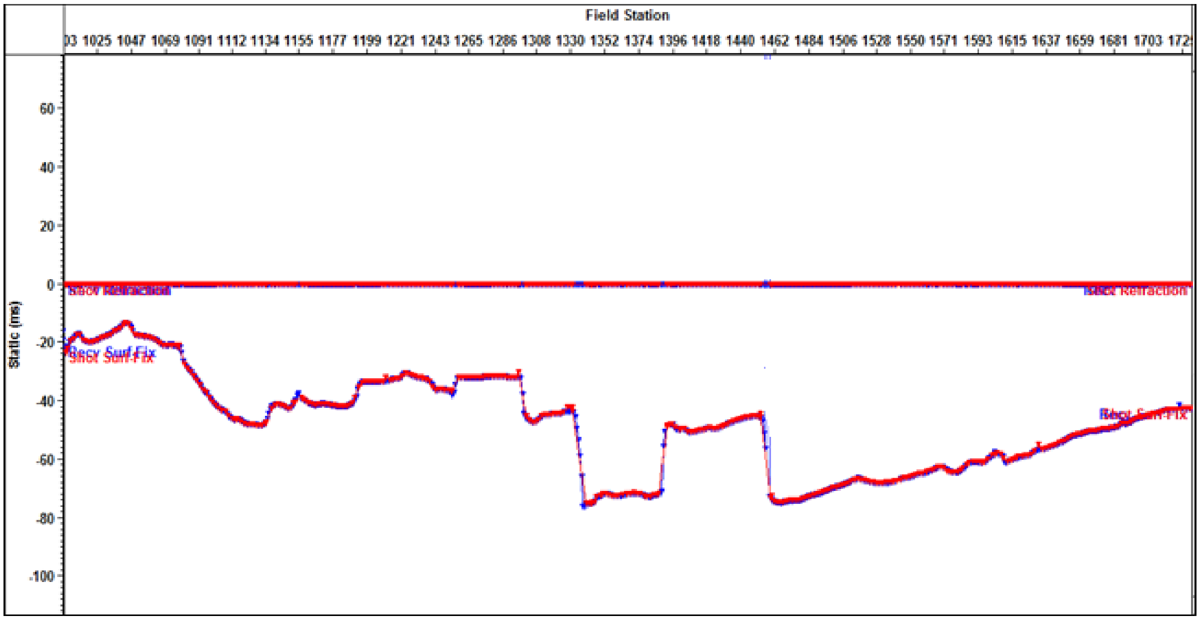

Figure 3. 30: Refraction statics for line 6 using 2D/3D Vista

In order to see the effect the effect of static corrections on the processed data, the steps outlined in Figure 3.31 were followed and the stacks with and without statics obtained and compared to see the resolution of the stacks when static correction is applied.

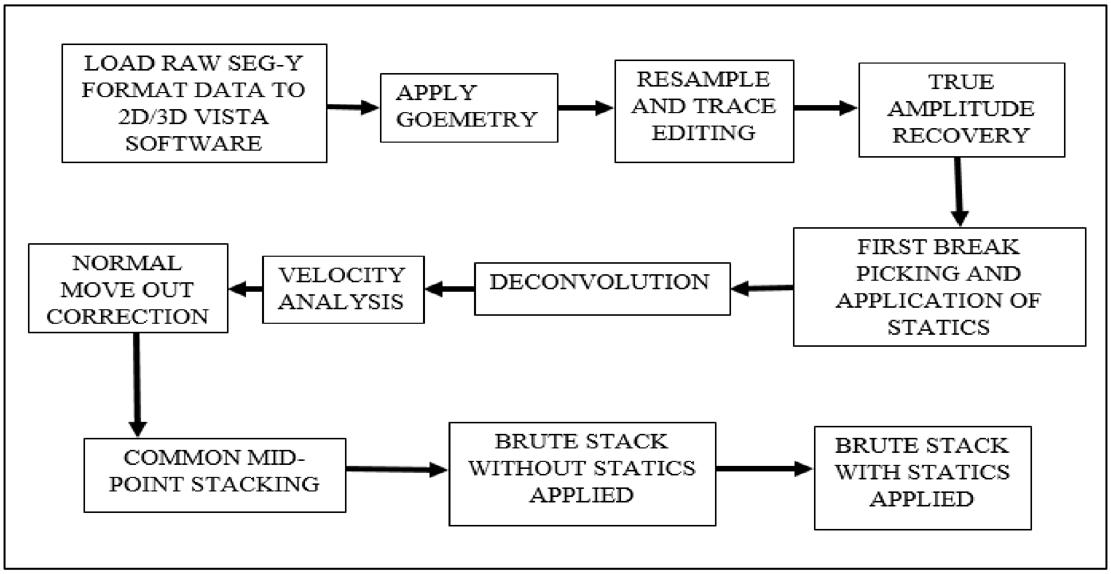

Figure 3. 31: Flow chart diagram for application of Statics to reflection seismic data for line 6

LOAD SEG-Y FORMAT- The acquired raw data was input in to the 2D/3D Vista seismic software. During this stage, the raw shot records were displayed on the screen QC of the raw data was performed, which included Identification of bad shot records (if any), Repeated FFIDs (Field File Identification No.), total number of channels, record length among others.

GEOMETRY APPLICATION- This step provides spatial coordinates of the seismic source and seismic detector for each data trace recorded in the survey. The relationship between seismic velocities, source detector separation and reference to ground locations and elevations were input using the SPS file. Once the geometry was applied, it was then re-written into trace headers.

RESAMPLE AND TRACE EDITING- Resample is the reduction of the data to a smaller sample rate (higher sample interval) to avoid processing twice as many numbers. It is normally applied near the start of the processing but not in any particular position. The data was re-sampled from 2 ms to 4 ms sample rate. Recorded field data generally shows that some of the traces are partially or completely corrupted due to immense noise or by the effect of loose ground coupling, which may cause deterioration of the stack. In order to cure this problem, every shot was displayed on screen and bad traces were edited.

TRUE AMPLITUDE RECOVERY- The amplitude of seismic energy decreases with increasing source detector distance. True amplitude recovery (TAR) with time power constant was applied to the data to compensate for the loss of amplitude due to wave front spreading and inelastic attenuation. Automatic Gain Control (AGC) was used to adjust the signal amplitude as an identical average value. An exponential gain function was used to compensate the attenuation losses.

FIRST BREAK PICKING- The first break picking of reflection seismic data was done for all the short records points along line 6 and the results obtained used to compute receiver statics and shot statics at each shot point along the profile, (Figure 3.30).

REFRACTION STATIC-Already described this section on refraction statics.

DECONVOLUTION- Deconvolution compresses the basic wavelet in the recorded seismogram, attenuates reverberations and short-period multiples, thus increases temporal resolution and yields a representation of subsurface reflectivity. The process is normally applied before stack. However, it is also common to apply deconvolution to stacked data.

VELOCITY ANALYSIS- Seismic velocities are the most important geophysical parameters for the interpretation of subsurface features. Seismic velocities are generally needed for the investigation of subsurface lithology, physical nature of the rocks and the calculation of dip and depth interfaces. Velocity analysis is the calculation of stacking velocity (Vs) or normal moveout velocity (Vnmo) from the measurements of normal moveout, (Al-Anezi, 2010). Vista software displays three different tiles or panels; semblance, gather and continuous velocity stack (CVS) where the selection of velocity is made in the semblance tile. The semblance tile is actually a contour map of semblance coefficients. The trial velocity corresponding to a high semblance coefficient is the RMS (Root Mean Square) velocity in the zone above the reflector. A semblance coefficient map can provide a clue that how many reflectors are present and how the RMS velocity waves reflected from them (Yilmaz, 2000). The CVS tile computes and displays the constant velocity stacks for further analysis. The remaining two tiles are the gather tile and max semblance/interval velocity tile. Interval velocity is calculated and updated by the Dix equation as soon as the selection of velocity is made.

NMO CORRECTION- The time difference between traveltime at a given offset and at zero offset is called normal moveout (NMO). The velocity required to correct for normal moveout is called the normal moveout velocity, (Yilmaz, 2000). NMO-correction was applied to the data in order to yield zero-offset recordings. NMO correction depends on time, offset and Root Mean Square velocity. The arrival time for seismic reflection as a function of offset can be approximated by hyperbola. A common mid-point (CMP) stack was obtained by summing those traces over offset to their correct position, i.e., each at the position of their common reflection point to create a seismic section.

BAND PASS FILTER-An Ormsby zero-phase Band pass filter was applied to remove residual low frequency noise during the processing. The frequency range was (1 - 5) / (35 - 40) Hz.

COMMON MID-POINT STACKING- Stacking is adding or averaging seismic signals. Common-midpoint stacking (CMP stacking) is used to improve the signal-to-noise ratio and to attenuate multiples. The CMP technique uses redundant recording to improve the (S/N) ratio. The NMO corrected traces from different records, due to rays reflected at positions near the common depth point, are summed up (stacked) and displayed as one trace at normal incidence (zero offset). The result is a composite record in time domain which reflects the structural image underneath the survey line. The NMO-procedure was applied assuming a near horizontally layered conditions. When dipping reflectors are stacked the reflection points are smeared. In these cases, a special dip moveout processing routine (DMO) is applied to correct for the smearing effects, (Knödel *et al.*, 2007). Finally, two CMP stacks were obtained (with refraction statics and the other without statics) by summing those traces over offset. A comparison between the two stacks (Figures 3.32 and 3.33) was done to see the effects of the structural differences between them.

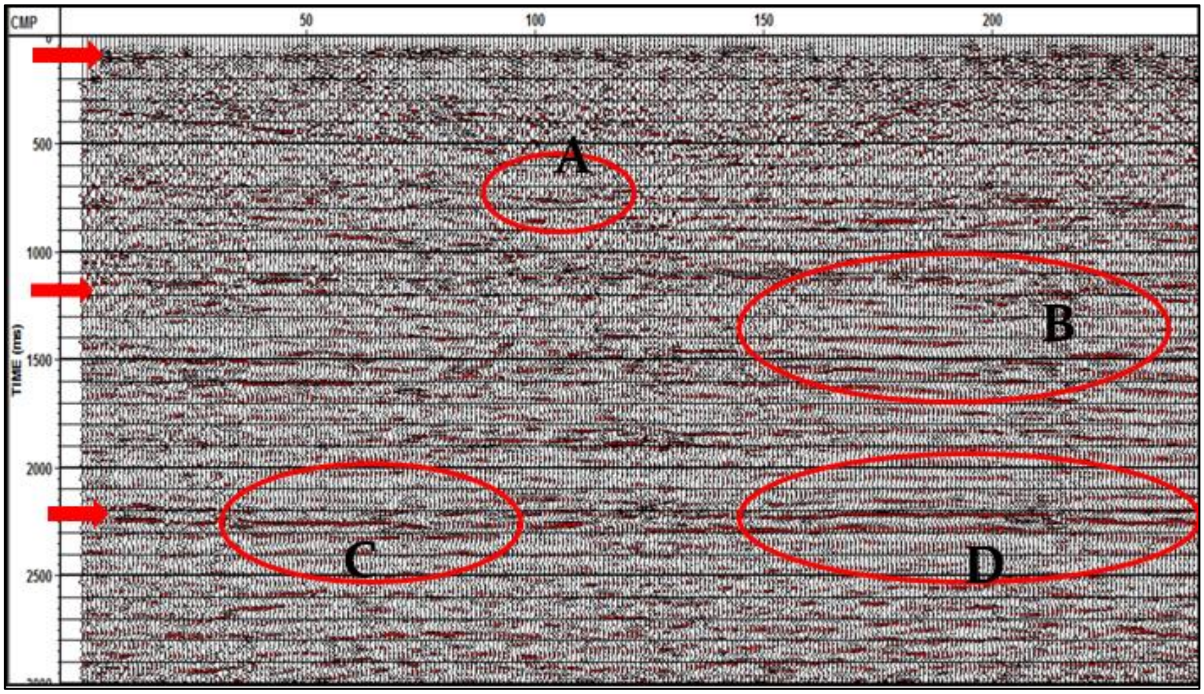

Figure 3. 32: Brute stack without application of static corrections to reflection seismic data.

Figure 3.32 is a reflection brute stack without static corrections. It is observed that the reflected images which represent seismic layer boundaries at the time intervals 800 ms, 1200 ms, 1500ms and 2200 ms and also for regions marked A, B, C, D are not defined clearly due low or lack resolution since the statics have not been applied. In fact at 800 ms, the image of the seismic reflected boundary layer is not seen at all. However, in Figure 3.33 which shows a brute stack with applied statics, the reflected layer boundaries at 800 ms, 1200 ms, 1500 ms, 2200 ms and of regions marked A, B, C, D of the reflection seismic stack are more defined (have higher resolution) and can be seen more clearly because the statics correction has been applied. If sections marked A, B, C and D in Figure 3.32 are compared with those in Figure 3.33, we see that the imaged portions of these sections are clearer and have been resolved into better defined reflected strata boundaries. If a structural feature such as trap is in this section or any other, it could be resolved and seen more clearly. In this data, positive statics have been applied (have moved the data away from time zero creating dead data at shallow times as seen in Figure 3.33) while negative static value moves the trace towards time zero (strips off shallow data). It is observed that static correction is necessary in order to map clearly deeper structural features for hydrocarbon exploration.

Stein *et al.*, (2009) observed that near surface anomaly is expressed in three ways; severely affecting the recorded times of the reflection seismics and ultimately the clarity and the position of the strata in the image as seen in Figure 3.33 and therefore affecting the type and magnitude of the generated noise and distorting the signal amplitudes. Due to their shallow occurrence in seismic data, the static effects of these near surface complexities cannot be suitably resolved by migration, velocity analysis hence the need for Static correction. Therefore, proper statics solutions are definite desirable for obtaining high-resolution seismic sections which can be used for stratigraphic and lithologic interpretations as seen in Figure 3.33 leading to mapping and locating deeper features for hydrocarbon and gas for exploitation.

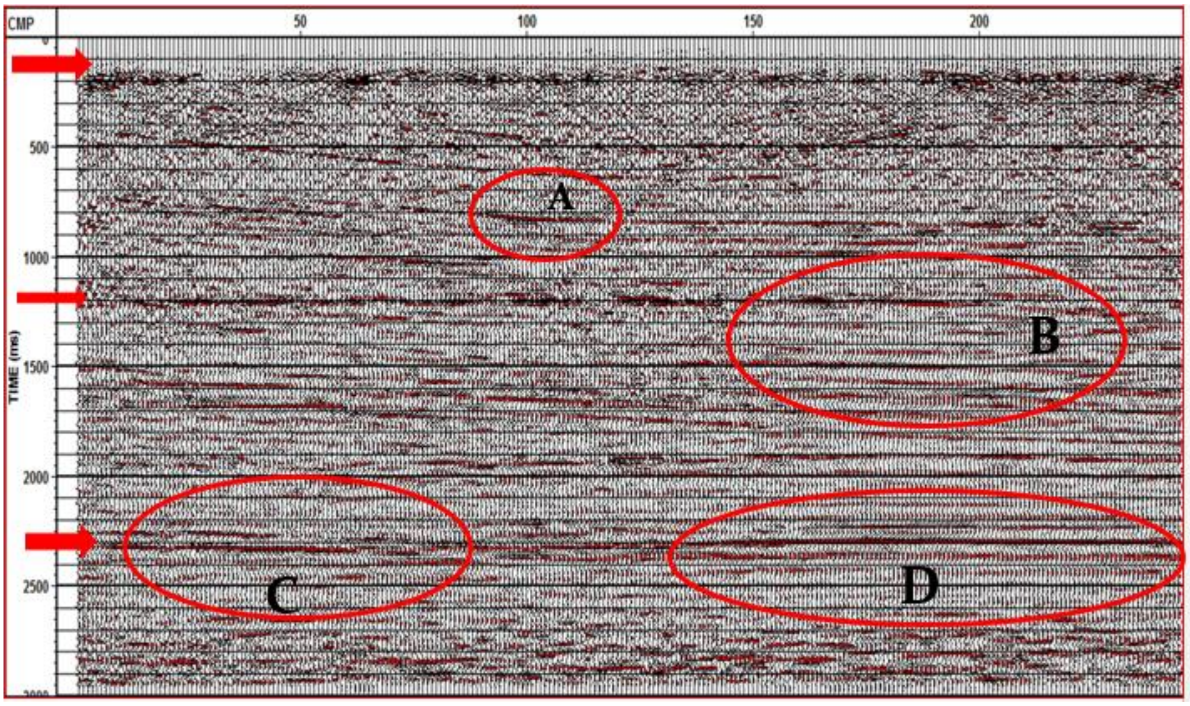

Figure 3. 33: Brute stack with static correction applied to reflection seismic data

3.5 CONCLUSIONS AND RECOMMENDATIONS

3.5.1 CONCLUSIONS

It can be observed that weathering velocity decreases generally towards the south with the most significant drop occurring in the South West. Seismic velocities within the consolidated layer appear to decrease gradually towards the south but with a sudden and most significant increase in the North. This shows a northward extension of a substratal geophysical anomaly. The velocity of the consolidated layer is highest at the points where the thickness of the weathering layer is most. The study reveals that weathering thickness generally increases northwards and eastwards as elevation increases towards the same direction. Normal faulting in the weathering layer followed by hill wash and normal erosion on the surface allowed for more deposition of sediments in the Lake Magadi and the surrounding regions thereby significantly increasing the thickness of the weathered zone in this regions and around Lake Magadi. Further, the geology in this area has significant effect on low velocity layer with regions having volcanic formations and low altitude prone to high thickness of the LVL.

At small dip angles it was observed that in approximately 90% of the reversed set of shallow seismic refraction cases, the averaging of updip and downdip velocities yields satisfactory results for velocity and thickness in the subsequent layers as observed in Table 3.2 and Table 3.3. The average of forward and reverse shooting velocities were used to calculate the true velocities and thickness of each layer at each station in all the eight profile in Figure 2.3. A three layer model of the low velocity zone is obtained; the weathered zone, the semi-weathered zone and the consolidated/ bedrock zone.

The average thickness of the weathered layer to the top of the sub-weathered zone is 2.6 m with an average velocity of 310 m/s. The weathering thickness ranges from 0.5 m in the swampy areas of the southern parts and increases to 4.5 m in the Eastern parts with maximum thickness observed in Lake Magadi. The calculated velocity ranges from 145.1 m/s in the south to 648.7 m/s in the northern region. The low weathering thicknesses and velocities observed in Shompole and swampy areas of the south through the south-west indicates the presence of loose unconsolidated and aerated soil materials mainly clay which may lead to high absorption of seismic energy. This general variation in the thickness of the weathered layer may, if not corrected for, may lead to false indications of significant structural features. The sub-weathered zone has velocities ranging from 380.3 m/s to 2802.3 m/s with an average of 1085.5 m/s. The depths range from 7.4 m to 52.0 m with an average of 22.9 m. The bedrock or the consolidated zone has velocities ranging from 671.8 m/s to 4844.4 m/s with an average of 2208.1 m/s. The average depth from the weathered zone to the bedrock is 25.5 m. There is large thickness variation around and within Lake Magadi. The results also showed that the weathered zone is averagely 31.3 m beyond which the bedrock begins, (Baker, 1958). This results are similar to shallow refraction data where the average depth to the bedrock in the southern part of Magadi and Northern part varies from 28-32 m. The low velocities observed on semi-weathered zone could be as a result of hydrothermal–saline conditions and reworked or sheared sediments consisting of clay, trachytes and mud which is in contrast with bedrock of higher velocities as observed in the consolidated zone.

These fragmented sediments of mud, clay and trachytes leads to low velocities in the weathered and parts of semi-weathered layer implies the weathering zone could result in adverse effect on deeper reflection seismic data. Application of statics to deep reflection seismic data leads to good resolution of image reflected layers and lithological characteristics of a given seismic section as seen in Figure 3.33 Therefore, this region requires static correction to be applied when processing deep seismic reflection data to map clearly deeper structural features for hydrocarbon location.

3.5.2 RECOMMENDATIONS

The presence of a variable low velocity layer in Magadi basin shows that deep reflection seismics will be impacted due to this layer. It is therefore necessary that it should be taken into account to eliminate the effects associated with the low velocity layer so that good quality data is obtained for clear structural and lithological interpretation of reflection features necessary for hydrocarbon location. The study recommends uphole survey to be carried in the area so that uphole data can compliment refraction survey that was carried out. Core samples can be obtained from uphole for further analysis to get the lithological characteristics of the low velocity layer in Magadi Basin. Since low velocity layer has great impact on seismic reflections, care needs to be taken when processing deep reflection seismic to ensure good and structural resolution of sub-surface features. This study suggests for meaningful and clear mapping of subsurface structural and lithological features in Magadi Basin, static correction needs to be applied to deep reflection seismic data in the study area.

REFERENCES

Al-Anezi, G. T. (2010). *Investigation of Weathering Layer Using Seismic Refraction and High Resolution Reflection Methods*, Published Msc Thesis. Department of Geology and Geophysics, College of Science: King Saud University.

Alaminokuma G. I. & Amonieah, J. (2012). Near-surface structrural model for enhanced seismic data acquistion and processing in Norht -Central Niger Delta. *American Journal of Scientific and Industrial Research, 3*(5), 252-262.

Anomohanran, O. (2014). Downhole seismic refraction survey of weathered lare characterization in Escravos, Nigeria. *American Journal of Applied Sciences, 11*(3), 371-380.

Baker, B. (1958). *Geology of the Magadi area.* Nairobi: The government Printer.

Baker, B. (1963). *Geology of the area of the South Magadi.* Nairobi: The government Printer.

Baker, B. H & Wohlenberg J. (1971). Structure and Evolution of the Kenya Rift Valley. *Nature*, *229*, 538-542.

Backhouse R. W. & Long R. E. (1976). The structure of the Western flank of the Gregory Rift Part 1. The Mantle. *Geophysical International journal, 44*(3), 677-688.

Bonjer. K. P., Fuchs K. & Wohlemberg J. (1970). Crustal Structure of the East African Rift Sysstem from Spectral Response Ratios of long Period body waves. *Journal of Geophysics, 36,* 287-297.

Cohen A., Campisano C., Arrowsmith R., Asrat A., Behrensmeyer A. K., Deino A., . . . Zinaye B. (2016). The Hominin Sites and Paleolakes Drilling Project: inferring the environmental context of human evolution from eastern African rift lake deposits. *Scientific Drilling, 21,* 1-16.

Crossley, R. (1979). Structure and Volcanism in the Southern Kenya Rift. In Geodynamic evolution of the Afro-Arabian Rift system. *Academic*, 89-98.

Drijkoningen, G. (2003). *Seismic Data Acquisition TA3600.* Delft, The Netherlands: Section Applied Geophysics & Petrophysics, Delft University of Technology .

Githiri, J. G. (2009). *Gravity and Magnetic Investigations of the Greater Magadi area in Kenya*. Unpublished PhD Thesis. Nairobi, Kenya: Jomo Kenyatta University of Agriculture and Technology.

Gregory, W. (1921). The Rift Valleys and Geology of East Africa. *London Seeley, Service*, 479.

Gooverts P. (1921). *Geostatistics for Natural Resources Evaluation.* New York: Oxford University Press.

Jhajhria, A. (2009). *Accurate and Automatic Refraction Statics in Large 3D Seismic Datasets*. Unpublished Msc. Thesis, Saskatchewan, Canada: University of Saskatchewan.

Johnson H. Stephen, (1976). Interpretation of Split Spread Refraction Data in terms of Plane Dipping Layers. *Geophysics, 41*(3), 418-424

Keary, P., Brooks M & Hill I. (2002). *An introduction to Geophysical Exploration.* Osney Mead, Oxford: Blackwell Scientific Publications.

Kolawole F., Okror C. & Olaleye O.P. (2012). Downhole Refraction Survey in Niger Delta Basin: A 3- layer Model. *APRN Journal of Earth Sciences*, *1*(2), 67-79.

Knödel, K., Lange G. & Voigt H. N. (2007). *Environmental Geology: Handbook of Field Methods and Case Studies.* Berlin Heidelberg, Germany: Springer-Verlag,

Krisp Working Group. (1987). Structure of the Kenyan Rift from seismic Refraction. *Nature 325*, 239-242.

Lambiase J. J. (1995). Hydrocarbon habitat in the Rift Basins. *Geological society Special publication, 80,* 117-144.

Lawton, D. C. (1989). Computation of refraction static using first-break travel time differnces. *Geophysics, 54*(10), 1289-1296.

Leat P. (1984). Geological Evolution of Trachytic Caldera Volcano Menengai Kenya Rift Valley. *Journal of the Geological Society. 141*(6), 1057-1069.

Li G., Gao C. & Junyi Z. (2009). Analysis of geophone properties effects for land seismic data. *Applied Geophysics. 6*(1), 93-101.

Lowrie W. (2007). *Fundamentals of Geophysics.* Cambridge University Press, New York: United States of America.

Mechie J., Keller G. R., Braile L. W., Mooney W. D. & Prodehl C. (1994). Structure of the Uppermost Mantle beneath the Kenya Rift. *Tectonophysics 236*, 201-216.

Cox M. (1999). *Static Corrections for Seismic Reflection Surveys.* Society of Exploration of Geophysicists, Oklahoma, United States of America.

Morley, C. K. (1999). Geoscience of Rift systems: Evolution of East Africa. *American Association of Petroleum Geologists, 44,* 1-18.

Ngecu, W. A. (1999). Lithostratigraphy and distribution of Pleistocene sediments of the Munyu wa Gicheru formation in South Kenya Rift Valley. *Journal of African Earth Geosciences, 29*(2), 411-421.

Owen R.B., Renaut R.W., Potts R. & Behrensmeyer A.K. (2011). Geochemical trends through time and lateral variability of diatom floras in the Pleistocene Olorgesailie Formation, southern Kenya Rift Valley. *Quaternary Research, 76,* 167-179.

Pap A. (1976). Apparent refraction velocities for dipping interfaces. Canada: Amoco Petroleum Company Ltd.

Rao V. V., Raju J. S., Prakasa R. B. S. & Rao P. K. (2004). Bed Rock Investigation by Seismic Refraction Method: A case Study. *Journal of Indian Geophysical Union, 8*(3), 223-228.

Riaroh D. & Okoth W. (1994). The geothermal fields of the Kenya Rift. *Tectonophysics, 236* (2), 117-130.

Reynolds M. J. (1998). *An Introduction to Applied and Environmental Geophysics*. West Sussex, England: John Wiley and Sons.

Saha S., Mandal A., Borah B. & Gupta M. (2012). *Characteristics of Low Velocity Layer in Upper Assam Basin near Naga Thrust: A brief Study*. 9th Biennial International Conference and Exposition on Petroleum Geophysics, Hyderabad. 249-253.

Stein A. J., Langston T. & Larson E. S. (2009). A Successful Statics Methodology for Land Data. Society of Exploration Geophysicists. *The Leading Edge, 28*(2), 222-226.

Talbot M. R., Morley C. K., Tiercelin J. J., Le Herisse A., Potdevin J. L. & Le Gall B. (2004). Hydrocarbon Potential of the Meso-Cenozoic Turkana Depression, northern Kenya. Source Rocks: quality, maturation, depositional environments and structural control. *Marine and Petroleum Geology*, *21,* 63-78.

Telford M. W., Geldart P. L. and Sheriff E. R. (1990). *Applied Geophysics.* Cambridge: Cambridge University Press.

Yilmaz, O. (2000). *Seismic Data Analysis: Processing, Inversion and Interpretation of Seismic Data.* Oklahoma, Tulsa: Society of Exploration Geophysicist.

Zhu, X., Gao R., Li Q., Guan Y., Lu Z. & Wang H. (2014). Static Corrections Methods in the Processing of Deep Reflection Seismic Data. *Journal of Earth Science, 25*(2), 299-308.

APPENDICES

Appendix 1: Sample Forward and Reverse First Break Pick Time and the Corresponding Time-Distance Graph for Some Stations along the Profiles

Offset (m)	FBT (ms) Left	FBT (ms) Right
0	5.662	6.057
1	8.847	9.518
3	11.089	12.979
5	15.381	16.440
8	20.389	19.902
11	24.418	21.921
16	28.259	29.131
21	36.486	37.944
27	44.714	46.758
33	55.802	55.571
41	65.103	64.384
49	74.403	73.197
59	83.704	82.491
67	94.077	89.846
75	101.947	97.200
81	106.150	104.555
87	110.353	111.910
92	114.556	115.948
97	117.686	117.727
100	120.905	119.506
103	122.694	121.284
105	124.482	123.063
107	126.271	124.841
108	128.059	126.620

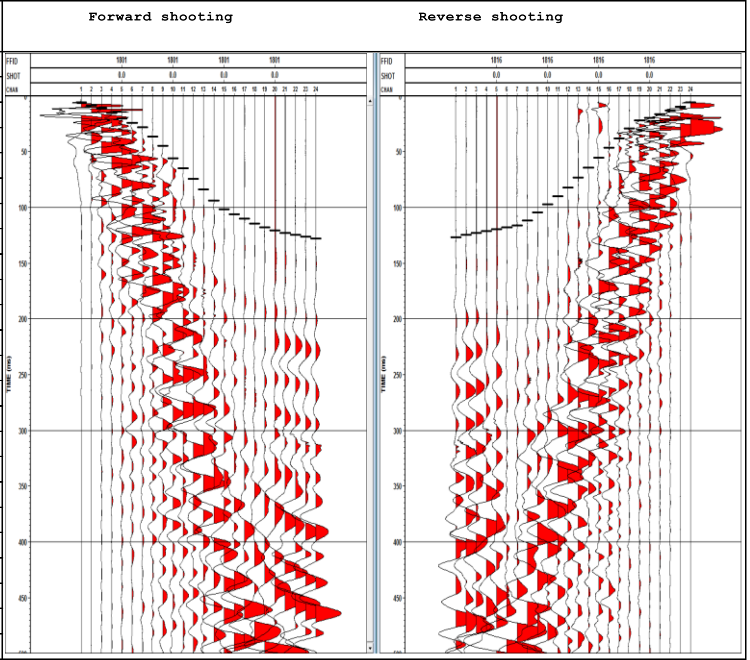

a: Line 1 station 6

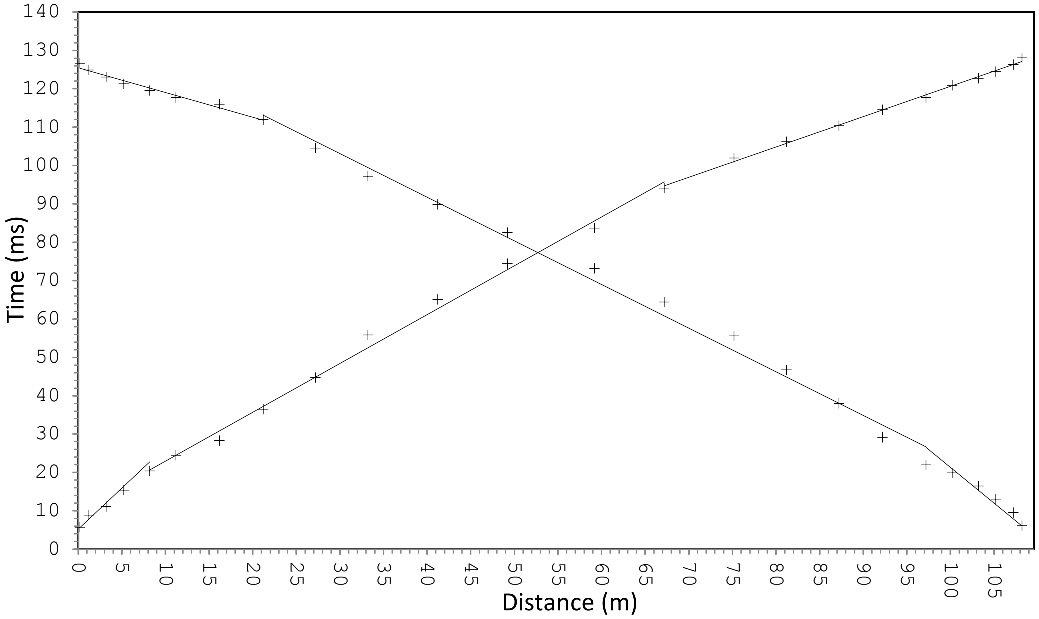

b: Interpretation of LVL of line 1 station 6

Offset (m)	FBT (ms) Left	FBT (ms) Right
0	5.357	4.762
1	8.185	7.738
3	11.607	10.714
5	17.857	15.476
8	21.825	22.024
11	27.381	28.571
16	35.516	35.119
21	43.651	41.667
27	51.786	53.571
33	67.262	65.278
41	76.191	76.984
49	90.476	88.691
59	104.762	107.143
67	120.238	123.512
75	129.315	135.714
81	138.393	142.857
87	147.470	150.000
92	154.762	154.018
97	157.143	157.738
100	159.524	160.119
103	161.786	162.054
105	163.214	163.988
107	164.643	165.923
108	166.071	167.857

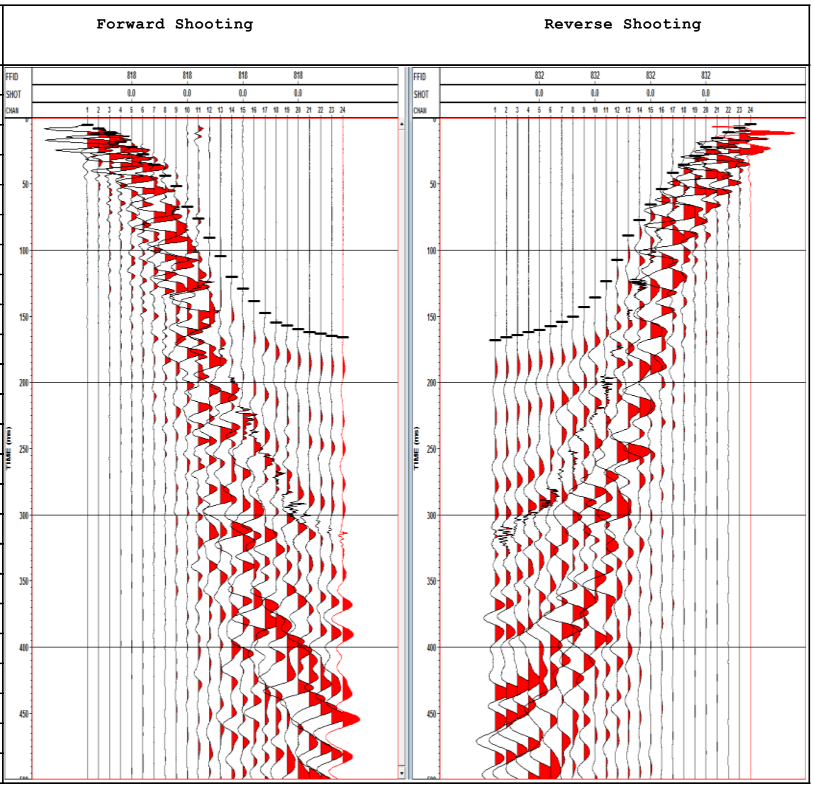

c: Line 2 station 6

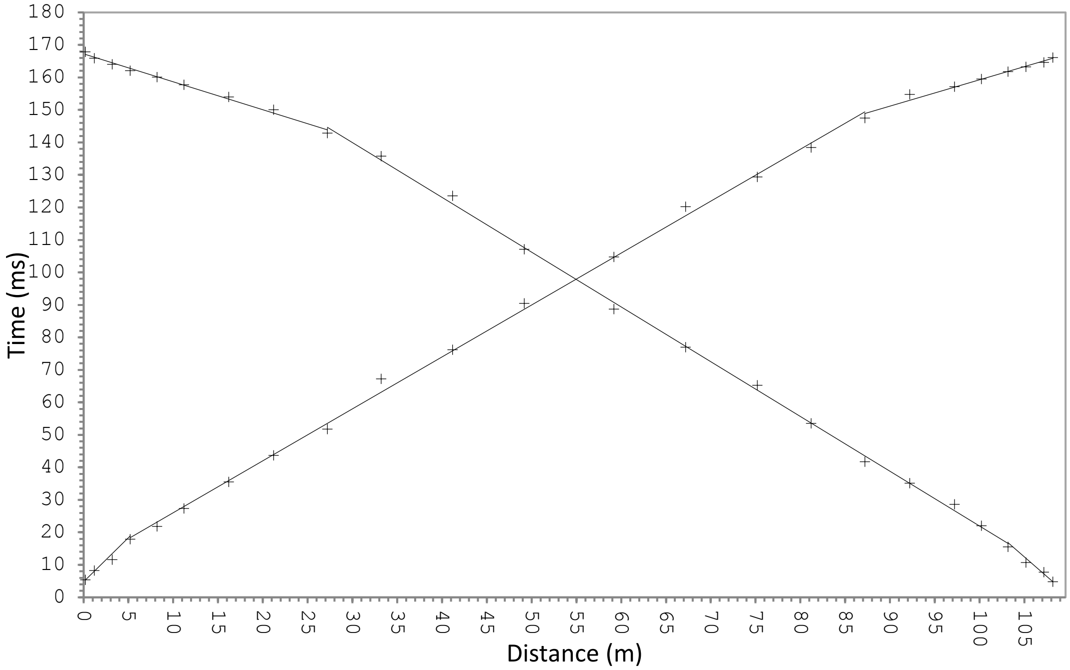

d: Interpretation of LVL of line 2 station 6

Offset (m)	FBT (ms) Left	FBT (ms) Right
0	5.351	5.904
1	7.889	8.551
3	13.674	12.012
5	18.409	16.695
8	23.931	24.024
11	29.717	30.811
16	39.447	37.258
21	43.918	42.806
27	47.073	46.968
33	50.492	49.941
41	54.963	54.102
49	59.696	59.043
59	65.993	64.804
67	70.478	70.155
75	75.505	75.505
81	79.073	79.073
87	82.640	81.846
92	84.679	85.103
97	87.046	87.750
100	89.180	90.193
103	90.465	90.753
105	90.728	91.313
107	91.254	91.873

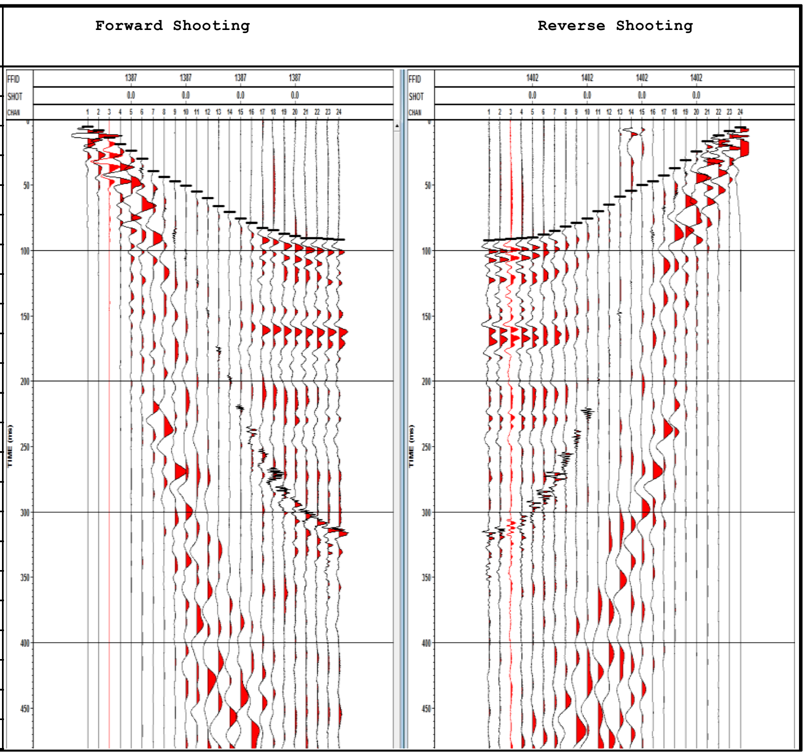

e: Line 3 station 11

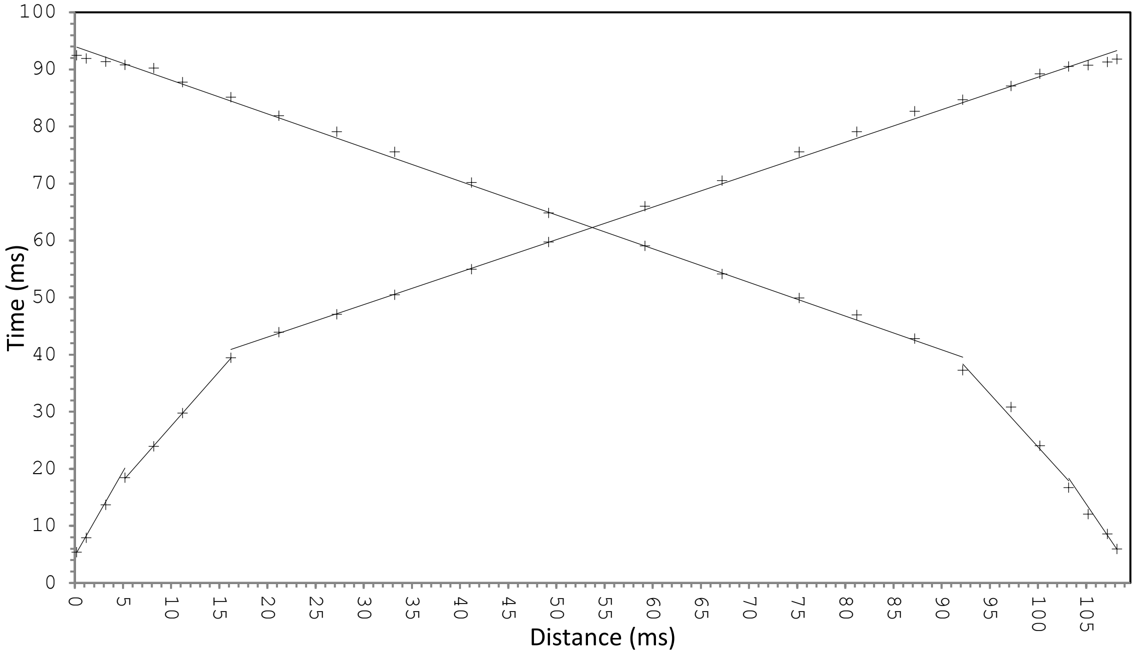

f: Interpretation of Line 3 station 11

Offset (m)	FBT (ms) Left	FBT (ms) Right
0	1.784	7.134
1	9.298	10.881
3	15.690	18.022
5	20.809	21.762
8	28.835	24.483
11	35.834	38.424
16	46.373	51.005
21	59.272	62.226
27	68.957	76.397
33	83.485	87.729
41	101.305	101.665
49	115.933	109.831
59	126.292	123.773
67	136.742	132.273
75	143.338	145.195
81	151.605	149.275
87	156.122	157.096
92	162.708	166.277
97	167.356	170.036
100	170.843	171.717
103	172.586	175.386
105	174.197	177.765
107	175.386	180.737
108	176.460	184.899

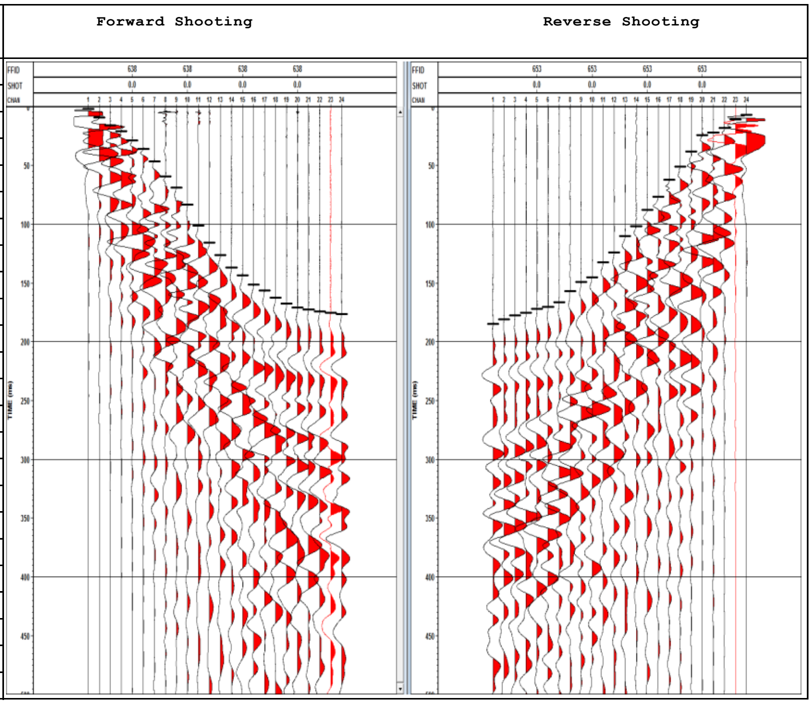

g: Line 4 station 7

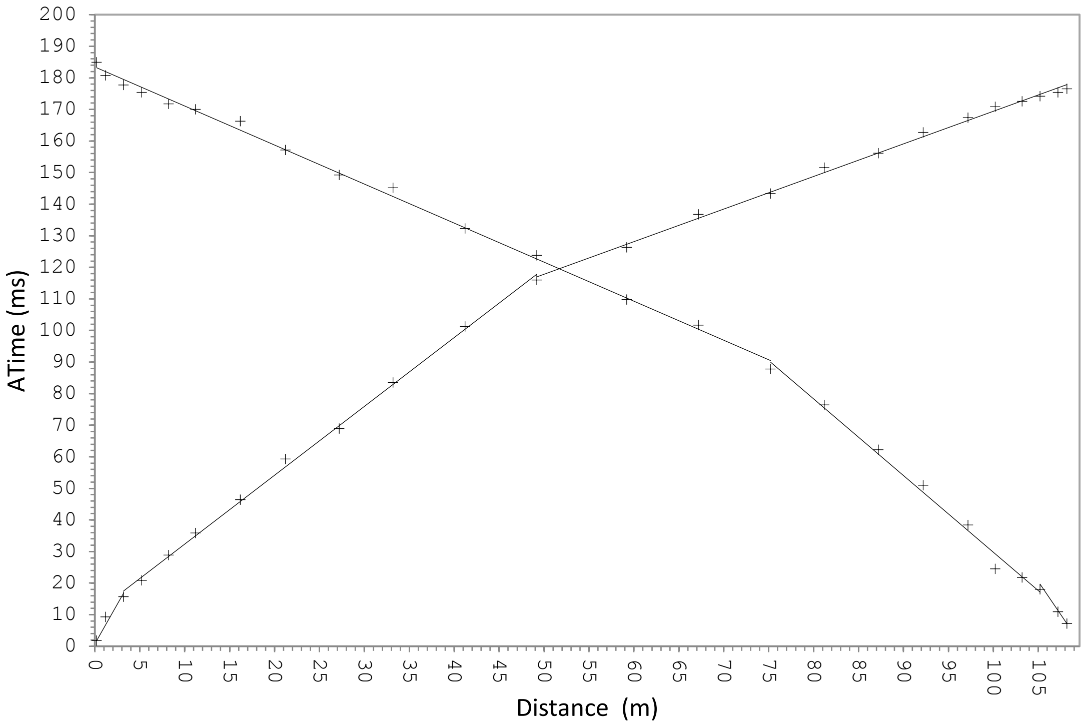

h: Interpretation for line 4 station 7

Offset (m)	FBT (ms) Left	FBT (ms) Right
0	2.025	4.756
1	8.099	10.807
3	16.450	20.214
5	25.308	27.315
8	37.709	38.297
11	46.061	46.837
16	56.437	57.993
21	70.104	70.155
27	83.770	82.640
33	95.665	91.684
41	104.776	105.977
49	129.072	121.284
59	140.207	131.599
67	147.547	146.254
75	152.608	153.438
81	155.645	157.160
87	157.670	161.454
92	162.732	164.890
97	164.090	166.321
100	165.874	168.847
103	167.658	170.330
105	168.847	170.902
107	169.441	171.475
108	170.036	172.048

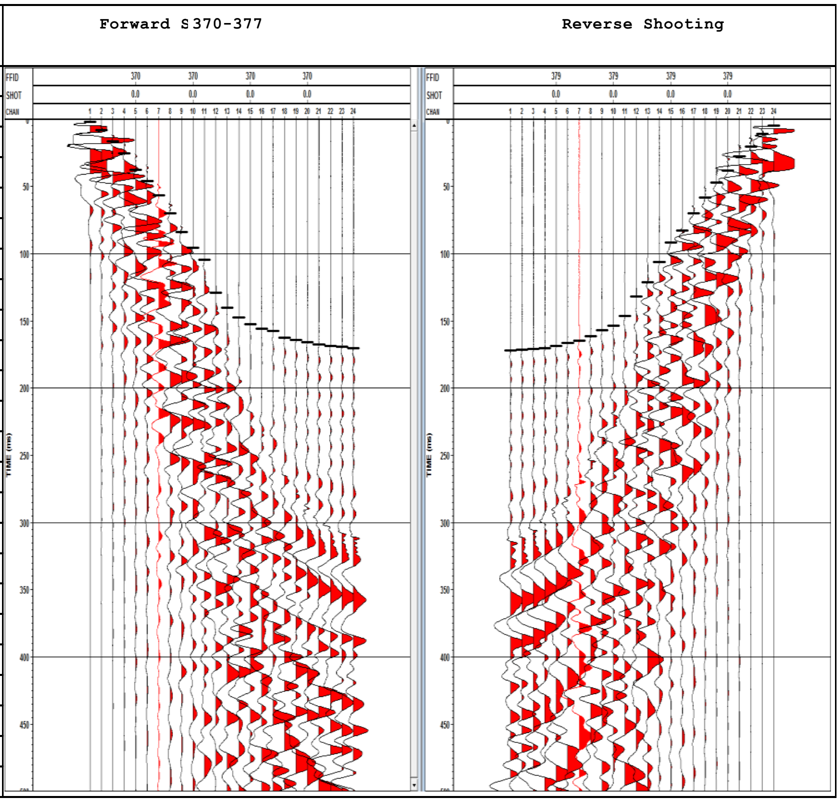

i: Line 5 station 14

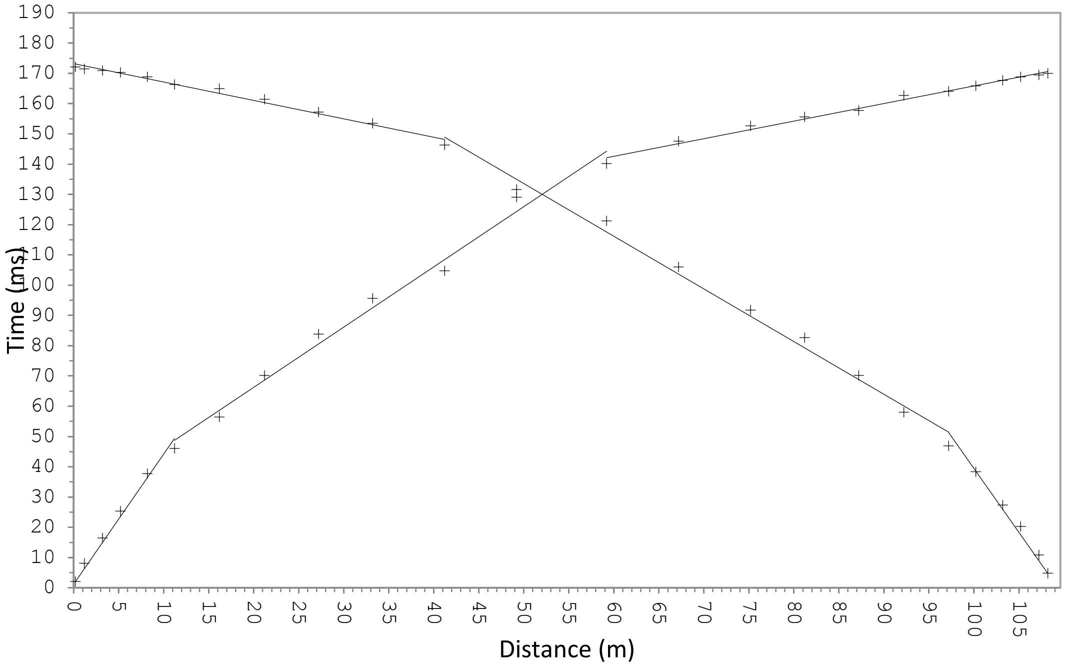

j: Interpretation Line 5 station 14

Offset (m)	FBT (ms) Left	FBT (ms) Right
0	5.351	5.070
1	8.971	11.465
3	16.081	18.091
5	23.192	24.717
8	30.302	31.343
11	37.412	37.335
16	43.858	45.401
21	48.178	50.240
27	52.829	56.924
33	57.481	63.615
41	64.209	68.966
49	70.155	74.316
59	73.127	77.289
67	76.100	80.410
75	80.856	81.748
81	82.640	83.086
87	84.394	84.423
92	86.055	85.612
97	86.609	86.405
100	87.162	87.198
103	87.716	87.991
105	88.270	88.783
107	88.381	89.576
108	89.045	90.369

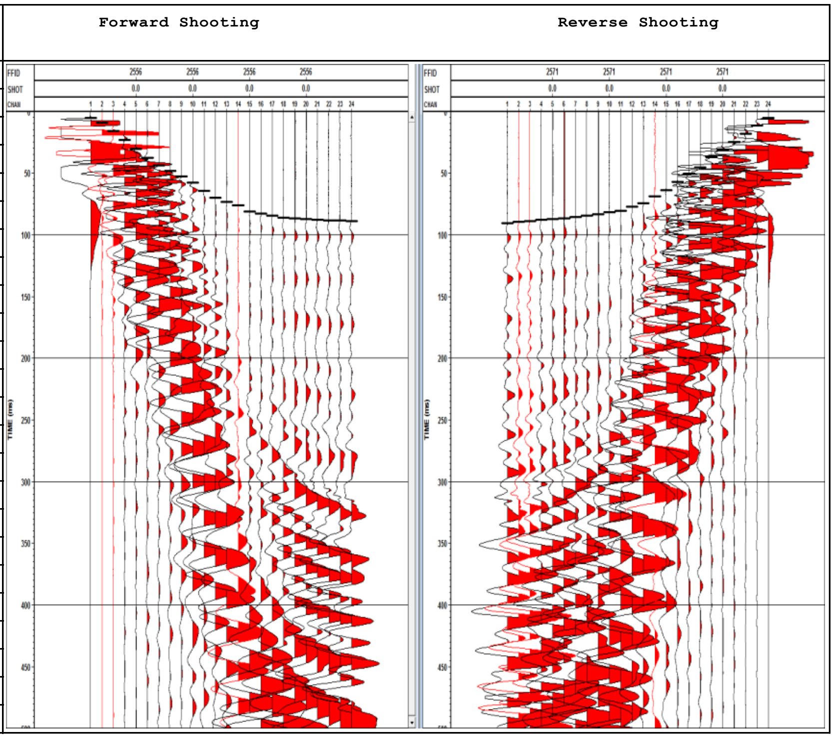

k: Line 6 station 9

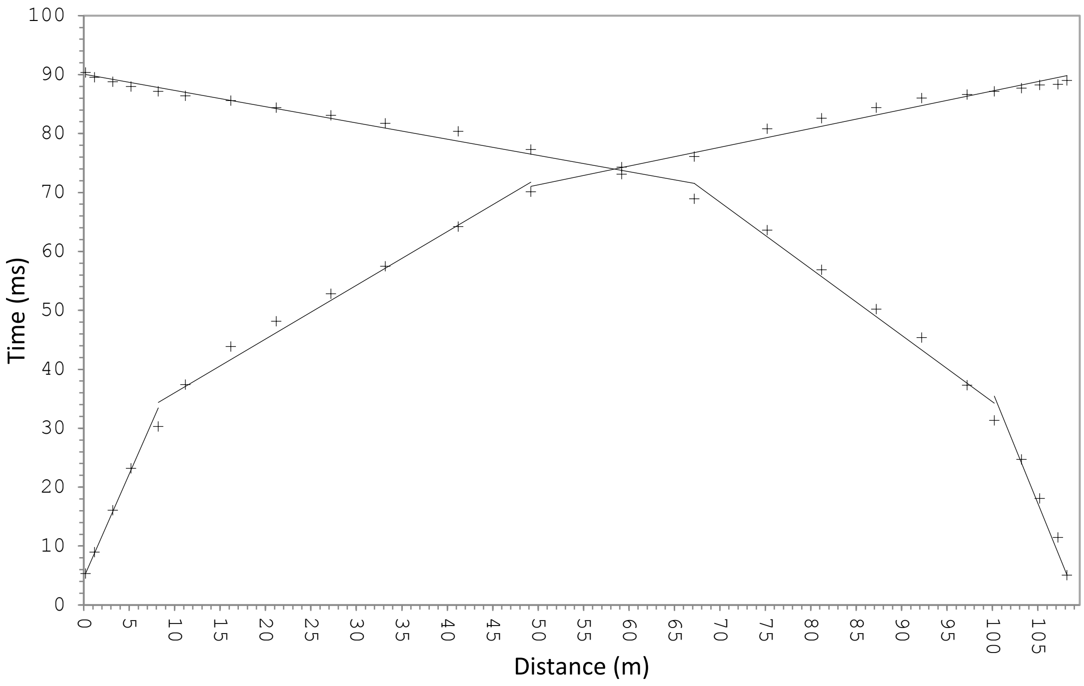

l: Interpretation of Line 6 station 9

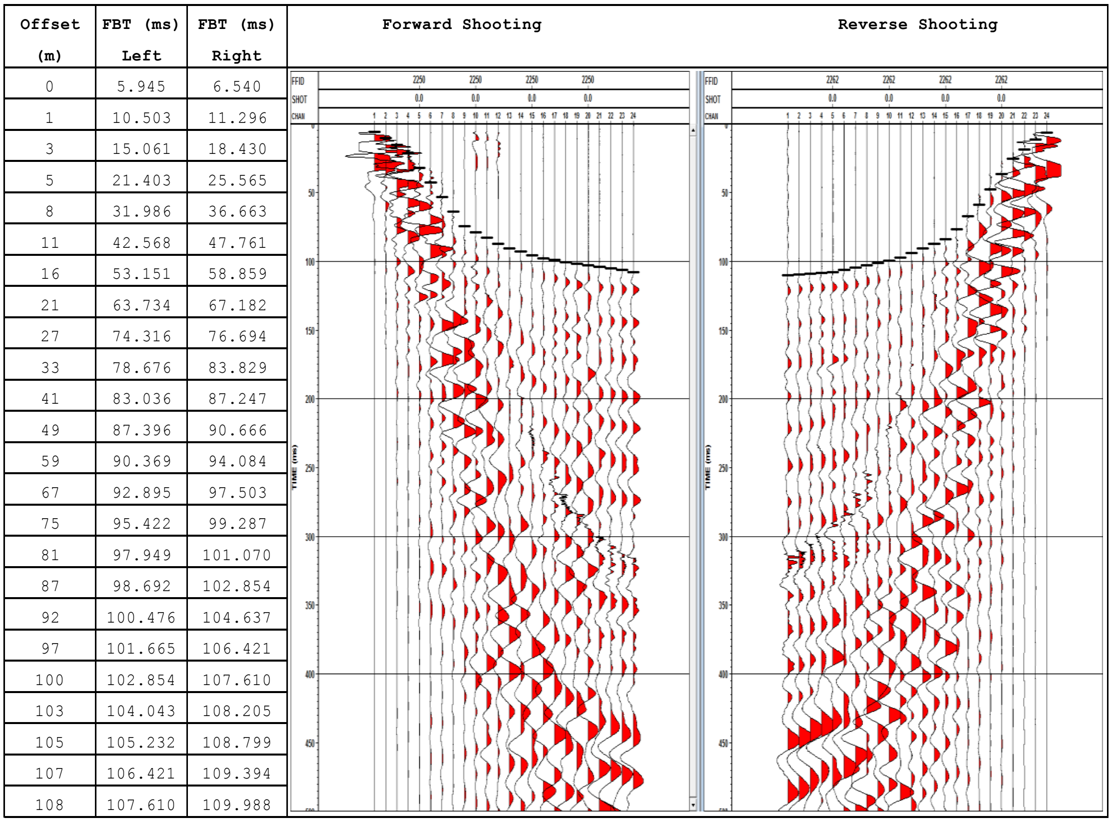

Offset (m)	FBT (ms) Left	FBT (ms) Right
0	5.945	6.540
1	10.503	11.296
3	15.061	18.430
5	21.403	25.565
8	31.986	36.663
11	42.568	47.761
16	53.151	58.859
21	63.734	67.182
27	74.316	76.694
33	78.676	83.829
41	83.036	87.247
49	87.396	90.666
59	90.369	94.084
67	92.895	97.503
75	95.422	99.287
81	97.949	101.070
87	98.692	102.854
92	100.476	104.637
97	101.665	106.421
100	102.854	107.610
103	104.043	108.205
105	105.232	108.799
107	106.421	109.394
108	107.610	109.988

m: Line 7 station 6

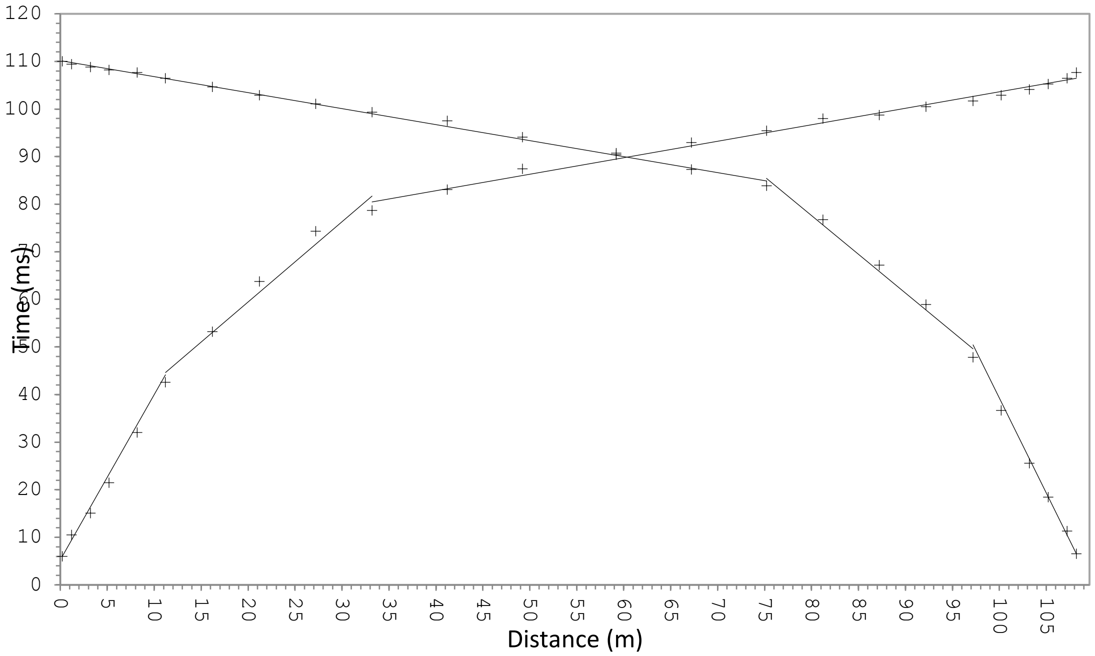

n: Interpretation Line 7 station 6

Offset (m)	FBT (ms) Left	FBT (ms) Right
0	1.189	1.189
1	4.741	3.697
3	10.347	9.182
5	15.953	14.666
8	21.559	20.150
11	27.165	25.634
16	32.508	32.536
21	40.127	40.374
27	47.746	48.212
33	55.365	56.938
41	62.984	65.164
49	71.449	73.391
59	76.935	81.709
67	82.420	87.872
75	87.906	94.034
81	93.392	100.196
87	98.877	102.457
92	102.854	104.637
97	105.952	107.015
100	108.333	108.323
103	110.119	109.631
105	111.310	110.939
107	113.159	112.247
108	114.286	113.555

Forward Shooting **Reverse Shooting**

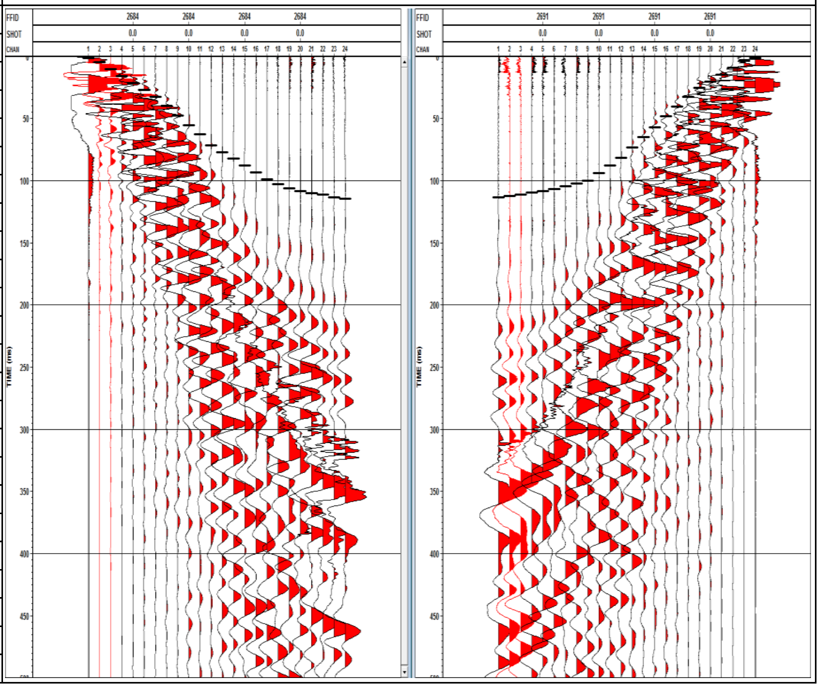

o: Line 8 station 17

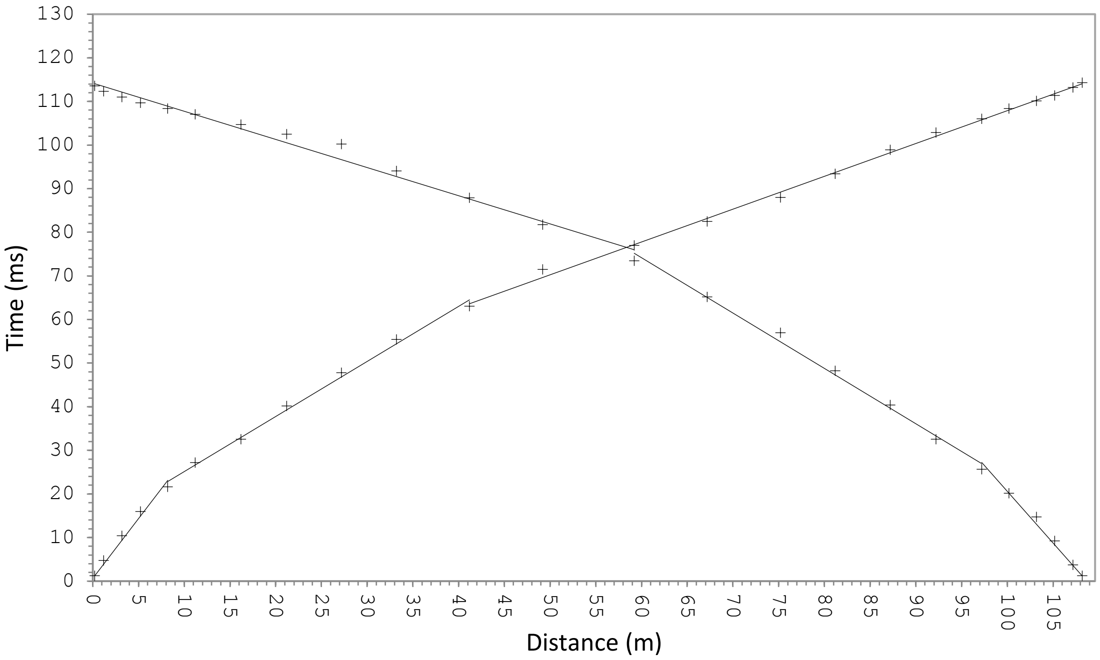

p: Interpretation Line 8 station 17

Appendix 2: Low Velocity Layer Summary Data

Line 1

Station Number	Elevation	V_0 (m/s)	V_1 (m/s)	V_2 (m/s)	Thickness (Z_0) (m)	Thickness (Z_1) (m)	Depth Z (m)
1	955.9	271.5	1576.3	3184.3	1.1	13.1	14.3
2	874.2	248.0	2136.1	3604.1	1.3	21.9	23.3
3	794.4	288.8	972.5	2837.4	1.5	17.3	18.8
4	734.5	280.4	2450.6	4516.4	1.4	22.4	23.8
5	718.8	283.9	1090.3	4355.9	1.1	8.8	9.8
6	687.4	391.1	832.4	1408.8	2.7	25.3	28.0
7	667.1	255.6	672.9	1278.3	1.6	10.4	12.0
8	653.4	216.8	558.4	1291.2	3.1	19.7	22.8
9	646.0	238.5	477.8	1650.7	3.9	24.2	28.1
10	644.1	209.8	475.9	1520.4	3.2	22.9	26.1
11	640.5	187.5	489.6	1682.4	2.8	24.1	26.9

Line 2

Station Number	Elevation	V_0 (m/s)	V_1 (m/s)	V_2 (m/s)	Thickness (Z_0) (m)	Thickness (Z_1) (m)	Depth Z (m)
1	852.3	235.1	2616.7	3512.9	1.5	35.2	36.7
2	790.9	244.5	1597.7	3965.9	1.3	14.4	15.7
3	686.6	285.4	1853.3	3519.5	1.2	15.4	16.6
4	660.1	362.2	864.4	1519.4	2.6	19.4	22.0
5	667.3	289.2	964.9	2265.4	2.0	23.8	25.8
6	682.8	292.6	609.5	1198.6	1.5	27.0	28.4
7	686.3	292.7	1188.4	1712.1	2.0	30.9	32.9
8	668.0	229.2	672.0	1127.9	1.3	10.3	11.6
9	662.0	334.2	1694.0	2357.1	2.6	36.6	39.1

10	665.8	564.7	2220.9	3279.5	4.8	43.4	48.2
11	657.2	365.1	1381.8	2702.8	3.8	37.9	41.6
12	631.8	453.1	1221.4	3349.6	3.6	24.7	28.3
13	628.2	368.6	1349.0	2299.9	2.2	26.9	29.1
14	688.5	251.0	1570.5	3438.0	1.2	14.0	15.2
15	724.7	353.7	1021.8	1337.9	1.6	12.1	13.7
16	663.7	309.4	890.9	1645.0	8.2	42.8	51.0
17	656.3	272.7	709.7	1049.8	1.4	18.0	19.3
18		496.1	1288.2	2553.8	12.4	52.0	64.4
19		378.4	1436.4	2630.4	1.7	17.8	19.5

Line 3

Station Number	**Elevation**	**V_0 (m/s)**	**V_1 (m/s)**	**V_2 (m/s)**	**Thickness (H_0) (m)**	**Thickness (H_1) (m)**	**Depth WZ (m)**
1	677.5	457.6	1215.2	1806.5	3.3	30.2	33.4
2	671.7	376.8	748.6	1556.3	2.0	13.6	15.6
3	656.9	378.4	1436.4	2630.4	1.7	17.8	19.5
4	618.2	253.1	1053.6	3384.2	1.6	19.0	20.6
5	616.3	343.5	1155.7	3418.8	2.2	19.6	21.8
6	611.7	223.0	714.0	1636.1	1.0	11.2	12.2
7	610.8	228.1	848.3	1751.1	1.0	7.4	8.5
8	609.3	612.9	1215.3	2750.5	1.9	12.3	14.2
9	607.2	200.9	629.2	1609.5	1.0	8.0	9.0
10	603.8	270.1	978.5	1516.0	1.0	10.9	11.8
11	606.7	271.0	529.5	1724.8	1.3	8.6	9.9

Line 4

Station Number	Elevation	V_0 (m/s)	V_1 (m/s)	V_2 (m/s)	Thickness (H_0) (m)	Thickness (H_1) (m)	Depth WZ (m)
1	1005.6	266.2	926.6	2223.9	5.7	41.2	46.9
2	1084.7	489.8	2802.3	3561.4	2.4	42.7	45.1
3	999.7	257.1	1489.2	2019.5	1.8	34.9	36.7
4	936.4	280.8	1856.3	2370.6	1.2	32.4	33.6
5	778.2	259.4	545.8	671.8	4.7	27.5	32.2
6	751.8	249.2	2099.8	2284.4	1.3	39.0	40.3
7	708.8	176.2	435.2	888.9	1.0	14.5	15.5
8	645.9	648.7	1100.9	1556.9	5.8	24.7	30.5
9	606.3	408.8	1301.5	1685.2	2.6	16.0	18.6
10	655.6	337.5	1225.2	1959.9	1.3	11.3	12.7
11	635.9	496.1	1288.2	2553.8	12.4	52.0	64.4
12	621.1	266.0	886.6	2781.7	3.3	25.4	28.8
13		230.7	611.6	1793.2	2.6	18.7	21.4
14		273.6	630.0	1897.4	2.0	15.5	17.5
15		173.8	508.7	1671.5	1.9	15.4	17.3
16		247.6	1041.9	1584.9	2.0	17.6	19.5
17		239.6	534.1	1647.7	1.9	18.4	20.4

Line 5

Station Number	Elevation	V_0 (m/s)	V_1 (m/s)	V_2 (m/s)	Thickness (H_0) (m)	Thickness (H_1) (m)	Depth WZ (m)
1	800.3	353.6	545.4	674.6	5.4	28.1	33.4
2	834.8	401.0	2801.0	3422.2	2.4	46.3	48.7
3	732.1	321.9	802.1	1169.8	6.1	36.2	42.3
4	700.6	565.2	1216.4	2105.9	4.6	26.5	31.1
5	604.4	392.2	1739.7	2288.1	1.9	32.1	34.0
6	602.1	564.4	2060.5	4844.4	5.8	49.8	55.6
7	745.4	275.2	1016.1	1961.2	2.0	38.1	40.2
8	679.1	309.3	905.4	2072.9	1.4	28.5	29.9
9	656.3	272.7	709.7	1049.8	1.4	18.0	19.3
10	639.4	216.2	470.0	1854.8	3.3	19.9	23.2
11	640.3	243.3	629.1	1871.4	5.3	27.5	32.7
12	642.6	232.3	571.9	1578.0	3.8	28.6	32.4
13	646.0	238.5	477.8	1650.7	3.9	24.2	28.1
14	650.3	222.8	538.3	1682.2	3.6	30.6	34.1
15	657.2	236.7	476.3	1605.1	2.6	28.1	30.6

Line 6

Station Number	Elevation	V_0 (m/s)	V_1 (m/s)	V_2 (m/s)	Thickness (H_0) (m)	Thickness (H_1) (m)	Depth WZ (m)
1	635.2	582.3	1096.6	1378.4	2.4	16.2	18.6
2	626.5	374.3	1123.4	3115.7	1.5	18.0	19.5
3	681.8	501.3	1123.0	1755.7	3.5	17.7	21.2
4	663.7	309.4	890.9	1645.0	8.2	42.8	51.0
5	696.6	323.4	887.5	3311.3	4.5	30.5	35.0
6	739.7	292.6	1202.1	2345.7	1.1	9.1	10.2
7	718.8	283.9	1090.3	4355.9	1.1	8.8	9.8

Line 7

Station Number	Elevation	V_0 m/s)	V_1 (m/s)	V_2 (m/s)	Thickness (H_0)(m)	Thickness (H_1)(m)	Depth WZ (m)
1	652.4	402.0	1864.2	3784.3	2.0	21.8	23.7
2	626.5	374.3	1123.4	3115.7	1.5	18.0	19.5
3	629.8	241.5	1448.8	2679.0	1.2	31.7	32.9
4	728.5	334.5	1036.3	1913.4	1.4	10.4	11.8
5	686.3	292.7	1188.4	1712.1	2.0	30.9	32.9
6	643.2	237.9	603.7	2930.3	3.7	22.0	25.7
7	643.2	229.3	599.1	1549.1	3.6	27.8	31.5
8	642.6	232.3	571.9	1578.0	3.8	28.6	32.4
9	644.1	209.8	475.9	1520.4	3.2	22.9	26.1
10	641.3	193.9	423.9	1738.2	2.8	23.1	25.9

Line 8

Station Number	Elevation	V_0 (m/s)	V_1 (m/s)	V_2 (m/s)	Thickness (H_0) (m)	Thickness (H_1) (m)	Depth WZ (m)
1	732.3	310.0	1924.4	4030.3	1.7	20.1	21.8
2	706.1	235.9	1384.4	3126.5	1.3	14.9	16.2
3	702.5	306.1	896.7	2556.5	2.3	19.6	21.9
4	687.4	391.1	832.4	1408.8	2.7	25.3	28.0
5	675.0	217.7	875.3	1466.2	1.2	9.6	10.8
6	651.0	224.9	803.0	2650.5	3.0	23.0	26.0
7	643.2	229.3	599.1	1549.1	3.6	27.8	31.5
8	640.3	243.3	629.1	1871.4	5.3	27.5	32.7
9	635.3	145.1	380.3	1831.1	1.3	16.9	18.2
10	630.4	184.8	656.9	1844.5	2.5	23.0	25.4
11	627.2	325.7	817.5	1588.3	2.6	16.9	19.5
12	623.4	226.9	764.2	1946.2	1.5	21.4	22.8
13	621.1	266.0	886.6	2781.7	3.3	25.4	28.8
14	615.9	193.8	776.5	1813.2	1.9	17.1	19.0
15	611.1	333.6	1060.3	1874.5	1.9	16.2	18.1
16	618.2	253.1	1053.6	3384.2	1.6	19.0	20.6
17	649.3	383.1	790.0	1438.9	2.8	18.2	21.0
18	706.2	419.4	676.7	1010.4	2.0	13.2	15.1